

# Modeling of metal-organic frameworks for optical applications

Von der Naturwissenschaftlichen Fakultät der  
Gottfried Wilhelm Leibniz Universität Hannover

zur Erlangung des Grades  
Doktor der Naturwissenschaften (Dr. rer. nat.)

genehmigte Dissertation

von

Marvin Treger, M. Sc.

2023

Referentin: Prof. Dr. rer. nat. Carolin König  
Korreferenten: Prof. Dr. techn. et rer. nat. Dr. h. c. Franz Renz  
Dr. rer. nat. Michael Fischer  
Tag der Promotion: 14.12.2023

## Kurzzusammenfassung

Metall-organische Gerüste (*engl. metal-organic frameworks*, MOFs) stellen eine bedeutende Gruppe innerhalb der porösen Hybridmaterialien dar. Sie bestehen aus Metallionen oder Metall-Oxo-Clustern, die als anorganische Baueinheiten bezeichnet werden und durch organische Liganden verknüpft sind, die als Linker bezeichnet werden. MOFs wurden intensiv im Hinblick auf klassische Anwendungsgebiete für poröse Materialien wie beispielsweise Katalyse und Gastrennung betrachtet. Im Gegensatz dazu werden in dieser Arbeit MOFs für die Verwendung als Materialien für optische Anwendungen untersucht. Hierbei ist insbesondere der Brechungsindex (refraktiver Index, RI) von besonderer Relevanz.

In dieser Arbeit wurde ein *ab initio* Simulationsprotokoll entwickelt, das eine verlässliche und präzise Berechnung der elektronischen Struktur und des RIs von MOFs ermöglicht. Hierzu wird die Dichtefunktionaltheorie (DFT) verwendet, um ausgehend von Einkristallstrukturdaten Modelle von MOFs zu erstellen und die optischen Eigenschaften zu berechnen. Beginnend mit dem bekannten MOF UiO-66 und dessen etablierten nitro- und aminofunktionalisierten Derivaten UiO-66-NO<sub>2</sub> und UiO-66-NH<sub>2</sub> wurde dieses Simulationsprotokoll angewendet. Anschließend wurde die Verwendung von „push-pull“-Linkermolekülen zum Aufbau des UiO-66 Gerüsts untersucht und das neue UiO-66-(NH<sub>2</sub>,NO<sub>2</sub>) Derivat computer-chemisch charakterisiert. Weiterhin wurde die Verwendung von monohalogenierten Linkermolekülen untersucht, mit welchen die UiO-66-X (X = F, Cl, Br, I) Derivate erhalten werden können. Zusätzlich wurde das neue UiO-66-I<sub>2</sub> Derivat vorgestellt, um im sichtbaren Spektralbereich einen hohen RI bei gleichzeitiger Transparenz zu erhalten.

Das im ersten Teil dieser Arbeit vorgestellte Simulationsprotokoll erlaubt ein tieferes Verständnis des Einflusses der modularen Komponenten eines MOFs auf den RI, aber ist mit einem hohen Rechenaufwand verbunden. Daher wurde ein weiteres effizienteres Simulationsprotokoll zur Berechnung des RIs von MOFs entwickelt. Dieses Protokoll basiert auf der Fragmentierung von MOFs, so dass die Polarisierbarkeiten der modularen Komponenten eines MOFs separat mittels DFT berechnet werden konnten. Anschließend wurde die Polarisierbarkeit des MOFs und der entsprechende RI unter der Verwendung der Lorenz-Lorentz-Gleichung berechnet.

**Stichwörter:** Metall-organische Gerüste, Modellierung, Dichtefunktionaltheorie, elektronische Struktur, Brechungsindex



## Abstract

Metal-organic frameworks (MOFs) are an important class of porous hybrid materials. They consist of metal ions or metal-oxo clusters forming the so-called inorganic building units connected by organic ligands acting as linker molecules leading to an intrinsic porosity of the framework. MOFs have been discussed intensively with regard to classical applications of porous materials like catalysis and gas separation. In this work, a different aspect is focused, namely the use of MOFs as optical materials. One fundamental property in this respect is the refractive index (RI).

To ensure the reliable and precise calculation of the RI of MOFs a novel *ab initio* simulation protocol was developed in this work. By applying density functional theory (DFT), accurate models of MOF crystal structures were prepared and the optical properties were calculated precisely. Starting with the well-known UiO-66 MOF and its established nitro- and amino-functionalized derivatives UiO-66-NO<sub>2</sub> and UiO-66-NH<sub>2</sub>, this simulation protocol was used to calculate the electronic structures and the corresponding optical properties. Furthermore, the incorporation of “push–pull” linkers into the UiO-66 framework was studied to allow a further tuning of the RI of the parent UiO-66 MOF. In this context, a novel UiO-66 analogue denoted as UiO-66-(NH<sub>2</sub>,NO<sub>2</sub>) was presented. In addition, the use of halogenated linkers yielding the well-known monohalogenated UiO-66 derivatives denoted as UiO-66-X (X = F, Cl, Br, I) was studied. To obtain high RI values while preserving the transparency in the visible spectral region, a novel dihalogenated UiO-66 derivative denoted as UiO-66-I<sub>2</sub> was introduced.

The simulation protocol developed in the first part of this work allows a detailed study of the electronic structure of MOFs and a better understanding how the the various modular components of a MOF influence its RI. This protocol is computationally demanding. As a consequence, a second, more efficient simulation protocol was presented allowing the screening of MOFs with regard to their RI. This simulation protocol is based on a fragmentation scheme for MOFs allowing the separate calculation of the polarizability of the modular components of MOFs using DFT. These polarizabilities were used to compute the total polarizability of a MOF and subsequently the corresponding RI by applying the Lorenz-Lorentz equation.

**Keywords:** metal-organic frameworks, modeling, density functional theory, electronic structure, refractive index



# Danksagung

An dieser Stelle möchte ich zunächst an Herrn Prof. Dr. Peter Behrens erinnern. Mein außerordentlicher Dank gilt Ihm für seine langjährige Betreuung meiner wissenschaftlichen Ausbildung beginnend mit der Bachelorarbeit über die Masterarbeit und schließlich der Promotion. Darüber hinaus danke ich Ihm für die Möglichkeit auf diesem interessanten, interdisziplinären Thema promovieren und die Forschungsergebnisse europaweit präsentieren zu können sowie für die eingehenden und inspirierenden Gespräche.

Weiterhin danke ich Frau Prof. Dr. Carolin König für den fachlichen Austausch, die Begleitung meiner Arbeit und für die Übernahme der Betreuung des letzten Teils meiner Arbeit und des Referates.

Herrn Prof. Dr. Dr. h. c. Franz Renz und Herrn Dr. Michael Fischer danke ich für die Übernahme der Korreferate und bei Herrn Prof. Dr. Dirk Dorfs bedanke ich mich herzlich für die Übernahme des Vorsitzes der Promotionskommission.

Ferner danke ich Dr. Andreas Schneider für die Begleitung meiner Arbeit, die Unterstützung beim Veröffentlichen der Publikationen und der Korrektur meiner Arbeit. Außerdem möchte ich mich bei ihm für die Möglichkeit zum Einstieg in das Molecular Modeling bedanken.

Dem gesamten Arbeitskreis Behrens spreche ich meinen Dank für die Unterstützung während meiner gesamten Promotionszeit aus. Gerne erinnere ich mich auch an die humorvollen Pausen und die zahlreichen gemeinsamen außerfachlichen Aktivitäten wie die Boßeltouren. Insbesondere möchte ich an dieser Stelle Dr. Andreas Schaate danken, der seit meinem ersten Tag im Arbeitskreis Behrens bei jeglichen Herausforderungen und Fragen zur Verfügung stand und darüber hinaus nicht nur meinen fachlichen sondern auch meinen kulturellen Horizont erweitert hat.

Besonders bedanken möchte ich mich auch bei allen aktiven und ehemaligen Mitgliedern des *in silico* Labors für die Einarbeitung, die Unterstützung bei jeglichen Problemen und die ausgezeichnete Arbeitsatmosphäre. Dabei möchte ich Lauritz Bußfeld für seine Einführung in die Systemadministration, viele neue spannende Musikgenres und das Mountainbiken danken. Ebenso danke ich Nils Denda für die vielen Stunden der fachlichen und außerfachlichen Diskussionen und die täglichen erheiternden Momente. Hinzukommt seine Unterstützung bei der Anfertigung dieser Arbeit durch die Einführung in  $\LaTeX$  und das Korrekturlesen.

## *Danksagung*

Ich möchte mich auch bei allen Freunden bedanken, die mich während meines Studiums und der Promotion begleitet und unterstützt haben. Hierbei möchte ich Patrick Bessel für den vielfältigen Austausch auch außerhalb der Universität danken. Besonders unser Pastatag war eine Institution und zentraler Bestandteil jeder Woche.

Schließlich bedanke ich mich herzlich bei meinen Eltern, die mir während der gesamten Studien- und Promotionszeit unterstützend zur Seite standen und immer ein offenes Ohr hatten.



# Contents

Kurzzusammenfassung	iii
Abstract	v
Danksagung	vii
Abbreviations	xi
1 Introduction	1
2 Theoretical background	5
2.1 Metal-organic frameworks . . . . .	5
2.1.1 Zirconium-based metal-organic frameworks . . . . .	10
2.1.2 Zeolitic imidazolate frameworks . . . . .	15
2.2 Density functional theory . . . . .	17
2.2.1 Theoretical foundations . . . . .	17
2.2.2 Kohn-Sham density functional theory . . . . .	22
2.3 Quantum mechanical calculation of the refractive index . . . . .	31
2.3.1 General background of the optical properties in the solid state . . . . .	32
2.3.2 Methods for the calculation of the refractive index . . . . .	41
2.4 References . . . . .	45
3 Results and discussion	55
3.1 Tuning the optical properties of the metal-organic framework UiO-66 via ligand functionalization . . . . .	55
3.2 Development of high refractive index UiO-66 framework derivatives via ligand halogenation . . . . .	67
3.3 Fragment-based approach for the efficient calculation of the refractive index of metal-organic frameworks . . . . .	78
4 Conclusion and outlook	93
5 Curriculum vitae	99
6 Publications	101



## Abbreviations

<i>ab initio</i>	<i>lat.</i> from the beginning or from first principles, here: relying on fundamental constants and laws of nature
au	atomic units
<i>bdc</i>	1,4-benzenedicarboxylate
BET	Brunauer–Emmett–Teller
<i>bpdc</i>	biphenyl-4,4-dicarboxylate
BZ	Brillouin zone
CCP	cubic closed packed
CDFT	current density functional theory
CGTO	contracted GTO
CPKS	coupled perturbed Kohn-Sham
DFT	density functional theory
DOS	density of states
DRS	diffuse reflectance spectroscopy
<i>e. g.</i>	<i>lat.</i> <i>exempli gratia</i> , for example
Eq.	equation
et al.	<i>lat.</i> <i>et alii</i> , and others
Fig.	figure
FWHM	full width at half maximum
GGA	generalized gradient approximation
GH	global hybrids
GTO	Gaussian-type-orbitals
HF	Hartree-Fock
hGGA	hybrid GGA
HK	Hohenberg-Kohn
HPC	high-performance computing
IBU	inorganic building unit
IR	infrared
IRMOF	isorecticular MOF
JDOS	joint density of states

## Abbreviations

KS	Kohn-Sham
LCAO	linear combination of atomic orbitals
LDA	local density approximation
LUIS	Leibniz University IT Service
mGGA	meta-GGA
MIL	Materials from Institut Lavoisier
MOF	metal-organic framework
PBC	periodic boundary conditions
PDOS	partial density of states
PhoenixD	Photonics, Optics, and Engineering – Innovation Across Disciplines
PW	plane wave
PNA	<i>para</i> -nitroaniline
PXRD	powder X-ray diffraction
QM	quantum mechanical
RCSR	Reticular Chemistry Structure Resource
RI	refractive index
RSH	range-separated hybrid
SCF	self consistent field
Sec.	section
SEM	scanning electron microscopy
STO	Slater-type-orbitals
TGA	thermogravimetric analysis
<i>tpdc</i>	[1,1':4',1''-terphenyl]-4,4''-dicarboxylate
UiO	Universitetet i Oslo
UV	ultraviolet
Vis	visible
XC	exchange-correlation
ZIF	zeolitic imidazolate framework

# 1 Introduction

More than 75 years ago, the transistor was invented.<sup>[1]</sup> This paved the way for the development of microelectronics and started a revolution in electronics leading to the digitization of every part of our daily life. In an analogous way, the transformation in optical technologies and photonics is a corner stone of the 21<sup>st</sup> century. Today, glass optical fibers are already the backbone of our communication and allow the exponential increase of internet traffic. For the pioneering work on the transmission of light in fibers for communication, K. C. Kao received the Nobel Prize in Physics 2009 highlighting the relevance of advances in photonics.<sup>[2,3]</sup> By overcoming traditional optical designs with novel, digital, and integrated optics, photonics will become competitive to electronics in a growing field of applications, because photons do not dissipate heat along the transmission line and allow logical operations at much higher speed.<sup>[4]</sup> Furthermore, novel optical systems like lensless cameras can be realized with digital optics.<sup>[5]</sup> This is only possible by replacing high precision optical systems by miniaturized, integrated, and digital optical systems facilitated by the advances in computing power. These novel optical systems require novel preparation techniques for example additive manufacturing allowing individualized optical components at low cost.

Those novel optical systems and their production require also novel materials. Traditional materials for optical applications like glasses and polymers are often limited in the adaptability of their optical properties and processability. For example, the development of high refractive index polymers with full transparency in the visible spectral range is an ongoing challenge.<sup>[6,7]</sup> Especially materials with a high or low refractive index (RI) or a combination of both are needed for novel optical elements like frequency tripling mirrors and the development of integrated photonics.<sup>[4,8]</sup> Thus, the development of novel materials with a large adaptability of the optical properties and simplified preparation routes are essential. Using inorganic-organic hybrid materials for optical applications is a promising approach to fulfill these requirements.<sup>[4,9,10]</sup> The materials show properties that are not only the sum of their single components' properties and even overcome the limitations of the individual components. One prominent class of hybrid materials are metal-organic frameworks (MOFs).

MOFs are inorganic-organic hybrid materials consisting of metal ions or metal-oxo clusters forming so-called inorganic building units (IBUs). These IBUs are coordinated by organic ligands denoted as linkers. The use of linkers with two or more metal-binding sites results in

## 1 Introduction

the formation of one- up to three-dimensional frameworks. The modular design of MOFs allows countless possible combinations and fueled the fast growth of the MOF research field since the first report of a metal-containing coordination network by Hoskins et al.<sup>[11]</sup> in 1989. Due to the spacing between the IBUs introduced by the linkers, MOFs show an intrinsic porosity. Therefore, MOFs have been discussed intensively with regard to classical applications of porous materials, like catalysis, gas separation, gas storage, or gas sensing.<sup>[12–14]</sup> Recently, the use of MOFs as materials for optical applications and the examination of their RI has gathered increasing attention.<sup>[15–19]</sup>

A prominent family of MOFs is formed by the zirconium-based frameworks, most of which feature outstanding chemical and thermal stability, promoting Zr-based MOFs for materials development.<sup>[20]</sup> The family of Zr-based MOFs originates from the work of Cavka et al.<sup>[21]</sup> reporting the exceptional stable UiO-66 MOF in 2008. UiO-66 is formed by Zr-metal-oxo clusters coordinated by 1,4-benzenedicarboxylate (*bdc*) linkers. It is structurally well characterized and has been studied extensively regarding its chemical, electrical, and optical properties as well as possible applications.<sup>[22]</sup> As a consequence, UiO-66 has become an archetypal MOF. Furthermore, numerous functionalized UiO-66 derivatives with altered properties can be obtained by using *bdc* linkers that contain additional functional groups. Therefore, UiO-66 is used as model compound to examine MOFs and their adaptability for optical applications in this work.

To select potential MOFs for novel optical applications, the knowledge of the optical properties with a focus on the RI is fundamental. Due to the countless number of possible MOFs, computational screenings are a convenient approach for examining MOFs.<sup>[23]</sup>

In 2014, the first attempt to calculate the RI of UiO-66 was made by Yang et al.<sup>[24]</sup> using a semiempirical method. They used Kohn-Sham density functional theory (DFT) to obtain equilibrium structural parameters and calculated optical properties using the PBE generalized gradient approximation (GGA) exchange–correlation (XC) functional. A plane wave basis set was chosen with a kinetic plane-wave cutoff energy of 500 eV. This cutoff energy was converged with respect to the total energy of the formula unit. To compensate the well-known underestimation of the band gap by the PBE XC functional, they shifted the calculated optical properties by a scissors operator based on the experimental band gap of UiO-66. In 2020, Ni et al.<sup>[25]</sup> published an *ab initio* DFT-based study including the calculation of the RI of UiO-66 and some of its derivatives. In this study, the PBE XC functional was used in combination with the Grimme DFT-D2 dispersion correction method for structural optimization.<sup>[26]</sup> Again, a kinetic plane-wave cutoff energy of 500 eV was used. Analogous to the study of Yang et al.,

a scissors operator correction was applied for the calculation of the optical properties. The scissors operator value was determined by comparing the band gaps obtained using the HSE06 and PBE XC functionals. The used range-separated hybrid GGA XC functional HSE06 is known to yield accurate band gaps.<sup>[27-29]</sup> Both approaches rely on the correction of the PBE calculations with a scissors operator leading to an overestimation of the amplitude of the dielectric function and thus to inaccurate RI values.<sup>[30]</sup> Nevertheless, both studies allow a qualitative study of the RI of UiO-66 and its derivatives.

The present work aims at the reliable and accurate calculation of the RI of MOFs. This promotes the examination of established MOFs as well as the design of novel MOFs for optical applications. Furthermore, a better understanding how the modular components of a MOF influence its RI can be obtained. Therefore, a novel *ab initio* simulation protocol is developed in this work allowing not only the accurate calculation of the optical properties but also of the electronic structure. By applying DFT, models of MOF crystal structures are prepared and subsequently the optical properties are evaluated. Therefore, carefully converged plane wave basis sets are used and different XC functionals are assessed. Finally, the HSE06 XC functional is used to determine both, the electronic structure and optical properties of MOFs.

As a consequence, this simulation approach is computationally demanding and thus not suitable for the large screening of MOFs with regard to their RI. In the literature, different methods are described reducing the computational effort for the evaluation of the RI of dense materials like polymers, molecular materials, and metal-organic networks.<sup>[31-33]</sup> These methods are based on the evaluation of either oligomers simplifying polymers or clusters and aggregates to study molecular materials or metal-organic networks. This allows to circumvent demanding calculations using periodic boundary conditions or extensive models to obtain the RI. The two- or three-dimensional porous structure of MOFs renders the application of these methods impossible or prevents the speed-up of the calculations provided by these methods, respectively. Accordingly, a second simulation approach is presented in this work, that aims at the efficient calculation of the RI of MOFs. This simulation approach is based on a fragmentation scheme for MOFs allowing the separate calculation of the polarizability of the modular components of MOFs. The polarizability of the fragments is then used to compute the total polarizability of a MOF and subsequently the Lorenz-Lorentz equation can be used to obtain the corresponding RI. This fragment-based approach is applied to a diverse series of MOFs.





## 2 Theoretical background

The following sections deal with an introduction into metal-organic frameworks (MOFs), their properties and applications with a focus on zirconium-based MOFs and zeolitic imidazolate frameworks. Subsequently, density functional theory is introduced as computational quantum mechanical modeling method. Finally, two methods are presented to calculate the refractive index (RI).

### 2.1 Metal-organic frameworks

Metal-organic frameworks are an emerging class of materials forming a subset of coordination polymers.<sup>[34]</sup> In contrast to coordination polymers, they contain potential voids and are formed by organic ligands that can be modified.<sup>[34,35]</sup> Furthermore, they show geometrically well-defined structures leading to high crystallinity.<sup>[35]</sup> Nevertheless, non-crystalline MOFs like amorphous MOFs and MOF glasses exist.<sup>[36,37]</sup>

The general building principle of MOFs was already outlined by Hoskins et al.<sup>[11]</sup> in 1989 describing metal nodes linked by organic connecting units forming cavities. Later, the term metal-organic framework was introduced in 1995 by Yaghi et al.<sup>[38]</sup> A MOF is built up by metal ions or metal-oxo clusters denoted as inorganic building units (IBUs). These IBUs are coordinated by organic ligands termed linkers. In the simplest case, this ligand has two metal coordination moieties resulting in a linear, rod-like ditopic linker connecting two IBUs (see Fig. 2.1).

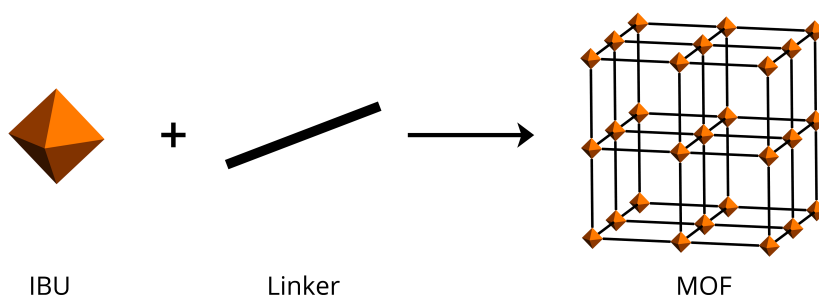


Figure 2.1: General building scheme of MOFs: the framework is constructed by IBUs coordinated by linkers. Here a six-connected octahedral IBU is coordinated by a linear ditopic linker.

## 2 Theoretical background

Next to ditopic linkers, tritopic up to octatopic linkers connecting up to eight IBUs have been used to synthesize MOFs.<sup>[39]</sup> The vast majority of these linkers are carboxylates and azolates, but for example phosphates, sulfonates, and linkers based on chelating groups like ortho-diols, -dithiols, and -diamines are also known.<sup>[39–41]</sup> Overall, the most studied linkers are ditopic carboxylates.<sup>[39]</sup> A very prominent example is the 1,4-benzenedicarboxylate (*bdc*) linker (see Fig. 2.2a) which has been used to construct a large number of MOFs. Additionally, it can be modified with a variety of functional groups. In Fig. 2.2, three examples of *bdc*-based MOFs are given. The first two MOFs are built up by isolated zero-dimensional IBUs and the last MOF is constructed with an chain-like one-dimensional IBU. Fig. 2.2b and 2.2c show the structures of MOF-5 with a zinc-based, six-fold connected IBU and UiO-66 with a zirconium-based, 12-fold connected IBU, respectively.<sup>[21,42]</sup> In contrast, Fig. 2.2d shows the structure of MIL-53 consisting of an chromium-based IBU formed by a chain of corner-sharing octahedra.<sup>[43]</sup>

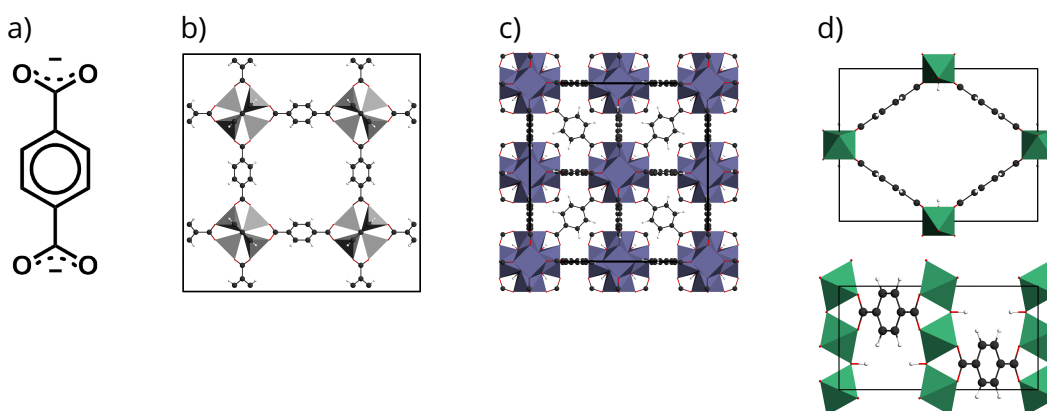


Figure 2.2: MOFs built up by the *bdc* linker: a) *bdc* linker, b) MOF-5, c) UiO-66 and d) MIL-53 (view along [100] at top and [010] at bottom).

Additionally, the formation of a certain MOF is not limited to a given metal-linker combination. Often, the metal ions can be varied to obtain a metal-substituted version of a given MOF. For example the *bdc* linker can be combined with zirconium, hafnium, thorium, uranium, or cerium to obtain UiO-66-type MOFs and MIL-53-type MOFs can be built up with chromium, vanadium, aluminum, indium, iron, gallium, or scandium.<sup>[21,43–53]</sup> Furthermore, a given metal-linker combination can form different MOFs depending on the reaction conditions, *e. g.* MIL-140A (see Sec. 2.1.1) is built up by the *bdc* linker and Zr ions as well.<sup>[54]</sup> This emphasizes the adaptability of MOFs as well as the capabilities of obtaining different MOFs due to

H																	He	
Li	Be											B	C	N	O	F	Ne	
Na	Mg											Al	Si	P	S	Cl	Ar	
K	Ca	Sc	Ti	V	Cr	Mn	Fe	Co	Ni	Cu	Zn	Ga	Ge	As	Se	Br	Kr	
Rb	Sr	Y	Zr	Nb	Mo	Tc	Ru	Rh	Pd	Ag	Cd	In	Sn	Sb	Te	I	Xe	
Cs	Ba			Hf	Ta	W	Re	Os	Ir	Pt	Au	Hg	Tl	Pb	Bi	Po	At	Rn
Fr	Ra			Rf	Db	Sg	Bh	Hs	Mt	Ds								
		La	Ce	Pr	Nd	Pm	Sm	Eu	Gd	Tb	Dy	Ho	Er	Tm	Yb	Lu		
		Ac	Th	Pa	U	Np	Pu	Am	Cm	Bk	Cf	Es	Fm	Md	No	Lr		

Figure 2.3: Periodic table of elements showing metals (orange) that have been used to construct MOFs. Data gathered by Yuan et al.<sup>[55]</sup>

their modular design. In total, the mono-, di-, tri- or tetravalent ions of 62 metals have been used to construct MOFs (see Fig. 2.3).<sup>[55]</sup>

In addition to the variation of the metal ion, organic chemistry can be used to modify a linker and exploit the modular design of MOFs. The modification of linkers allows the preparation of MOFs with altered physical and chemical properties over a broad range.<sup>[56]</sup> MOF-5 is a well-studied example in this context. Its *bdc* linker can be modified over a wide range with functional groups, e. g. halogen atoms or an amino moiety. The use of these functionalized linkers and closely related reaction conditions results in MOFs sharing the structure and topology of the parent MOF-5 (see Fig. 2.4).<sup>[57]</sup> Such a series of MOFs is called isorecticular and allows the rational design and synthesis of MOFs from their modular components.<sup>[57]</sup>

Accordingly, MOF-5 is also known as isorecticular MOF-1 (IRMOF-1).<sup>[57]</sup> The bromo derivative of IRMOF-1 can be obtained with 2-bromobenzene-1,4-dicarboxylate (*bdc-Br*) and is called IRMOF-2.<sup>[57]</sup> In addition to IRMOF-2, the complementary monohalogenated IRMOF-2-*X* (*X* = F, Cl, I) derivatives can be obtained by using the corresponding *bdc-X* linkers (see Tab. 2.1). Using 2-aminobenzene-1,4-dicarboxylate (*bdc-NH<sub>2</sub>*), the amino derivative of IRMOF-1 called IRMOF-3 can be prepared.<sup>[57]</sup> Furthermore, the *bdc* linker can be extended by incorporating a second and third phenylene group resulting in the biphenyl-4,4'-dicarboxylate (*bpdc*) and [1,1':4',1''-terphenyl]-4,4''-dicarboxylate (*tpdc*) linkers, respectively. These linkers can be used to construct the IRMOF-10 and IRMOF-16 using the *bpdc* or *tpdc* linker, respectively, and tune the pore sizes of the IRMOFs.<sup>[57]</sup> The largest pore of IRMOF-1 has a diameter of 18.5 Å, growing up to 24.5 Å and 28.8 Å for IRMOF-10 and IRMOF-16, respectively (see Fig. 2.4).<sup>[57]</sup>

## 2 Theoretical background

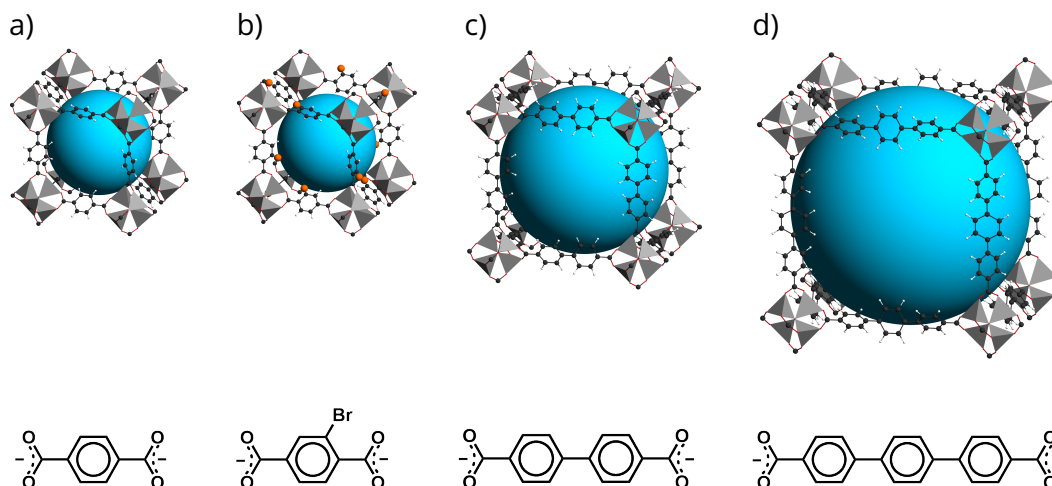


Figure 2.4: IRMOF series with primitive cubic topology built up by zinc-based  $[\text{Zn}_4\text{O}]^{6+}$  IBUs (gray) with pores (blue) and corresponding linkers: a) MOF-5 (IRMOF-1) b) IRMOF-2, c) IRMOF-10 and d) IRMOF-16.

Table 2.1: Examples of different IRMOFs obtained by modifying the *bdc* linker.

MOF	linker	reference
IRMOF-1	<i>bdc</i>	[42]
IRMOF-2	<i>bdc-Br</i>	[57]
IRMOF-2- <i>X</i> ( <i>X</i> = F,Cl,I)	<i>bdc-X</i>	[58]
IRMOF-3	<i>bdc-NH<sub>2</sub></i>	[57]
IRMOF-10	<i>bpdc</i>	[57]
IRMOF-16	<i>tpdc</i>	[57]

All in all, the modular design of MOFs results in numberless possibilities to construct a MOF. In addition to the building principles of MOFs presented above, the preparation of MOFs using different metal ions or linkers simultaneously in a single framework is possible. These MOFs are denoted as mixed-metal and mixed-linker MOFs, respectively.<sup>[59,60]</sup> Yet, more than 100 000 MOFs have been synthesized and over 500 000 MOFs have been predicted.<sup>[61,62]</sup> In 2008, O’Keeffe et al.<sup>[63]</sup> presented a system to identify the topological structures of MOFs with three periodic nets. These nets are collected in the Reticular Chemistry Structure Resource (RCSR) and assigned with RCSR symbols. The RCSR symbols are written in lower case and bold, *e. g.*

**dia** for the four-connected net of cubic diamond and **bcu** for the body-centered cubic lattice. The IRMOFs show the **pcu** topology corresponding to the primitive cubic lattice.

As stated initially, MOFs are generally crystalline and porous. The porosity is an intrinsic property of the frameworks due to the spacing of the IBUs introduced by the linkers. Using functionalized linkers, the chemistry of the pores and their size can be tailored. The Brunauer–Emmett–Teller (BET) area of activated carbon can be taken as reference for MOFs and ranges approximately from 250 to 2500 m<sup>2</sup> g<sup>-1</sup>.<sup>[64]</sup> From the *bdc*-based MOFs presented above, MOF-5 has the largest BET area with 3800 m<sup>2</sup> g<sup>-1</sup>, followed by UiO-66 with 1400 m<sup>2</sup> g<sup>-1</sup> and MIL-53 with 1300 m<sup>2</sup> g<sup>-1</sup>.<sup>[65–67]</sup> Today, the DUT-60 MOF has the largest reported BET area of all MOFs with 7800 m<sup>2</sup> g<sup>-1</sup>.<sup>[68]</sup>

## Applications

Based on their porosity, MOFs have been discussed intensively with regard to classical applications of porous materials like catalysis, gas separation and gas storage.<sup>[69,70]</sup> MOFs have been investigated for numerous catalytic applications, for example as solid Lewis and Brønsted acids or as hosts for guests with catalytic properties like metal nanoparticles.<sup>[69]</sup> Additionally, using MOFs for photocatalytic hydrogen evolution and carbon dioxide reduction was discussed.<sup>[69]</sup> Furthermore, MOFs have been used as membrane materials for liquid separation, *e. g.* desalination, and gas separation, *e. g.* nitrogen and carbon dioxide separation, or hydrogen purification.<sup>[71]</sup> Besides the separation of gases, the storage of gases *e. g.* carbon dioxide or energy-related gases like methane and hydrogen in MOFs is of interest.<sup>[70]</sup> In addition, MOFs have been examined for energy storage applications for example as electrode materials in supercapacitors due to their remarkable surface area.<sup>[72]</sup> Related to the studies focusing on the use of MOFs for gas separation and storage is the exploration of MOFs as chemical sensors for gas or vapor detection.<sup>[73]</sup> Finally, MOFs are also discussed as materials for biological applications for example as drug delivery systems.<sup>[74]</sup>

Beyond these studies, some early-stage companies deal with the commercialization of MOF-based products with a focus on the separation, storage or sensing of gases. For instance, Water Harvesting Inc. develops MOF-based atmospheric water generation products based on the MOF water harvester developed at University of California, Berkeley.<sup>[75,76]</sup> The first available commercial MOF-based product is a dopant gas delivery system produced by NuMat Technologies and labelled ION-X.<sup>[77]</sup> It allows the storage and delivery of phosphine, arsine, and boron trifluoride gases used as dopants for the fabrication of semiconductors.

## 2 Theoretical background

Moreover, MOFs have been examined for the use in optical applications as modular materials with a broad adaptability of the optical properties. These studies focus for example the photoluminescence and upconversion luminescence of MOFs for white-light emission and non-linear effects like the second-harmonic generation.<sup>[15,17]</sup> Therefore, lanthanides or linker with distinct optical properties are often used to construct MOFs.<sup>[15,17]</sup> Alternatively, guest molecules like organic dyes are introduced into the pores.<sup>[15]</sup> Furthermore, relative changes of the RI of MOFs due to the adsorption of guest molecules have been used to construct sensors for example by using MOFs as coatings for optical fibers.<sup>[78]</sup> In contrast, attempts to evaluate the RI of MOFs as fundamental property for many optical applications, *e. g.* coatings and filters, are rare.<sup>[16,79–81]</sup> To determine the RI of a MOF precisely, single crystals or optical thin films have to be prepared with high quality, whereby all present studies are based on optical thin films. The effort associated with these experiments to obtain precise and reliable results might be the reason for the limited number of such studies. As a consequence, this work aims at the development of computational methods to calculate the RI of MOFs precisely. Therefore, MOFs from the families of zirconium-based MOFs and zeolitic imidazolate frameworks are selected.

### 2.1.1 Zirconium-based metal-organic frameworks

The family of Zr-based MOFs evolved on the basis of a study published in 2008.<sup>[21]</sup> This study was concerned with a Zr-carboxylate MOF labelled UiO-66 showing high thermal and chemical stability.<sup>[21]</sup> The stability of UiO-66 has gathered a lot of attention and led to an rapidly increasing number of reports of new Zr-based MOFs most of which are constructed with carboxylates.<sup>[20,22]</sup> Today, more than 200 Zr-based MOFs have been recorded.<sup>[55]</sup> In general, Zr-carboxylate MOFs show a high stability compared to other MOFs.<sup>[55]</sup> This enhanced stability is provided by the strong metal-ligand bond. The strength of this coordination bonds originates from the high-valent Zr cation with its high charge density leading to a highly polarized bond in combination with carboxylate oxygen atoms. Furthermore, the high charge of the Zr cation requires more ligands for charge balancing. This results in IBUs with high connectivity and an enhanced framework stability.<sup>[55]</sup> This improved stability expands the field of possible applications and facilitates the development of materials for practical applications. Accordingly, Zr-based MOFs are a key element of this work allowing the reliable validation of the simulation protocols developed in this work. Therefore, UiO-66-type MOFs and the Zr-*fum* MOF as well as MIL-140A-type MOFs are selected. In the following, these MOFs are discussed in detail.

## UiO-66

The Zr-carboxylate MOF UiO-66 (Universitetet i Oslo, UiO) is based on the *bdc* linker and was discovered by the Lillerud group.<sup>[21]</sup> The IBU is 12-fold coordinated by the linker resulting in a structure which can be described as an expanded cubic closed packed (CCP) structure (see Fig. 2.5a). The CCP lattice is also called face-centered cubic lattice leading to the **fcu** label for this topology. The IBU of UiO-66 is formed by a hexanuclear metal-oxo cluster ( $[\text{Zr}_6\text{O}_4(\text{OH})_4]^{12+}$ ) based on an octahedron of Zr atoms (see Fig. 2.5c).<sup>[21]</sup> Each of these Zr atoms is eight-fold coordinated with a square-antiprismatic geometry (see Fig. 2.5d). The faces of the  $\text{Zr}_6$ -octahedron are capped with  $\mu_3$ -oxygen atoms and  $\mu_3$ -hydroxy groups forming the first square of the antiprism. The second square is constructed by four oxygen atoms of the carboxylate groups of four different linkers. Each carboxylate group of a linker connects the corners of two antiprisms (see Fig. 2.5e). This  $\text{Zr}_6$ -based IBU is characteristic for Zr-carboxylate MOFs and can be found in many frameworks.<sup>[20]</sup>

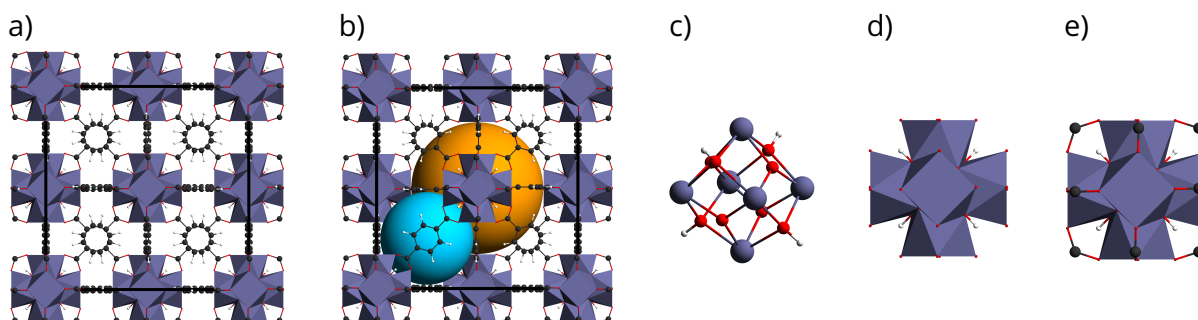


Figure 2.5: Structure and modular components of UiO-66 with  $F\bar{4}3m$  space group symmetry: a) unit cell, b) unit cell with octahedral (orange) and tetrahedral (blue) pore, c)  $[\text{Zr}_6\text{O}_4(\text{OH})_4]^{12+}$  IBU formed by an octahedron of zirconium atoms with  $\mu_3$ -oxygen atoms and  $\mu_3$ -hydroxy groups capping the triangular faces, d) polyhedra representation of the IBU with square antiprisms capping the  $\text{Zr}_6$ -octahedron and e) IBU with carboxylate groups connecting the corners of the antiprisms.

A single-crystal X-ray diffraction study by Øien et al.<sup>[82]</sup> revealed that the positions of the  $\mu_3$ -oxygen atoms and  $\mu_3$ -hydroxy groups of the IBU are distinct due to different Zr-O bond lengths and with an occupancy of 0.5 each. This allows the description of the crystal structure with space group  $Fm\bar{3}m$  (No. 225). The alternately placing of these groups, as shown in Fig. 2.5c, results in a model with reduced electrostatic interactions and lowers the symmetry of the

## 2 Theoretical background

structure corresponding to the space group  $F\bar{4}3m$  (No. 216).<sup>[83]</sup> Analog to the CCP lattice, the structure of UiO-66 contains tetrahedral and octahedral voids (Fig. 2.5b). These tetrahedral and octahedral pores of UiO-66 have a diameter of about 8 and 11 Å, respectively, with triangular windows of approximately 6 Å.<sup>[84]</sup>

UiO-66 shows an exceptional thermal and chemical stability.<sup>[21]</sup> This stability has been demonstrated against water, strong acids and many solvents.<sup>[83]</sup> Furthermore, it does not decompose in air up to 375 °C.<sup>[83]</sup> The heating of UiO-66 above 250 °C results in a dehydrated material.<sup>[83]</sup> This dehydrated UiO-66 is based on distorted  $[\text{Zr}_6\text{O}_6]^{12+}$  clusters instead of  $[\text{Zr}_6\text{O}_4(\text{OH})_4]^{12+}$  ones resulting in a lower symmetry ( $R\bar{3}m$ , No. 166).

In analogy to MOF-5, UiO-66 allows the preparation of a series of isorecticular MOFs. Especially the use of different mono-, di- and tetrasubstituted *bdc* linkers allows the preparation of a large number of UiO-66 derivatives denoted as UiO-66-*X*.<sup>[85]</sup> These MOFs share the stability of the parent UiO-66.<sup>[85]</sup> In Tab. 2.2 some examples of UiO-66 derivatives obtained via the halogenation of the *bdc* linker are shown. Additionally to the UiO-66-*X* derivatives, *M*-UiO-66 derivatives can be obtained by using Hf, Th, U or Ce, as stated in Sec. 2.1. Furthermore, the *bpdc* and *tpdc* linker and their functionalized derivatives can be used to construct isorecticular MOFs with extended pores known as UiO-67 and UiO-68, respectively.<sup>[21]</sup>

Table 2.2: Examples of different mono-, di- and tetrasubstituted UiO-66 derivatives obtained by using different halogenated *bdc* linkers with year of first publication.

MOF	X	linker	year	reference
UiO-66- <i>X</i>	F	<i>bdc</i> -F	2012	[86]
	F <sub>2</sub>	<i>bdc</i> -F <sub>2</sub>	2013	[87]
	F <sub>4</sub>	<i>bdc</i> -F <sub>4</sub>	2015	[88]
	Cl	<i>bdc</i> -Cl	2012	[86]
	Cl <sub>2</sub>	<i>bdc</i> -Cl <sub>2</sub>	2013	[87]
	Br	<i>bdc</i> -Br	2010	[89, 90]
	Br <sub>2</sub>	<i>bdc</i> -Br <sub>2</sub>	2013	[87]
	I	<i>bdc</i> -I	2013	[84]



Zr-*fum* MOF

In contrast to MOF-5, isorecticular UiO-66 MOFs can also be prepared by using shorter linkers. This is illustrated for example by the Zr-*fum*-MOF presented by the Behrens group in 2011.<sup>[91]</sup> This MOF is built up by the Zr<sub>6</sub>-based IBU and the fumarate (*fum*) linker and shows the **fcu** topology. Compared to the *bdc* linker, the *fum* linker is not strictly linear leading to a slightly tilted arrangement of the IBUs (see Fig. 2.6). Consequently, the symmetry is lowered to space group  $Pn\bar{3}$  (No. 201).<sup>[91]</sup> In 2014, Furukawa et al.<sup>[92]</sup> confirmed the initial structure of the Zr-*fum*-MOF by a single-crystal X-ray diffraction study and labeled the material as MOF-801. Analog to UiO-66, the Zr-*fum*-MOF can also be prepared by using Ce.<sup>[50]</sup> In comparison to UiO-66, the shorter *fum* linker leads to smaller diameters of the tetrahedral and octahedral pores and the BET area is reduced to approximately 860 m<sup>2</sup> g<sup>-1</sup>.<sup>[91]</sup> Due to the lower symmetry of the Zr-*fum*-MOF, two different tetrahedral pores (4.8 and 5.6 Å) are observed in addition to the octahedral pore with a size of 7.4 Å.<sup>[92]</sup> The triangular pore windows have a diameter of about 3.5 Å.<sup>[93]</sup> These small pore windows allow the efficient separation of small molecules like carbon dioxide and methane.<sup>[93]</sup> Using a methyl functionalized *fum* linker allows even the separation of Xenon and Krypton.<sup>[94]</sup> Furthermore, the Zr-*fum*-MOF exhibits an exceptional high water uptake at low pressures in combination with an excellent cycling performance.<sup>[92]</sup> Finally, this led to the construction of a proof-of-concept device and a first generation of devices for water harvesting from air by the Yaghi group at the University of California, Berkeley.<sup>[95]</sup>

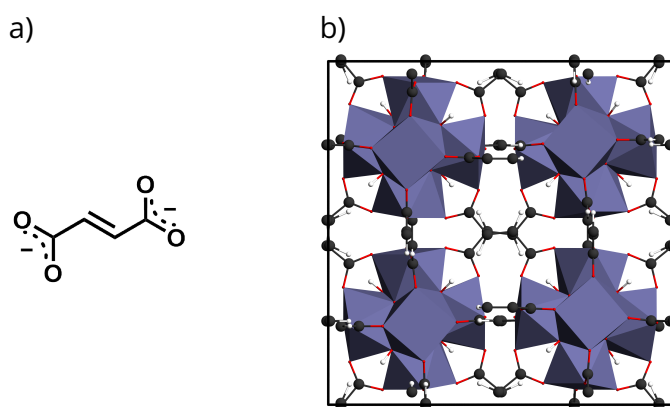


Figure 2.6: Zr-*fum*-MOF: a) *fum* linker and b) unit cell with  $Pn\bar{3}$  space group symmetry

## 2 Theoretical background

### MIL-140A

In 2012, the Serre group presented an isorecticular series of Zr-carboxylate MOFs labeled MIL-140 (Materials from Institut Lavoisier, MIL).<sup>[54]</sup> Analog to UiO-66, this series contains a Zr-based MOF constructed with the *bdc* linker denoted as MIL-140A (see Fig. 2.7). Contrary to the UiO-66 series, the MIL-140 series is built up by an one-dimensional IBU (see Fig. 2.7b). This IBU is formed by a chain of  $[\text{Zr}_2\text{O}_2]^{4+}$  dimers represented as edge-sharing Zr polyhedra forming a repeating tetramer of Zr polyhedra (see Fig. 2.7c). Each Zr polyhedron is constructed by seven oxygen atoms coordinating a Zr atom in analogy to the structure of monoclinic  $\text{ZrO}_2$ .<sup>[54]</sup> In the case of the Zr polyhedron in MIL-140, three of the seven coordinating oxygen atoms are  $\mu_3$ -oxygen atoms and four oxygen atoms belong to carboxylate groups. The one-dimensional IBUs are connected to six other IBUs resulting in triangular, one-dimensional pores. This results in the  $C2/c$  space group symmetry and **bsn** topology analog to the topology observed in the  $\beta$ -phase of tin (Sn).<sup>[54]</sup>

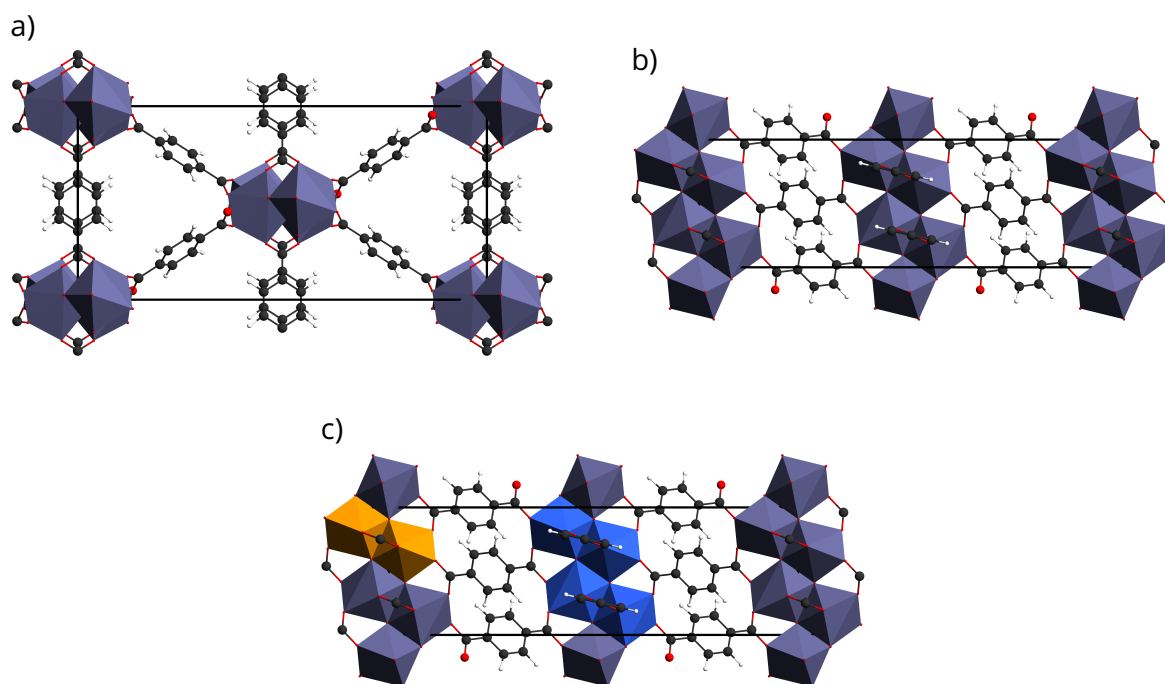


Figure 2.7: MIL-140A unit cell with  $C2/c$  space group symmetry: a) view along  $[001]$ , b) view along  $[010]$  and c) edge-sharing polyhedra of  $[\text{Zr}_2\text{O}_2]^{4+}$  dimer (orange) and repeating tetramer Zr polyhedra (blue).

Compared to UiO-66, MIL-140A shows a reduced porosity (BET area  $415 \text{ m}^2 \text{ g}^{-1}$ ) and an increased density.<sup>[54]</sup> In addition, the one-dimensional IBU leads to a close arrangement of the *bdc* linkers along the [010] direction resulting in  $\pi$  stacking for 50% of the linkers of MIL-140A (see Fig. 2.7a). These short-range dispersive interactions and the one-dimensional IBU lead to an enhanced thermal stability of the MIL-140A framework up to  $450^\circ \text{C}$  in air.<sup>[96]</sup> Similar to UiO-66, functionalized *bdc* linkers can be used to obtain MIL-140A derivatives.<sup>[97]</sup> But in contrast to UiO-66, the higher density of MIL-140A limits the use of sterically demanding moieties. For example the preparation of the monohalogenated derivatives is limited to MIL-140A-*X* (*X* = F, Cl, Br).<sup>[97]</sup> Corresponding to IRMOF-10 and UiO-67, the *bpdc* linker has been used to obtain an isorecticular MIL-140 MOF with an increased pore size denoted as MIL-140C.<sup>[54]</sup> Finally, Jacobsen et al.<sup>[98]</sup> presented the preparation of Ce-MIL-140A in 2020 .

### 2.1.2 Zeolitic imidazolate frameworks

Zeolitic imidazolate frameworks (ZIFs) are a prominent family of MOFs. In contrast to Zr-based MOFs, this family is not defined by MOFs sharing the same metal, but by frameworks all formed by imidazolate-based linkers. The term ZIF was introduced by the Yaghi group on the basis of a study presenting MOFs termed ZIF-1 to -12.<sup>[99]</sup> From these 12 ZIFs, ten show a topology already known from zeolites. This can be explained by a comparison of the Si-O-Si angle in zeolites and the metal-imidazolate-metal angle in ZIFs. Both angles are about  $145^\circ$  leading to the structural similarities of imidazolate-based MOFs and zeolites. Therefore, the building scheme of zeolites can be directly transferred to ZIFs. Zeolites are constructed by corner-sharing  $\text{TO}_4$  (*T* = Si, Al) tetrahedra. Accordingly, ZIFs are built up by metal atoms that are tetrahedrally coordinated by imidazolate linkers. In analogy to the oxygen atoms of zeolites linking the edges of  $\text{TO}_4$  tetrahedra, each imidazolate linker connects two metal nodes in a ZIF. Today, about 250 zeolite topologies are known and from these approximately 40 can be found in ZIFs.<sup>[100]</sup>

#### ZIF-8

ZIF-8 was one of the 12 first published ZIFs. Initially, it was discovered by Huang et al.<sup>[101]</sup> but only labeled as zeolite-type MOF with sodalite topology. ZIF-8 gathered rapidly increasing attention and is currently one of the most investigated MOF compounds.<sup>[22]</sup> It is built up by zinc ions and 2-methyl-imidazolate (*mim*) see Fig. 2.8a) and crystallizes with  $I\bar{4}3m$  space group symmetry and **sod** topology corresponding to the structure of sodalite (see Fig. 2.8b).<sup>[99]</sup> The

## 2 Theoretical background

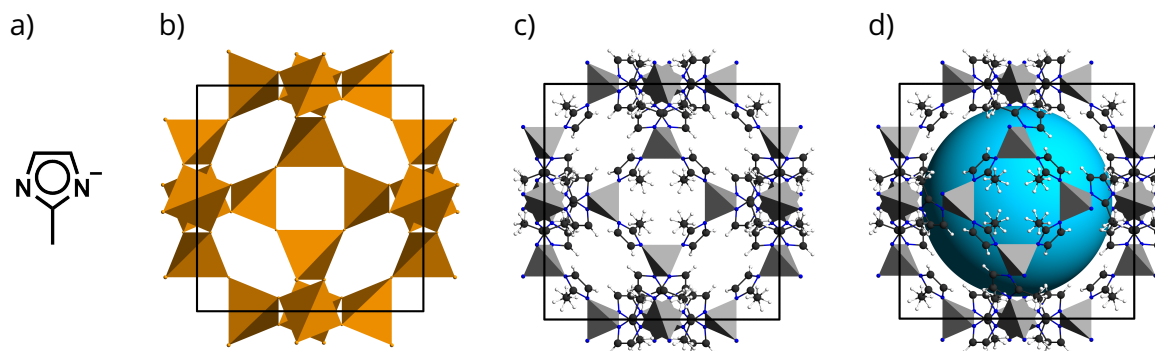


Figure 2.8: Structure and modular components of ZIF-8: a) 2-methylimidazolate linker, b) sodalite structure with corner sharing  $\text{TO}_4$  tetrahedra, c) ZIF-8 unit cell with  $I43m$  space group symmetry and tetrahedrally coordinated Zn atoms (gray) and d) ZIF-8 unit cell with highlighted central pore (blue).

Table 2.3: Examples of different ZIFs with SOD topology obtained with imidazolate derivatives and year of first publication.

ZIF	linker	year	reference
SALEM-2	<i>im</i> imidazolate	2012	[109]
ZIF-8	<i>mim</i> 2-methyl-imidazolate	2006	[99]
SOD-ZIF-71	<i>dcim</i> 4,5-dichloro-imidazolate	2014	[110]
ZIF-90	<i>ica</i> imidazolate-2-carboxyaldehyde	2008	[111]
ZIF-108	<i>nim</i> 2-nitro-imidazolate	2014	[112]
ZIF-318	$\text{CF}_3im$ 2-trifluoromethyl-imidazolate	2017	[113]

sodalite structure consists of cages with the form of truncated octahedra.<sup>[102]</sup> These cages are called  $\beta$ -cages and are constructed by six four-membered rings and eight six-membered rings denoted as  $[4^66^8]$ . Accordingly, the pores of ZIF-8 (see Fig. 2.8d) can be described as enlarged  $\beta$ -cages with a pore diameter of 12 Å and a diameter of about 3 Å for the hexagonal pore windows.<sup>[99,101]</sup> This results in a BET area of 1630 m<sup>2</sup> g<sup>-1</sup>.<sup>[99]</sup> ZIF-8 is thermally stable up to 400 °C in air and remains its structure and porosity in a series of solvents and under basic conditions.<sup>[103]</sup> Besides using zinc ions, ZIF-8 was also prepared by using cobalt, cadmium, magnesium, manganese, and iron ions.<sup>[104–108]</sup> In addition to the *mim* linker, Zn can be combined with a number of imidazolate derivatives to construct ZIFs with **sod** topology. Some of these ZIF-8 derivatives are compiled in Tab. 2.3.

ZIF-8 has been widely investigated as membrane material for separation applications.<sup>[114]</sup> Furthermore, ZIF-8 has been used to construct gas and vapor sensors on the basis of the change of its RI due to the adsorption of guest molecules. Only two years after its initial publication, ZIF-8 was already used to realize a gas sensor based on a Fabry-Pérot interferometer in 2010.<sup>[115]</sup> In 2012, Hinterholzinger et al.<sup>[116]</sup> prepared a photonic crystal composed of alternating dielectric layers (Bragg stack) enclosing a ZIF-8 film to perform optical sensing. Moreover, ZIF-8 has been used as coating for optical fibers to construct various types of optical sensors.<sup>[78]</sup> Recently, Keppler et al.<sup>[81]</sup> published a study concerned with the determination of the RI of ZIF-8. Additionally, the change of the RI of ZIF-8 induced by guest molecules was investigated and quantified. Therefore, different ZIFs including ZIF-8 and some of its derivatives are examined in this work regarding their RI by applying the developed simulation approaches.

## 2.2 Density functional theory

Density functional theory (DFT) is a quantum mechanical modeling method allowing the computation of the electronic structure of many-electron systems, *e. g.* solids. In this work, DFT is applied to MOFs to calculate their electronic structure and examine their optical properties. This section provides a brief introduction to DFT. Methods for the quantum mechanical calculation of optical properties are given in section 2.3. Starting with the Schrödinger equation, the Hartree-Fock approximation is introduced. Afterwards, the Hohenberg-Kohn theorems and the Kohn-Sham DFT are presented.

### 2.2.1 Theoretical foundations

The electronic structure of matter in a stationary state is described by the time-independent Schrödinger equation. The time-independent Schrödinger equation

$$\mathbf{H}\Psi = E\Psi \tag{2.1}$$

is composed of the wave function  $\Psi$ , the energy of the system  $E$  and the Hamiltonian operator  $\mathbf{H}$ .<sup>[117]</sup> Within the Born-Oppenheimer approximation, electrons are considered to move in the field of fixed nuclei since the nuclei are much heavier and thus move more slowly.<sup>[118]</sup>

## 2 Theoretical background

Consequently, the kinetic energy of the nuclei can be neglected and the repulsion between the nuclei is constant. This yields the electronic Hamiltonian

$$\begin{aligned} \mathbf{H}_{\text{elec}} &= \mathbf{T}_e + \mathbf{V}_{\text{ne}} + \mathbf{V}_{\text{ee}} \\ &= - \sum_{i=1}^N \frac{1}{2} \nabla_i^2 - \sum_{i=1}^N \sum_{A=1}^M \frac{Z_A}{r_{iA}} + \sum_{i=1}^N \sum_{j<i}^n \frac{1}{r_{ij}} \end{aligned} \quad (2.2)$$

for  $N$  electrons  $i$  and  $M$  nuclei  $A$ . It is composed of three operators describing the kinetic energy of the electrons  $\mathbf{T}_e$ , the Coulomb attraction of nuclei with atomic number  $Z_A$  and electrons  $\mathbf{V}_{\text{ne}}$  and the Coulomb repulsion of electrons  $\mathbf{V}_{\text{ee}}$ .<sup>[117]</sup> The distances  $r$  are given by the magnitudes of the corresponding position vectors  $\mathbf{r}$ , for example

$$r_{iA} = |\mathbf{r}_{iA}| = |\mathbf{r}_A - \mathbf{r}_i| \quad (2.3)$$

describes the distance between the  $i$ th electron and  $A$ th nucleus. The electronic Hamiltonian above as well as all following equations are given in atomic units, as a result all equations are dimensionless. The Coulomb attraction of nuclei and electrons

$$\begin{aligned} \mathbf{V}_{\text{ne}} &= \sum_{i=1}^N V_{\text{ext}}(\mathbf{r}_i) \\ V_{\text{ext}}(\mathbf{r}_i) &= - \sum_{A=1}^M \frac{Z_A}{r_{iA}} \end{aligned} \quad (2.4)$$

can be split up into an potential referred as “external” potential  $V_{\text{ext}}$  acting on electron  $i$  due to the nuclei of charges  $Z_A$ .<sup>[117]</sup> The solution to the Schrödinger equation involving the electronic Hamiltonian

$$\mathbf{H}_{\text{elec}} \Psi_{\text{elec}} = E_{\text{elec}} \Psi_{\text{elec}} \quad (2.5)$$

is the electronic wave function

$$\Psi_{\text{elec}} = \Psi_{\text{elec}}(\mathbf{x}_1, \mathbf{x}_2, \dots, \mathbf{x}_N) \quad (2.6)$$

describing the motion of the electrons and depending explicitly on the electronic coordinates  $\mathbf{x}_i$  but parametrically on the nuclear coordinates. The electronic coordinates are comprised of space coordinates  $\mathbf{r}_i$  and spin coordinates  $s_i$ . To obtain the total energy

$$E_{\text{tot}} = E_{\text{elec}} + \sum_{A=1}^M \sum_{B<A}^M \frac{Z_A Z_B}{r_{AB}} \quad (2.7)$$

of a system with fixed nuclei, the Coulomb repulsion of the nuclei has to be added to the electronic energy  $E_{\text{elec}}$ . Equations 2.2 to 2.7 define the so-called electronic problem of many-electron systems that has to be solved by applying quantum mechanical models. In the following, the subscript “elec” will be dropped.

### Hartree-Fock approximation

The Hartree-Fock (HF) approximation is of substantial importance and introduces some fundamental concepts. Within the HF scheme, the wave function

$$\begin{aligned} \Psi \approx \Psi_{\text{HF}} = \Phi_{\text{SD}} &= \frac{1}{\sqrt{N!}} \begin{vmatrix} \chi_1(\mathbf{x}_1) & \chi_2(\mathbf{x}_1) & \cdots & \chi_N(\mathbf{x}_1) \\ \chi_1(\mathbf{x}_2) & \chi_2(\mathbf{x}_2) & \cdots & \chi_N(\mathbf{x}_2) \\ \vdots & \vdots & & \vdots \\ \chi_1(\mathbf{x}_N) & \chi_2(\mathbf{x}_N) & \cdots & \chi_N(\mathbf{x}_N) \end{vmatrix} \\ &= \frac{1}{\sqrt{N!}} \det [\chi_1 \chi_2 \cdots \chi_N] \end{aligned} \quad (2.8)$$

is approximated with a single Slater determinant consisting of  $N$  spin orbitals  $\chi_i(\mathbf{x}_i)$ .<sup>[118]</sup> These spin orbitals

$$\chi_i(x_i) = \phi_i(\mathbf{r}_i)\sigma(s_i) \quad (2.9)$$

with

$$\sigma(s_i) = \begin{cases} \alpha(s_i) \\ \text{or} \\ \beta(s_i) \end{cases} \quad (2.10)$$

are a product of a spatial orbital  $\phi_i(\mathbf{r}_i)$  and a spin function  $\sigma(s_i)$ .

## 2 Theoretical background

The expectation value of the Hamiltonian applied to a Slater determinant

$$\begin{aligned} E_{\text{HF}} &= \langle \Phi_{\text{SD}} | \mathbf{H} | \Phi_{\text{SD}} \rangle \\ &= \sum_i^N \langle i | \mathbf{h} | i \rangle + \frac{1}{2} \sum_{i,j=1}^N \langle ij | ij \rangle - \langle ij | ji \rangle \end{aligned} \quad (2.11)$$

is given by the HF energy  $E_{\text{HF}}$ .<sup>[119]</sup> This energy is composed of an integral  $\langle i | \mathbf{h} | i \rangle$  involving the core-Hamiltonian  $\mathbf{h}$  and the two-electron integrals  $\langle ij | ij \rangle$  and  $\langle ij | ji \rangle$  called Coulomb and exchange integrals, respectively. The HF energy

$$E_{\text{HF}} = E [\{\chi_i\}] \quad (2.12)$$

is a functional of the set of spin orbitals  $\{\chi_i\}$ . Minimization results in the HF equations

$$\mathbf{f}_i \chi_i = \varepsilon_i \chi_i \quad (2.13)$$

defined as  $N$  eigenvalue equations with the Fock operator  $\mathbf{f}_i$ , the spin orbitals  $\chi_i$  as eigenfunctions and the orbital energies  $\varepsilon_i$  as eigenvalues.<sup>[119]</sup> The Fock operator

$$\mathbf{f}_i = \mathbf{h} + \mathbf{V}_i^{\text{HF}} \quad (2.14)$$

is a sum of the core-Hamiltonian operator  $\mathbf{h}$  and an effective one-electron potential operator called the HF potential  $\mathbf{V}_i^{\text{HF}}$ .<sup>[118]</sup> The core-Hamiltonian operator

$$\begin{aligned} \mathbf{h} &= \mathbf{t}_e + \mathbf{v}_{\text{ne}} \\ &= -\frac{1}{2} \nabla_i^2 - \sum_{A=1}^M \frac{Z_A}{r_{iA}} \end{aligned} \quad (2.15)$$

is obtained from Eq. 2.2 by neglecting the electron-electron Coulomb repulsion energy operator and omitting the sum over all electrons to obtain the kinetic energy and potential energy for attraction to the nuclei of a single electron. The HF potential

$$\mathbf{v}_i^{\text{HF}} = \sum_j^N (\mathbf{J}_j - \mathbf{K}_j) \quad (2.16)$$



is composed of the Coulomb operator  $\mathbf{J}_j$  and the exchange operator  $\mathbf{K}_j$ . In contrast to the exact two electron repulsion operator  $\mathbf{V}_{ee}$  in the Hamiltonian (see Eq. 2.2), the Coulomb operator

$$\mathbf{J}_j(\mathbf{x}_1) = \int \chi_j^*(\mathbf{x}_2) \frac{1}{r_{12}} \chi_j(\mathbf{x}_2) d\mathbf{x}_2 \quad (2.17)$$

represents the averaged potential that an electron at position  $\mathbf{x}_1$  experiences from an electron in  $\chi_j$ .<sup>[118]</sup> The exchange operator

$$\mathbf{K}_j(\mathbf{x}_1)\chi_i(\mathbf{x}_1) = \left[ \int \chi_j^*(\mathbf{x}_2) \frac{1}{r_{12}} \chi_i(\mathbf{x}_2) d\mathbf{x}_2 \right] \chi_j(\mathbf{x}_1) \quad (2.18)$$

has no classical interpretation and is defined by its effect when operating on a spin orbital  $\chi_i(\mathbf{x}_1)$ . Following Eq. 2.9, the exchange operator involves the integration over the spin coordinate. Spin functions are orthonormal and accordingly the exchange energy only exists for electrons of equal spin. In Eq. 2.11, the term  $i = j$  is allowed describing the interaction of the average charge of an electron with itself which is called self-interaction.<sup>[119]</sup> In the case of the HF approximation, this self-interaction has no influence on the energy of the system, because for  $i = j$  the Coulomb and exchange operators are identical and the resulting HF potential is zero.

The HF equations (Eq. 2.13) are presented as linear eigenvalue equations, but should be denoted as pseudo-eigenvalue equations.<sup>[118]</sup> They involve the HF potential depending on the solution  $\{\chi_i\}$  of the pseudo-eigenvalue equations through the Fock operator. As a consequence, the HF equations have to be solved iteratively since the orbitals are derived from their own potentials. Therefore, a self-consistent field (SCF) approach has to be applied.

Finally, the approximation of the wave function of a many-electron system with a single Slater determinant results in an approximate treatment of the electron-electron repulsion. Accordingly, the Fock operator describes a system of  $N$  electrons that do not interact, but each electron experiences an averaged Coulomb potential arising by the other  $N - 1$  electrons. As a result, the motion of electrons is not correlated correctly and the kinetic energies as well as the nuclei-electron Coulomb energies are not exact. Therefore, the HF energy  $E_{\text{HF}}$  differs from the exact energy of a system with interacting electrons  $E$ . The difference

$$E_{\text{corr}}^{\text{HF}} = E - E_{\text{HF}} \quad (2.19)$$

is called correlation energy.<sup>[117]</sup> Consequently, a number of wave function based techniques has been developed to improve the HF approximation and account for the electron correlation.<sup>[119]</sup>

### 2.2.2 Kohn-Sham density functional theory

The density functional theory of electronic structure allows the replacement of an  $N$ -electron wave function depending on  $3N$  spatial variables and  $N$  spin coordinates with the electron density  $\rho(\mathbf{r})$  depending only on three spatial variables. This results in a drastic reduction of the computational effort for the treatment of many-electron systems.

#### Hohenberg-Kohn theorems

In 1964, Hohenberg and Kohn<sup>[120]</sup> presented their theorems and provided an exact energy functional  $E[\rho]$ . The first Hohenberg-Kohn theorem legitimizes the use of the electron density as basic variable. It states that the external potential “ $V_{\text{ext}}$  is (to within a constant) a unique functional of  $\rho(\mathbf{r})$ ”; since, in turn,  $V_{\text{ext}}$  fixes  $\mathbf{H}$  we see that the full many-particle ground state is a unique functional of  $\rho(\mathbf{r})$ ”.<sup>[120]</sup> This can be emphasized by the integral of the electron density

$$N = \int \rho(\mathbf{r}) d\mathbf{r} \quad (2.20)$$

determining the number of electrons  $N$ . Furthermore, the cusps in the density determine the positions of the nuclei and the heights of the cusps define the corresponding nuclear charges.<sup>[121]</sup> Therefore, the external potential is defined, the  $N$ -electron Schrödinger equation can be constructed and its solution determines the corresponding ground state. Consequently, the external potential defining the Hamiltonian and the corresponding energy  $E_V$  are a functional of the electron density  $\rho(\mathbf{r})$ . The energy functional for a given external potential

$$E_V[\rho] = T[\rho] + V_{\text{ne}}[\rho] + V_{\text{ee}}[\rho] \quad (2.21)$$

is given by the functionals of the kinetic energy  $T$  and the potential energies  $V$  of the nuclei-electron and electron-electron interaction.<sup>[117]</sup> This energy functional can be separated

$$E[\rho] = \int \rho(\mathbf{r})V_{\text{ext}}(\mathbf{r}) d\mathbf{r} + F_{\text{HK}}[\rho] \quad (2.22)$$

into the external potential  $V_{\text{ext}}$  (see Eq. 2.4) depending on the system and an universal system independent Hohenberg-Kohn (HK) functional  $F_{\text{HK}}$ .<sup>[119]</sup> This Hohenberg-Kohn functional

$$\begin{aligned} F_{\text{HK}}[\rho] &= T[\rho] + V_{\text{ee}}[\rho] \\ &= T[\rho] + J[\rho] + E_{\text{ncl}}[\rho] \end{aligned} \quad (2.23)$$

comprises the classical Coulomb repulsion energy

$$J[\rho] = \frac{1}{2} \int \int \frac{\rho(\mathbf{r}_1)\rho(\mathbf{r}_2)}{r_{12}} d\mathbf{r}_1 d\mathbf{r}_2 \quad (2.24)$$

and a non-classical functional  $E_{\text{ncl}}$ . The non-classical functional describes the electron-electron interaction containing the self-interaction correction, exchange and correlation, but its explicit expression is unknown.

The second Hohenberg-Kohn theorem provides the energy variational principle. It states that the energy functional provides an upper bound for any trial density  $\tilde{\rho}$  associated with an external potential  $\tilde{V}_{\text{ext}}$ . Accordingly, the energy functional of a system has a minimum for the ground state energy

$$E_0 = E[\rho_0] \leq E[\tilde{\rho}] \quad (2.25)$$

which is only obtained if the density is the true ground state density  $\rho_0$ . Consequently, the knowledge of the HK functional allows the determination of the ground state energy of any electronic system by minimizing the energy functional.<sup>[120]</sup>

## Kohn-Sham equations

In 1965, one year after the publication of the Hohenberg and Kohn theory, Kohn and Sham<sup>[122]</sup> presented their method allowing practical calculations using DFT. The Kohn-Sham (KS) theory invokes an reference system of non-interacting electrons using an universal functional  $F[\rho]$  in analogy to the HK theory. The corresponding Hamiltonian

$$\mathbf{H}_S = \sum_i^N -\frac{1}{2}\nabla_i^2 + \sum_i^N V_S(\mathbf{r}_i) \quad (2.26)$$

## 2 Theoretical background

contains a term for the kinetic energy and an effective KS potential  $V_S$  but no electron-electron Coulomb repulsion term.<sup>[117]</sup> Since this Hamiltonian describes a non-interacting system, the corresponding ground state wave function

$$\Psi = \Phi_S = \frac{1}{\sqrt{N!}} \det [\varphi_1 \varphi_2 \cdots \varphi_N] \quad (2.27)$$

is determinantal consisting of KS orbitals  $\varphi_i$  describing  $N$  non-interacting electrons in analogy to the determinantal HF wave function (see Eq. 2.8). This artificial non-interacting system is connected to the real interacting system by defining the effective potential  $V_S$  such that the resulting electron density

$$\rho_S(\mathbf{r}) = \sum_i^N \sum_s |\varphi_i(\mathbf{r}, s)|^2 = \rho_0(\mathbf{r}) \quad (2.28)$$

is exactly equal to the ground state electron density of the real system  $\rho_0$ .<sup>[119]</sup> These KS orbitals allow the exact calculation of the kinetic energy

$$T_S[\rho] = \sum_i^N \left\langle \varphi_i \left| -\frac{1}{2} \nabla^2 \right| \varphi_i \right\rangle \quad (2.29)$$

which is not equal to the kinetic energy of the interacting system in the HK theory  $T[\rho]$  but requires only a small correction.<sup>[117]</sup> Therefore, the universal functional

$$F[\rho] = T_S[\rho] + J[\rho] + E_{XC}[\rho] \quad (2.30)$$

is separated where

$$\begin{aligned} E_{XC}[\rho] &= (T[\rho] - T_S[\rho]) + (V_{ee}[\rho] - J[\rho]) \\ &= T_C[\rho] + E_{ncl}[\rho] \end{aligned} \quad (2.31)$$

is the so-called exchange-correlation (XC) energy. The first term of the XC energy is the residual part of the true kinetic energy  $T_C$  and the second term describes the non-classical part of the electron-electron interaction. Hence, the XC energy contains the non-classical effects of

self-interaction correction, exchange, and correlation contributing to the potential energy and in addition a contribution to the kinetic energy. Finally, the total energy of the system

$$E[\rho] = \int \rho(\mathbf{r})V_S(\mathbf{r}) d\mathbf{r} + F[\rho] \quad (2.32)$$

is defined in analogy to the HK theory. To obtain the electron density  $\rho(\mathbf{r})$  for a given effective potential  $V_S$ ,  $N$  one-electron equations

$$\left[ -\frac{1}{2}\nabla^2 + V_S(\mathbf{r}) \right] \varphi_i = \varepsilon_i \varphi_i \quad (2.33)$$

corresponding to the Hamiltonian  $\mathbf{H}_S$  (see Eq. 2.26) have to be solved. The KS potential

$$\begin{aligned} V_S(\mathbf{r}) &= V_{\text{ext}}(\mathbf{r}) + \frac{\delta J[\rho]}{\delta \rho(\mathbf{r})} + V_{\text{XC}}(\mathbf{r}) \\ &= V_{\text{ext}}(\mathbf{r}) + \int \frac{\rho(\mathbf{r}_2)}{r_{12}} d\mathbf{r}_2 + \frac{\delta E_{\text{XC}}[\rho]}{\delta \rho(\mathbf{r})} \end{aligned} \quad (2.34)$$

is composed of the external potential  $V_{\text{ext}}$  (see Eq. 2.2), an electron-electron Coulomb repulsion potential and an XC potential defined by the XC energy.

Analog to the HF equations, the KS one-electron equations have to be solved iteratively by applying an SCF approach. Starting with an initial guess of the electron density, the KS potential is calculated (Eq. 2.34). Subsequently, the KS equations are solved determining the KS orbitals (Eq. 2.33). From these orbitals the electron density is obtained (Eq. 2.28) and the corresponding energy is calculated (Eq. 2.32). By using the energy variational principle of the HK theory, the ground state energy of the system is obtained (Eq. 2.25). In contrast to the HF approximation which is based on the approximation of a determinantal wave function, KS theory is exact. Approximations are only made upon the decision of an explicit form of the XC energy functional. Nevertheless, the XC energy has only a very small contribution to the energy.<sup>[123]</sup> Therefore, a reasonable approximation of the XC functional results in a very good approximation of the universal functional  $F$ . Consequently, KS-DFT is a widely and successfully applied quantum chemistry method. Finally, Walter Kohn received the Nobel Prize in Chemistry 1998 for his contributions to the foundations of modern DFT.<sup>[124]</sup>

### Exchange-correlation energy functionals

To perform KS-DFT calculations, the XC energy functional  $E_{\text{XC}}[\rho]$  (XC functional) has to be approximated. The approximations and the corresponding explicit forms of the XC functional are attributed to different levels of theory. The hierarchy of these XC functional approximations is determined in analogy to “Jacobs’s ladder” connecting earth to heaven.<sup>[125]</sup> The kind of ladder lifts up from the “Hartree World” consisting of the Hartree approximation neglecting the XC energy completely and the HF approximation neglecting the correlation energy to the “heaven of chemical accuracy”.<sup>[125]</sup> Therefore higher rungs are typically more accurate but also more computationally demanding than lower ones. In general, the construction of XC functionals can be performed by relying on fundamental constants (*ab initio*) or by fitting a functional form depending on parameters (semi-empirical) to a set *e. g.* energies or molecular geometries.<sup>[125]</sup>

The first rung of XC functional approximations has already been presented in the original paper by Kohn and Sham in 1965. The approximation is based on the uniform electron gas and the corresponding XC energy per electron  $\epsilon_{\text{XC}}$ . This results in the local density approximation (LDA)

$$E_{\text{XC}}^{\text{LDA}}[\rho] = \int \rho(\mathbf{r})\epsilon_{\text{XC}}(\rho(\mathbf{r})) d\mathbf{r} \quad (2.35)$$

in which the XC energy density  $\epsilon_{\text{XC}}(\rho)$  of a homogeneous electron gas of electron density  $\rho$  is weighted by the electron density  $\rho$  of the real and inhomogeneous system. It is called local because it only depends on the local electron density  $\rho(\mathbf{r})$  of the system. The LDA is a drastic approximation because the inhomogeneous electron density of molecules and atoms comes not even close to the uniform electron gas. Nevertheless, LDA gives remarkably accurate bond lengths and equilibrium structures.<sup>[119,126]</sup>

The shortcomings of LDA functionals were improved by involving the density gradient  $\nabla\rho$ . The resulting approximation

$$E_{\text{XC}}^{\text{GGA}}[\rho] = \int \rho(\mathbf{r})\epsilon_{\text{XC}}^{\text{GGA}}(\rho(\mathbf{r}), \nabla\rho(\mathbf{r})) d\mathbf{r} \quad (2.36)$$

is called generalized gradient approximation (GGA) and represents the second rung.<sup>[125]</sup> A very prominent GGA functional is the parametrization of Perdew, Burke, and Ernzerhof denoted as PBE functional.<sup>[127]</sup> All parameters present in the PBE functional are fundamental constants.

To obtain further improved approximations, the KS orbital kinetic energy density

$$\tau = \frac{1}{2} \sum_i^N |\nabla \varphi_i(\mathbf{r})|^2 \quad (2.37)$$

is comprised. The corresponding functionals

$$E_{\text{XC}}^{\text{mGGA}}[\rho] = \int \rho(\mathbf{r}) \varepsilon_{\text{XC}}^{\text{GGA}}(\rho(\mathbf{r}), \nabla \rho(\mathbf{r}), \tau) d\mathbf{r} \quad (2.38)$$

form the third rung and are known as meta-GGA (mGGA) functionals.

The systematic improvement of XC functional approximations is generally limited by the self-interaction error and long-range dynamic correlation. Therefore, the exact exchange energy known from HF theory (Sec. 2.2.1) is mixed with DFT XC functionals to overcome the limitations due to the self-interaction error.<sup>[126]</sup> The resulting functionals are denoted as hybrids and form the fourth rung. These hybrid functionals can be constructed for example by using GGA functionals leading to hybrid GGA (hGGA) functionals. Typically only a fraction  $c_X$  of exact exchange energy  $E_X$  is mixed globally with the DFT XC functionals

$$E_{\text{XC}}^{\text{GH}} = c_X E_X^{\text{HF}} + (1 - c_X) E_X^{\text{DFT}} + E_C^{\text{DFT}} \quad (2.39)$$

yielding global hybrid (GH) functionals.<sup>[128]</sup> The fraction of exact exchange energy  $c_X$  is often between 20 and 25%.<sup>[119]</sup> Two very popular and widely used hybrid functionals are B3LYP and PBE0. The B3LYP functional is a semi-empirical functional using 20% exact exchange energy, while the PBE0 functional is based on the non-empirical PBE functional and uses 25% exact exchange energy.<sup>[129,130]</sup> In contrast to global hybrid functionals, the exact exchange contribution can be range-separated into a short-range (sr) and a long-range (lr) contribution using the range-splitting parameter  $\omega$

$$E_{\text{XC}}^{\text{RSH}} = c_X E_X^{\text{HF,sr}}(\omega) + (1 - c_X) E_X^{\text{DFT,sr}}(\omega) + c_X E_X^{\text{HF,lr}}(\omega) + (1 - c_X) E_X^{\text{DFT,lr}}(\omega) + E_C^{\text{DFT}} \quad (2.40)$$

resulting in range-separated hybrid functionals (RSH).<sup>[128]</sup> The HSE06 hGGA functional used in this work is an example for this approach. It is based on the non-empirical PBE XC functional and involves 25% exact exchange energy.<sup>[27]</sup> In contrast to the general definition of RSH functionals given above, the HSE06 functional only involves the exact exchange energy as short-range

## 2 Theoretical background

contribution.<sup>[131]</sup> Consequently, the HSE06 functional is equivalent to the PBE0 functional at short ranges and reaches the pristine PBE functional for long ranges.

Finally, the fifth rung of the ladder is given by double hybrid functionals. These functionals involve additionally to the HF exchange a second hybrid construction for the correlation energy.<sup>[132]</sup>

None of the approximations discussed above accounts for long-range dynamic electron correlation leading to dispersion interactions. The approximations of rungs one to four typically show an exponential long-range decay instead of a proper  $r^{-6}$  decay.<sup>[128]</sup> A very popular method to improve the dispersion interactions in KS-DFT was developed by Grimme and co-workers.<sup>[26]</sup> This method adds an dispersion correction energy  $E_{\text{disp}}$  to the energy obtained with KS-DFT

$$E_{\text{DFT-D}} = E_{\text{KS-DFT}} + E_{\text{disp}} \quad (2.41)$$

to obtain an dispersion corrected energy.<sup>[133]</sup> In its initial version and first revision (DFT-D2), this method was based on an empirical two-body dispersion correction

$$E_{\text{disp}} = -s_6 \sum_{i=1}^{N-1} \sum_{j=i+1}^N \frac{C_6^{ij}}{R_{ij}^6} f_{\text{dmp}}(R_{ij}) \quad (2.42)$$

describing the atom pairs  $ij$ . It comprises a global scaling coefficient  $s_6$  depending on the used XC functional, the interatomic distance  $R_{ij}$ , a dispersion coefficient for the atom pairs  $C_6^{ij}$  and a damping function  $f_{\text{dmp}}$  for small interatomic distances. The damping function

$$f_{\text{dmp}}(R_{ij}) = \frac{1}{1 + e^{-d(R_{ij}/R_r - 1)}} \quad (2.43)$$

involves the sum of the atomic van der Waals radii  $R_r$  and a factor  $d$  defining the steepness of the damping function. In the later revisions DFT-D3 and DFT-D4, additional three- and many-body terms were introduced depending on the geometrical arrangement of the atoms and the system size.<sup>[134,135]</sup>

In contrast to the DFT-D2 method, Tkatchenko and Scheffler<sup>[136]</sup> developed a two-body dispersion correction method incorporating the chemical environment of each atom. Therefore, the dispersion coefficients for the atom pairs  $C_6^{ij}$  are derived from the electron density of a



molecule or solid by a summation of all dispersion coefficients of the respective molecule or solid. This approach is denoted as vdW-TS method and the dispersion corrected energy

$$E_{\text{disp}} = -\frac{1}{2} \sum_{i=1}^{N-1} \sum_{j=i+1}^N \frac{C_6^{ij}}{R_{ij}^6} f_{\text{dmp}}(R_{ij}) \quad (2.44)$$

is calculated without a global scaling coefficient. Instead, the damping function

$$f_{\text{dmp}}(R_{ij}) = \frac{1}{1 + e^{-d(R_{ij}/(R_{rSR})-1)}} \quad (2.45)$$

includes a scaling coefficient  $s_R$  depending on the XC functional.

Both, the DFT-D2 and the vdW-TS method are used in this work in combination with GGA XC functionals to obtain accurate molecular geometries.

## Basis sets

By selecting an approximation of the XC functional at the desired level, the KS equations can be solved. In principle, this is possible by a numerical approach resulting in a high computational demands. Therefore, a set of predefined basis functions is used to reduce the computational effort. These sets of  $L$  basis functions  $\eta_\mu$  are used in a linear expansion

$$\varphi_i = \sum_{\mu}^L c_{i,\mu} \eta_\mu \quad (2.46)$$

to approximate the KS orbitals.<sup>[119]</sup> In general, basis sets can be composed of atomic orbitals or plane waves. The first type of basis set is mostly applied to molecules, while the latter type of basis sets is used to describe solid state systems.

Calculations based on atomic orbitals basis sets correspond to the linear combination of atomic orbitals (LCAO) method to construct molecular orbitals.<sup>[119]</sup> Atomic orbitals-based basis sets can be constructed by Slater-type-orbitals (STOs) or Gaussian-type-orbitals (GTOs).<sup>[137,138]</sup> GTO basis sets are widely used because of their computational advantages. They have the general form

$$\eta^{\text{GTO}}(r) = N x^l y^m z^n e^{-\alpha r^2} \quad (2.47)$$

with a normalization coefficient  $N$ .<sup>[119]</sup> The sum  $l + m + n$  defines the type of orbital where 0 corresponds to an s-orbital and 1 to a p-orbital. The coefficient  $\alpha$  determines the radial extent

## 2 Theoretical background

of the functions. Large values result in functions with a compact shape describing the shape of orbitals near the nucleus and small values provide functions with a diffuse shape describing the long-range behavior of orbitals far from the nucleus.<sup>[139]</sup> Therefore, a series of GTOs with different values of  $\alpha$  is required to obtain a suitable description of the complete shape of an orbital. A function as defined in Eq. 2.47 is called primitive GTO. Sets of primitive GTOs are combined as fixed linear combinations

$$\eta^{\text{CGTO}} = \sum_a^A d_a \eta_a^{\text{GTO}} \quad (2.48)$$

forming so-called contracted GTOs (CGTOs) to describe specific orbitals *e. g.* the 1s-orbital.<sup>[139]</sup> As a result, the inner parameters  $d_a$  of a CGTO have not to be determined by the variational principle. This is widely applied to core orbitals describing the inner electrons. These orbitals require a larger number of GTOs to represent the wave function cusp near the nucleus. Therefore, the number of functions  $c_{i,\mu}$  distributed to the energetic important core orbitals is reduced by using CGTOs. This allows to reduce the computational effort and distribute more functions to the chemical important valence orbitals. Typically, an  $nZ$  notation is used to indicate the number of contracted basis functions  $n$  involved in the construction of the basis set, *e. g.*  $n = 2$  corresponds to a double zeta (DZ) quality. In this work, the GTO-based Karlsruhe-type basis sets are deployed which are available for a large fraction of elements in the periodic table.<sup>[140]</sup>

In contrast to atomic orbital basis sets, plane wave basis sets do not comply with the LCAO method. The basis functions are not centered at the nuclei but have the form of solutions of the Schrödinger equation describing free electrons. These solutions have the general form of plane waves (PWs)

$$f_{\text{PW}}(\mathbf{r}) = e^{i\mathbf{k}\mathbf{r}} \quad (2.49)$$

described with the wave vector  $\mathbf{k}$  and extending through the complete space.<sup>[119]</sup> Therefore, PW basis sets are mainly applied to solid state systems. By using Bloch's theorem, PWs can be used to construct a basis set

$$\varphi_{i,\mathbf{k}}^{\text{PW}}(\mathbf{r}) = e^{i\mathbf{k}\mathbf{r}} u_{\mathbf{k}}(\mathbf{r}) \quad (2.50)$$

describing a periodic system with a periodic cell defined by the lattice vectors  $\mathbf{a}_1$ ,  $\mathbf{a}_2$  and  $\mathbf{a}_3$ .<sup>[141]</sup> The function  $u_{\mathbf{k}}$  is periodic in space with the periodicity of the system

$$u_{\mathbf{k}}(\mathbf{r} + n_1\mathbf{a}_1 + n_2\mathbf{a}_2 + n_3\mathbf{a}_3) = u_{\mathbf{k}}(\mathbf{r}) \quad (2.51)$$

### 2.3 Quantum mechanical calculation of the refractive index

for any integers  $n_1, n_2$  and  $n_3$ . Analog to the real space, a reciprocal lattice vector

$$\mathbf{G} = m_1 \mathbf{b}_1 + m_2 \mathbf{b}_2 + m_3 \mathbf{b}_3 \quad (2.52)$$

can be defined with the vectors of the Brillouin zone  $\mathbf{b}_1, \mathbf{b}_2$  and  $\mathbf{b}_3$  with any integers  $m_1, m_2$  and  $m_3$ . The periodicity of the function  $u_{\mathbf{k}}$  allows an expansion as a set of PW

$$u_{\mathbf{k}}(\mathbf{r}) = \sum_{\mathbf{G}} c_{\mathbf{G}} e^{i\mathbf{G}\cdot\mathbf{r}} \quad (2.53)$$

as a sum over the reciprocal lattice vector.<sup>[141]</sup> Combining Eq. 2.50 and 2.53 results in

$$\varphi_{i,\mathbf{k}}^{\text{PW}}(\mathbf{r}) = \sum_{\mathbf{G}} c_{i,\mathbf{k}+\mathbf{G}} e^{i(\mathbf{k}+\mathbf{G})\cdot\mathbf{r}} \quad (2.54)$$

a basis set of PWs. This basis set allows to solve the KS equations at each point in the Brillouin zone  $\mathbf{k}$  separately by summing over an infinite number of possible values of  $\mathbf{G}$ . Each basis function can be interpreted as a solution of the Schrödinger equation for a free electron. Therefore, a kinetic energy

$$E = \frac{1}{2} |\mathbf{k} + \mathbf{G}|^2 \quad (2.55)$$

is associated with every PW where high kinetic energies correspond to PW oscillating on short length scales in real space. Consequently, the sum over  $\mathbf{G}$  in Eq. 2.54 is truncated by including only plane waves with kinetic energy values less than a cutoff value  $E_{\text{cut}}$  to limit the basis set to physically relevant wave functions.<sup>[141]</sup>

Finally, the quality of a KS-DFT calculation depends on two approximations and their respective qualities. The first approximation is required due to the unknown explicit form of the XC functional. The quality of the XC functional approximation is defined by the rung of the used XC functional. The second approximation is introduced by the use of basis sets. The quality of a basis set is indicated by the  $nZ$  notation or cutoff energy  $E_{\text{cut}}$ , respectively.

## 2.3 Quantum mechanical calculation of the refractive index

In the following section, the physical foundations of the optical properties in the solid state are elucidated with a focus on the refractive index. Afterwards, two approaches for the calculation of the index of refraction using quantum mechanical (QM) methods are illustrated. These two

## 2 Theoretical background

approaches are the basis of the calculations of the refractive index of MOFs performed in this work.

### 2.3.1 General background of the optical properties in the solid state

In general, the optical properties in the solid state can be ascribed to three phenomena. These phenomena are the reflection, propagation, and transmission of electromagnetic radiation and light, respectively.<sup>[142]</sup> The propagation of light in an optical medium is mainly characterized by three phenomena as well. The phenomena can be differentiated into the scattering, absorption, and refraction of light by the optical medium. Furthermore, so-called non-linear effects can be observed for high beam intensities.

#### The complex refractive index

The refraction of light is caused by the slower propagation of light in an optical medium compared to the propagation in vacuum and is described by the refractive index.<sup>[142]</sup> The refractive index  $n$

$$n = \frac{v}{c} \quad (2.56)$$

is defined by the ratio of the speed of light propagating in a medium  $v$  and the speed of light in the vacuum  $c$ . In addition, the RI is frequency-dependent

$$n = n(\omega), \quad (2.57)$$

thus the propagation speed of light in an optical medium is frequency-dependent leading to a dispersion of the propagation speed. The reduction of the propagation speed of light in an optical medium results in the refraction of a light beam at the interface of two different optical media. The change in the direction of the light beam is described by Snell's law

$$\frac{n_1}{n_2} = \frac{\sin \varphi_2}{\sin \varphi_1} \quad (2.58)$$

and depends on the ratio of the RIs  $n_1$  and  $n_2$  of the two optical media 1 and 2, respectively, resulting in a change of the ratio of the angles of the light beams normal to the interface  $\varphi_1$  and  $\varphi_2$ .<sup>[143]</sup> The reduction of the propagation speed of light in an optical medium is caused by

### 2.3 Quantum mechanical calculation of the refractive index

the interaction of the light as an oscillating electromagnetic wave with charge carriers and not by absorption of the light. Nevertheless, the RI can be related with the absorption of light

$$n^* = n + ik \quad (2.59)$$

resulting in the complex refractive index  $n^*$ . The real part of the complex refractive index is given by  $n$  and the imaginary part  $k$  is called extinction coefficient or attenuation index.<sup>[143]</sup> The linking of the RI describing the dispersion of the propagation speed of light as a function of the frequency and the extinction coefficient describing the absorption of light

$$n^*(\omega) = n(\omega) + ik(\omega) \quad (2.60)$$

is called dispersion relation.<sup>[144]</sup> By using the Kramers-Kronig relations correlating the real and imaginary part of a response function, the so-called Kramers-Kronig dispersion relations

$$n(\omega) = 1 + \frac{2}{\pi} \mathcal{P} \int_0^{\infty} \frac{\omega' k(\omega')}{(\omega')^2 - \omega^2} d\omega' \quad (2.61)$$

and

$$k(\omega) = -\frac{2}{\pi} \mathcal{P} \int_0^{\infty} \frac{n(\omega') - 1}{(\omega')^2 - \omega^2} d\omega' \quad (2.62)$$

relating the real and imaginary part of the complex refractive index  $n$  and  $k$ , respectively, can be obtained.<sup>[143,145]</sup> Here,  $\mathcal{P}$  denotes the Cauchy principal value,  $\omega$  represents a pole, *e. g.* a resonance frequency of the system, and  $\omega'$  is the frequency of the light. The extinction coefficient  $k$  allows the derivation of the absorption coefficient  $\alpha$

$$\alpha(\omega) = \frac{2\omega}{c} k(\omega) = \frac{4\pi}{\lambda} k(\omega) \quad (2.63)$$

by incorporating the speed of light  $c$ , the frequency  $\omega$  and the wavelength  $\lambda$ , respectively.<sup>[143]</sup> The absorption coefficient  $\alpha$  is used to quantify the absorption of light with Lambert's law

$$I(z) = I_0 e^{-\alpha(\omega)z} \quad (2.64)$$

## 2 Theoretical background

relating the intensity of an incident light beam  $I_0$  with the transmitted intensity  $I$  through a medium with the thickness  $z$ .<sup>[146]</sup> Besides the absorption, refraction, and transmission of light, the reflection of light can occur. From the Fresnel equations a relation for the frequency-dependent reflectivity  $R$  describing the reflection of light at normal incidence

$$R(\omega) = \frac{(n(\omega) - 1)^2 + k^2(\omega)}{(n(\omega) + 1)^2 + k^2(\omega)} \quad (2.65)$$

can be obtained as a function of  $n$  and  $k$ .<sup>[144]</sup>

The complex dielectric function

From the Maxwell equations a relation between the RI  $n$  and the dielectric function  $\varepsilon$

$$n = \sqrt{\varepsilon} \quad (2.66)$$

can be derived.<sup>[142]</sup> The dielectric function

$$\varepsilon^*(\omega) = \varepsilon_1(\omega) + i\varepsilon_2(\omega) \quad (2.67)$$

is as well as the RI a complex and frequency-depending function. Using Eq. 2.66 the complex refractive index  $n^*$  can be related with the complex dielectric function

$$n^*(\omega) = n(\omega) + ik(\omega) = \sqrt{\varepsilon_1(\omega) + i\varepsilon_2(\omega)}. \quad (2.68)$$

The imaginary part of the dielectric function  $\varepsilon_2$  describes the absorption of energy analogous to the extinction coefficient  $k$ . The real and imaginary part of the dielectric function are not independent and also linked by the Kramers-Kronig dispersion relations

$$\varepsilon_1(\omega) = 1 + \frac{2}{\pi} \mathcal{P} \int_0^{\infty} \frac{\omega' \varepsilon_2(\omega')}{(\omega')^2 - \omega^2} d\omega' \quad (2.69)$$

and

$$\varepsilon_2(\omega) = -\frac{2}{\pi} \mathcal{P} \int_0^{\infty} \frac{\varepsilon_1(\omega') - 1}{(\omega')^2 - \omega^2} d\omega'. \quad (2.70)$$

### 2.3 Quantum mechanical calculation of the refractive index

Eq. 2.68 leads to

$$\varepsilon_1(\omega) = n^2(\omega) - k^2(\omega) \quad (2.71)$$

and

$$\varepsilon_2(\omega) = 2n(\omega)k(\omega) \quad (2.72)$$

as expressions of  $n$  and  $k$  for the real and imaginary part of the dielectric function  $\varepsilon_1$  and  $\varepsilon_2$ , respectively. This results in

$$n(\omega) = \sqrt{\frac{\sqrt{\varepsilon_1^2(\omega) + \varepsilon_2^2(\omega)} + \varepsilon_1(\omega)}{2}} \quad (2.73)$$

and

$$k(\omega) = \sqrt{\frac{\sqrt{\varepsilon_1^2(\omega) + \varepsilon_2^2(\omega)} - \varepsilon_1(\omega)}{2}} \quad (2.74)$$

as relations for the calculation of the refractive index  $n$  and extinction coefficient  $k$  using the complex dielectric function. Finally, by using the Kramers-Kronig dispersion relations, the sole knowledge of the real or imaginary part of the dielectric function is sufficient to calculate the real and imaginary part of the complex refractive index by using Eq. 2.73 and 2.74.

#### The Lorentz oscillator

The Lorentz oscillator is a classical model describing atoms with electrons bound to the nucleus in an analogous way to the bonding of a small mass to a larger mass connected by a spring. This harmonic oscillator model allows the mathematical description of electrons excited by an electric field leading to the frequency dependence of the polarizability and dielectric function of a solid. The model is based on two assumptions. First, the mass of the nucleus is infinite, which is quite accurate when the mass of an electron is compared to the mass of a nucleus. Second, the force arising from the interaction of the electron with the magnetic field of the light

## 2 Theoretical background

wave is neglected, because this force is low due to the small velocity of the electron compared to the speed of light  $c$ . This results in

$$\varepsilon_1(\omega) = 1 + \frac{4\pi N e^2}{m} \frac{(\omega_0^2 - \omega^2)}{(\omega_0^2 - \omega^2)^2 + \Gamma^2 \omega^2} \quad (2.75)$$

and

$$\varepsilon_2(\omega) = \frac{4\pi N e^2}{m} \frac{\Gamma \omega}{(\omega_0^2 - \omega^2)^2 + \Gamma^2 \omega^2} \quad (2.76)$$

as expressions for the real and imaginary part of the dielectric function  $\varepsilon_1$  and  $\varepsilon_2$ , respectively.<sup>[144]</sup> In this context,  $N$  is the number of atoms per volume,  $e$  is the elementary charge,  $m$  is the mass of the excited electron,  $\Gamma$  is a damping coefficient and describes the energy loss in a solid and  $\omega_0$  is the resonance frequency of the excited electron. In the case of semi-conducting or insulating materials, the resonance frequency  $\omega_0$  corresponds to the excitation of electrons from the valence band into the conduction band, which is called interband transition. The curves of the real and imaginary part of the dielectric function for a single resonance frequency are shown in Fig. 2.9. The full width at half maximum (FWHM) of the imaginary part of the dielectric function  $\varepsilon_2$  at a given resonance frequency  $\omega_0$  is determined by the damping coefficient  $\Gamma$ . In addition, the frequencies of the minimum  $\omega_{\min}$  and maximum  $\omega_{\max}$  of the real part of the dielectric function  $\varepsilon_1$  at a given resonance frequency  $\omega_0$  can be calculated from the damping coefficient  $\Gamma$

$$\omega_{\max} = \omega_0 - \frac{\Gamma}{2} \text{ and } \omega_{\min} = \omega_0 + \frac{\Gamma}{2} . \quad (2.77)$$

The maximum value of  $\varepsilon_2$

$$\varepsilon_{2,\max} = \frac{4\pi N e^2}{m \omega_0 \Gamma} \quad (2.78)$$

is found at  $\omega_0$ . In general,  $\varepsilon_1$  increases with increasing frequency, which is denoted as normal dispersion. In the region of  $\omega_0$  between  $\omega_{\max}$  and  $\omega_{\min}$  the real part of the dielectric function decreases, which is called anomalous dispersion.

Using Eq. 2.73, 2.74 and 2.65 the RI, extinction coefficient, and reflectivity can be calculated from the dielectric function obtained with the Lorentz oscillator model. The resulting curves are shown in Fig. 2.10. In the region with frequencies much larger than the resonance frequency  $\omega_0$ , the imaginary part of the dielectric function  $\varepsilon_2$  is zero and the real part of the dielectric function  $\varepsilon_1$  is larger than 1 (see Fig. 2.9). Furthermore, the analysis of Eq. 2.72 and 2.71 in this



### 2.3 Quantum mechanical calculation of the refractive index

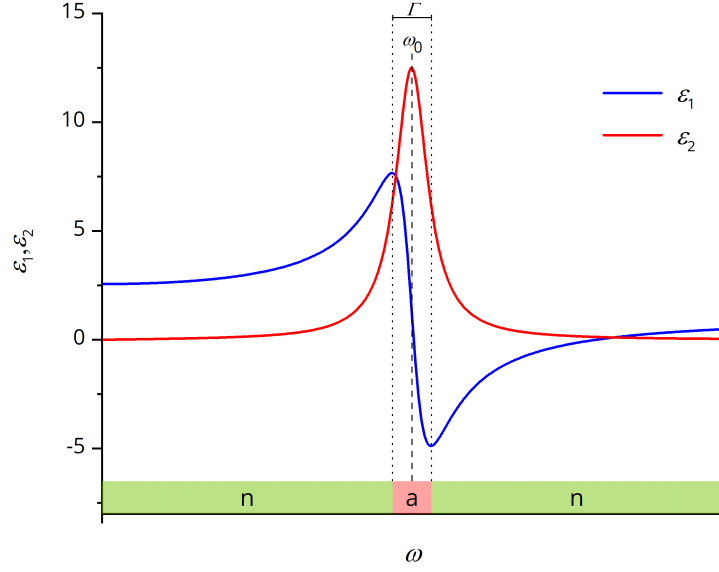


Figure 2.9: Frequency dependence of the real (blue) and imaginary (red) part of the dielectric function  $\epsilon_1$  and  $\epsilon_2$ , respectively, calculated with the Lorentz oscillator model. The position of the maximum of the imaginary part is determined by the resonance frequency  $\omega_0$  and the FWHM is given by the damping coefficient  $\Gamma$ . In the green region,  $\epsilon_1$  has a normal dispersion (n) and in the red region anomalous (a) dispersion can be observed. The functions were calculated with  $\omega_0 = 268$  THz,  $\Gamma = \omega_0/8$  and  $(4\pi N e^2)/m = 312.5 \omega_0$ .

region shows that the extinction coefficient  $k$  is also zero and the RI is larger than one leading to the relation

$$\epsilon_1 = n^2. \quad (2.79)$$

In this region, no absorption (resulting in a high transparency) paired with a low reflectivity is observed (see Fig. 2.10). In the region near the resonance frequency  $\omega_0$ ,  $\epsilon_2$  and  $k$  show maxima, where the maximum of  $k$  (see Fig. 2.10) is shifted to slightly higher frequencies compared to  $\epsilon_2$  (see Fig. 2.9). In addition, the reflectivity has remarkable values, meaning that all the non-absorbed light is strongly reflected. At frequencies larger than the resonance frequency  $\omega_0$ , the photon energy is much larger than the binding energy of the electrons resulting in electrons with a response analogous to free electrons in a metal. As a result, the reflectivity dominates and leads to a metallic reflectance (see Fig. 2.10).

In the case of silicon, these correlations of the optical properties can be observed even visually. The band gap energy and the corresponding interband transitions of silicon are located in the infrared (IR) spectral region of the light. Due to this, the region of high reflectivity of silicon is

## 2 Theoretical background

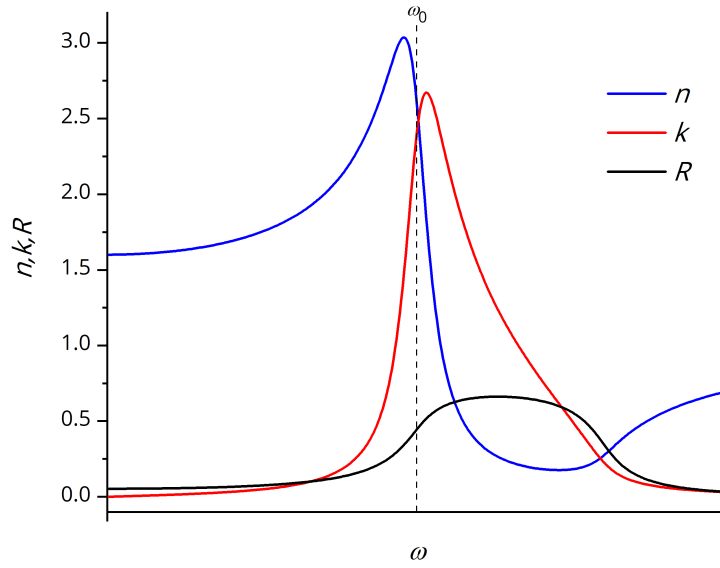


Figure 2.10: Frequency dependence of the refractive index  $n$  (blue), extinction coefficient  $k$  (red) and reflectivity  $R$  (black) calculated with the Lorentz oscillator model. The resonance frequency  $\omega_0$  is highlighted. The comparison of  $n$  with  $\epsilon_1$  from Fig. 2.9 at frequencies  $\omega \ll \omega_0$  illustrates the relation given by Eq. 2.79 ( $n = 1.6$  and  $\epsilon_1 = 2.56$ ). The functions were calculated with  $\omega_0 = 268$  THz,  $\Gamma = \omega_0/8$  and  $(4\pi N e^2)/m = 312.5 \omega_0$ .

found at higher frequencies corresponding to the visible (Vis) spectral region leading to the metallic appearance of crystalline silicon.

### The refractive index of materials

Typical materials used in optical applications like glass or polymers possess absorption of UV light leading to a transparency in the Vis spectral region. Accordingly, these materials have a low reflectivity and a RI with normal dispersion in the Vis region. The corresponding real and imaginary parts of the complex dielectric function and complex refractive index are shown in Fig. 2.11. Using the Lorentz oscillator model described above, the fundamental absorption of a material given by its band gap  $E_g$  can be related to a resonance frequency  $\omega_0$

$$E_g = \hbar\omega_0 . \quad (2.80)$$

The shift of the resonance frequency to higher values (smaller wavelengths) corresponds to a shift of the dielectric function to higher frequencies and results in a shift of the RI in the Vis region to lower values (see Fig. 2.11). Accordingly, an increase of the band gap energy leads to a decrease of the RI values in the Vis region and a decrease of the band gap energy results in an increase of the RI values in the Vis region. Furthermore, the magnitude of the dielectric function described by the Lorentz oscillator is determined by the number of atoms per volume  $N$ . As a result, an increase of the density of a material leads to an increase of the RI in the Vis region.

Compared to the UV region, the dispersion of the RI is considerably smaller in the Vis region. Thus, it is suitable to describe the RI of a material with a single value  $n_D$ . This RI value is taken from the dispersion curve of the RI at a wavelength of 589 nm or measured at 589 nm, respectively.<sup>[147]</sup> This wavelength corresponds to the sodium D-line (D<sub>1</sub> and D<sub>2</sub> doublet), which is commonly used in refractometers as monochromatic light source. Additionally, the Abbe number  $\nu_d$  can be used to characterize the dispersion of a material in the Vis region. This classification number

$$\nu_d = \frac{n_d - 1}{n_F - n_C} \quad (2.81)$$

is calculated with the RI values at different Fraunhofer lines d also labeled D<sub>3</sub> (587,6 nm), F (486,1 nm) and C (656,3 nm).<sup>[148]</sup> The values of the Abbe number lie typically between 15 and 100 with high values representing a low dispersion.

## 2 Theoretical background

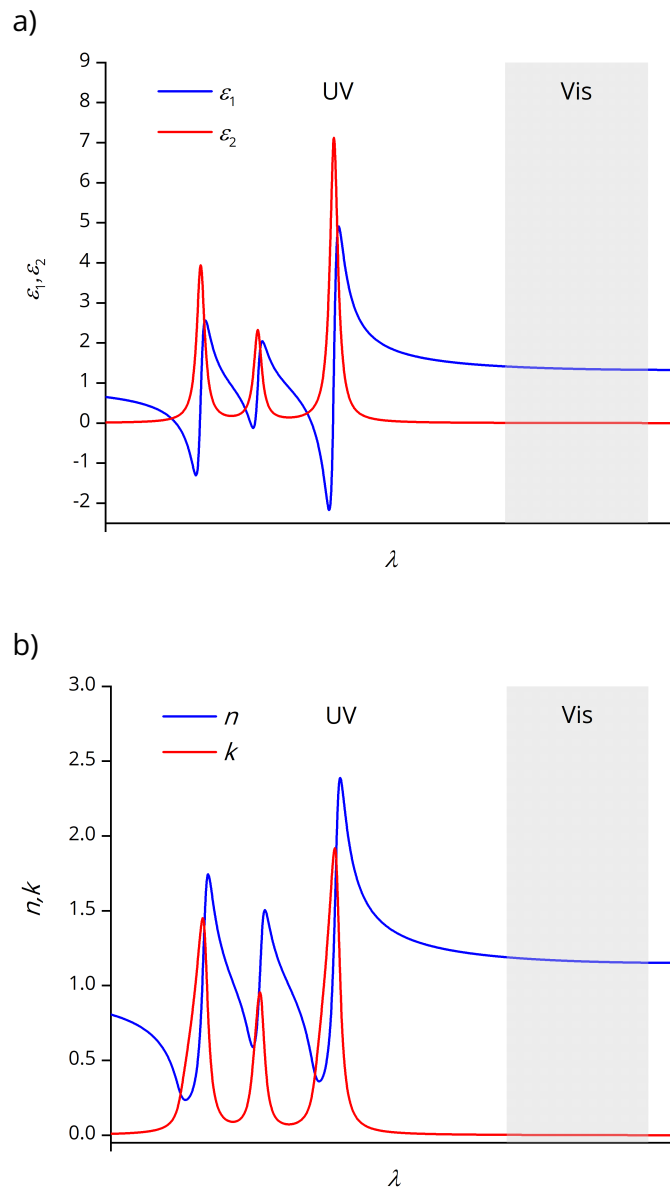


Figure 2.11: Schematic representation of the complex refractive index and the dielectric function as a function of the wavelength  $\lambda$  of a material for optical applications. The material only shows absorption of light in the UV region. a) real (blue) and imaginary (red) part of the dielectric function  $\epsilon_1$  and  $\epsilon_2$ , respectively, with maxima of  $\epsilon_2$  in the UV region. b) real (blue) and imaginary (red) part of the complex refractive index  $n$  and  $k$ , respectively, with maxima of the extinction coefficient  $k$  in the UV region. Accordingly, the material is transparent in the Vis region (gray) and the RI  $n$  has a normal dispersion in the Vis region.

### 2.3.2 Methods for the calculation of the refractive index

In this work, two approaches for the calculation of the refractive index of materials were applied to MOFs. Both approaches rely on QM methods allowing the calculation of the optical properties of a material. The first approach is based on the QM calculation of the imaginary part of the dielectric function. By applying the Kramers-Kronig dispersion relations and the equations for the complex refractive index derived from the Maxwell equations, the refractive index can be calculated. The second approach is based on the QM calculation of the polarizability. By using the Lorenz-Lorentz equation, the refractive index can be calculated.

#### Dielectric function approach

Ehrenreich and Cohen<sup>[149]</sup> derived the complex, frequency-dependent dielectric function for a free-electron gas and a real solid by applying the SCF approach. Within the SCF approach, a many-electron system is described by a time-dependent interaction of a single electron with a self-consistent electric field. The obtained imaginary part of the dielectric function  $\varepsilon_2(\omega, \mathbf{q})$  depends on the frequency  $\omega$  and photon wave vector  $\mathbf{q}$ . For electromagnetic radiation up to the far UV spectral region (200 nm) the maximal transferred wave vector

$$2\mathbf{q} = \frac{4\pi}{\lambda} \sim 5 \cdot 10^{-3} \text{ \AA}^{-1} \quad (2.82)$$

is negligible compared to the reciprocal lattice vector. Thus, only phonons in the center ( $\Gamma$ ) of the Brillouin zone (BZ) can be excited.<sup>[150]</sup> Using perturbation theory within the limit  $\mathbf{q} \rightarrow 0$  and expanding all quantities depending on  $\mathbf{q}$  about  $\mathbf{q} = 0$ , the imaginary part of the dielectric function

$$\begin{aligned} \varepsilon_2(\omega, 0) = & \frac{e^2}{\mathbf{q}^2 \pi} \sum_v \int_{\text{BZ}} d\mathbf{k} f_0(E_{k,v}) \\ & \times [\delta(E_{\mathbf{k}+\mathbf{q},v} - E_{k,v} - \hbar\omega) - \delta(E_{\mathbf{k}-\mathbf{q},v} - E_{k,v} + \hbar\omega)] \\ & + \frac{e^2}{\pi m^2 \omega^2} \sum_{c,v} \int_{\text{BZ}} d\mathbf{k} [f_0(E_{k,v}) - f_0(E_{k,c})] \\ & \times |\mathbf{a}_0 \cdot \mathbf{p}_{ji}|^2 \delta(E_{k,c} - E_{k,v} - \hbar\omega) \end{aligned} \quad (2.83)$$

## 2 Theoretical background

is obtained.<sup>[149]</sup> The first term describes one-electron intraband excitations and the second term corresponds to interband optical absorption. Following Eq. 2.82,

$$\mathbf{q} = 0 \quad (2.84)$$

is valid for electromagnetic radiation until the far UV spectral region. In this case, the wave vector of the electron in the valence band  $\mathbf{k}'$  and the wave vector of the electron in the conduction band  $\mathbf{k}''$  are equal

$$\mathbf{k}' = \mathbf{k}'' . \quad (2.85)$$

Transitions described by Eq. 2.84 and 2.85 are called direct or vertical interband transitions.<sup>[144]</sup> At  $T = 0$  K, the Fermi distribution function  $f_0$  becomes a step function and for direct interband transitions

$$\varepsilon_2(\omega, 0) = \frac{e^2}{\pi m^2 \omega^2} \sum_{c,v} \int_{\text{BZ}} d\mathbf{k} |\mathbf{a}_0 \cdot \mathbf{p}_{cv}|^2 \delta(E_{\mathbf{k},c} - E_{\mathbf{k},v} - \hbar\omega) \quad (2.86)$$

is derived as expression for the imaginary part of the dielectric function. Here,  $m$  is the mass of an electron,  $e$  is the elementary charge,  $c$  denotes a state in the conduction band,  $v$  denotes a state in the valence band,  $E_{\mathbf{k}}$  is the energy for a given band and wave vector,  $\mathbf{a}_0$  is the unit polarization vector and  $\mathbf{p}_{cv}$  is the matrix element of the momentum operator or electric dipole transition matrix element, respectively.<sup>[144,151]</sup> The matrix element

$$\mathbf{p}_{cv} = \frac{1}{V} \int_{\text{cell}} \psi_c^* \mathbf{p} \psi_v d\mathbf{r} \quad (2.87)$$

is given by the volume of the unit cell  $V$ , the momentum operator  $\mathbf{p}$  and the wave functions  $\psi$  of the valence and conduction band.

The imaginary part of the dielectric function defined by direct interband transitions (see Eq. 2.86) consists of two fundamental parts given by the matrix element and the so-called joint density of states (JDOS). The JDOS measures the density of valence and conduction band states of equal energy difference. The matrix element weights the optical transitions, but the JDOS mainly determines the contribution of interband transitions to the optical properties of solids. The density of states (DOS) itself is characterized by states where the dispersion of a band is flat. Accordingly, critical points of the DOS at

$$\Delta_{\mathbf{k}} E_l(\mathbf{k}) = 0 \quad (2.88)$$

### 2.3 Quantum mechanical calculation of the refractive index

are given by the dispersion relation  $\Delta_k E_l(\mathbf{k})$  of a band  $l$ . These critical points are called van Hove singularities and occur at highly symmetric points in the BZ (denoted by capital Greek letters).<sup>[152]</sup> As a consequence, the JDOS shows maxima if the dispersion relation of the valence and conduction band are zero. Such points are called optical critical points and lead to a distinctive structure of the imaginary part of the dielectric function and in the optical absorption spectra. The relevance of the structure of the JDOS for the calculation of the imaginary part of the dielectric function demands precise knowledge of the energies of the valence and conduction band states. Consequently, the choice of the XC functional (see Sec. 2.2.2) is crucial for the calculation of the refractive index using DFT methods.

Using the calculated imaginary part of the dielectric function  $\varepsilon_2$ , the real part of the dielectric function  $\varepsilon_1$  can be obtained by the Kramers-Kronig dispersion relation given by Eq. 2.69. Finally, the dispersion of the refractive index  $n(\omega)$  can be calculated by applying Eq. 2.73 relating the complex dielectric function and the refractive index.

#### Polarizability approach

Lee and Colwell<sup>[153]</sup> developed the theory for the coupled perturbed Kohn-Sham (CPKS) calculation of the static polarisability  $\alpha$  with nonlocal functionals. By solving the CPKS equations for a given system, the polarisability can be calculated using DFT. In the following, orbitals  $\phi$  are denoted with indices, where  $i$  and  $j$  are unoccupied,  $a$  and  $b$  are occupied and  $p$  and  $q$  are any molecular orbitals. Here, the derivative of a molecular orbital with respect to a perturbation  $\lambda$  by an external electric field perturbation  $F^\lambda$

$$\frac{d\phi_p}{d\lambda} = U_{jp}^\lambda \phi_j \quad (2.89)$$

is given by the unknown tensor  $U^\lambda$  which can be calculated from the CPKS equations.

The dipole moment  $\mu^\lambda$  is obtained from the the first derivative of the energy with respect to the electric field perturbation  $F^\lambda$

$$\frac{dE}{d\lambda} = 2P_{ii}^\lambda = -\mu^\lambda \quad (2.90)$$

with

$$P_{ii}^\lambda = (i|x^\lambda|i) \quad (2.91)$$

## 2 Theoretical background

being a dipole moment matrix element given by a dipole moment integral. The second derivative of the energy with respect to the electric field perturbation  $F^\mu$

$$\frac{d^2 E}{d\lambda d\mu} = 4P_{pi}^\lambda U_{pi}^\mu = -\alpha_{\lambda\mu} \quad (2.92)$$

yields the polarizability  $\alpha_{\lambda\mu}$  with the tensor  $U_{pi}^\mu$ . The tensor of solutions  $U_{bj}^\lambda$  for perturbation  $\lambda$  is obtained by solving the CPKS equation

$$H_{aibj} U_{bj}^\lambda = -P_{ai}^\lambda \quad (2.93)$$

consisting of a perturbation specific matrix given by the dipole momentum matrix  $P_{ai}^\lambda$  and a perturbation independent matrix given by the Hessian matrix  $H_{aibj}$ . The Hessian matrix is given by

$$H_{aibj} = \delta_{ai,bj} (E_a - E_i) + 4(ai|bj) + 4 \left( \phi_a \phi_i \left| \frac{d^2 F_{XC}}{d\rho^2} \right| \phi_b \phi_j \right) \quad (2.94)$$

and depends on the orbital energies  $E$ , the two-electron repulsion integrals  $(ai|bj)$  and an integral depending on the second derivation of the exchange-correlation function  $F_{XC}$  with respect to the electron density  $\rho$ .<sup>[153]</sup> To calculate frequency-dependent polarizabilities, standard DFT is insufficient and current DFT (CDFT) along with the magnetic Hessian has to be used in addition to the electric Hessian given by Eq. 2.94.<sup>[154,155]</sup>

Analogous to the approach based on the dielectric function, the choice of the XC functional is crucial for the calculation of the polarizability and subsequently for the RI. But the number of implemented XC functionals in DFT codes using periodic boundary conditions with modules for the calculation of the polarizability (CASTEP, CRYSTAL) is limited.<sup>[156,157]</sup> Furthermore, these fully periodic calculations are computationally demanding. Therefore, it is convenient to calculate molecular polarizabilities instead of solid state polarizabilities.<sup>[32,158]</sup> This approach requires an appropriate fragmentation scheme to obtain molecular fragments from a solid state material. Using the molecular fragments, a series of molecular DFT calculations can be performed to obtain molecular polarizabilities. Finally, these molecular polarizabilities can be used to calculate the polarizability of the solid state material. In this work, such a fragmentation scheme was developed for MOFs (see Sec. 3.3).



Lorenz<sup>[159]</sup> (1869) and Lorentz<sup>[160]</sup> (1878) both derived independently a formula relating the refractive index and density of a substance.<sup>[161]</sup> The modern formulation of the Lorenz-Lorentz law

$$\frac{n^2 - 1}{n^2 + 2} = \frac{4\pi}{3} N\alpha \quad (2.95)$$

relates the RI  $n$  with the polarizability  $\alpha$  and number density  $N$  describing the number of molecules per unit volume. In the case of a crystalline material, the number density

$$N = \frac{1}{V} = \frac{\rho N_A}{M} \quad (2.96)$$

is equal to the reciprocal volume of the unit cell  $V$  and for amorphous materials it can be calculated from the density  $\rho$ , the Avogadro constant  $N_A$  and the molecular weight  $M$ . Using the static polarizability obtained by DFT calculations and the number density calculated from experimental data or theoretical studies, the Lorenz-Lorentz law yields the static RI of a material.

## 2.4 References

- [1] *Out of the crystal maze: Chapters from the history of solid-state physics*, (Eds.: L. Hoddeson, E. Braun, J. Teichmann, S. R. Weart), Oxford University Press, New York and Oxford, **1992**.
- [2] K. C. Kao, G. A. Hockham, *Proc. Inst. Electr. Eng.* **1966**, *113*, 1151–1158.
- [3] NobelPrize.org, The Nobel Prize in Physics 2009, **2009**, <https://www.nobelprize.org/prizes/physics/2009/summary> (visited on 04/23/2023).
- [4] P. Bettotti, *Advances in Optics* **2014**, *2014*, 1–24.
- [5] J. Wu, H. Zhang, W. Zhang, G. Jin, L. Cao, G. Barbastathis, *Light. Sci. Appl.* **2020**, *9*, 53.
- [6] E. K. Macdonald, M. P. Shaver, *Polym. Int.* **2015**, *64*, 6–14.
- [7] D. H. Kim, W. Jang, K. Choi, J. S. Choi, J. Pyun, J. Lim, K. Char, S. G. Im, *Sci. Adv.* **2020**, *6*, eabb5320.
- [8] C. Rodríguez, S. Günster, D. Ristau, W. Rudolph, *Opt. Express.* **2015**, *23*, 31594–31601.
- [9] R. Ferreira, P. S. André, L. D. Carlos, *Opt. Mater.* **2010**, *32*, 1397–1409.
- [10] R. Pardo, M. Zayat, D. Levy, *Chem. Soc. Rev.* **2011**, *40*, 672–687.
- [11] B. F. Hoskins, R. Robson, *J. Am. Chem. Soc.* **1989**, *111*, 5962–5964.

## 2 Theoretical background

- [12] L. E. Kreno, K. Leong, O. K. Farha, M. Allendorf, R. P. van Duyne, J. T. Hupp, *Chem. Rev.* **2012**, *112*, 1105–1125.
- [13] A. Dhakshinamoorthy, Z. Li, H. Garcia, *Chem. Soc. Rev.* **2018**, *47*, 8134–8172.
- [14] H. Li, K. Wang, Y. Sun, C. T. Lollar, J. Li, H.-C. Zhou, *Mater. Today* **2018**, *21*, 108–121.
- [15] T. N. Nguyen, F. M. Ebrahim, K. C. Stylianou, *Coord. Chem. Rev.* **2018**, *377*, 259–306.
- [16] W. Yin, C.-A. Tao, F. Wang, J. Huang, T. Qu, J. Wang, *Sci. China Mater.* **2018**, *61*, 391–400.
- [17] Y. Zheng, F.-Z. Sun, X. Han, J. Xu, X.-H. Bu, *Adv. Optical Mater.* **2020**, *8*, 2000110.
- [18] K.-T. Hsu, P. Thanasekaran, T.-W. Hsu, C.-H. Su, B.-C. Chang, Y.-H. Liu, C.-H. Hung, K.-L. Lu, *CrystEngComm* **2021**, *23*, 824–830.
- [19] H. Li, L. Zhang, H. He, Y. Yang, Y. Cui, G. Qian, *Sci. China Mater.* **2021**, *64*, 698–705.
- [20] Y. Bai, Y. Dou, L.-H. Xie, W. Rutledge, J.-R. Li, H.-C. Zhou, *Chem. Soc. Rev.* **2016**, *45*, 2327–2367.
- [21] J. H. Cavka, S. Jakobsen, U. Olsbye, N. Guillou, C. Lamberti, S. Bordiga, K. P. Lillerud, *J. Am. Chem. Soc.* **2008**, *130*, 13850–13851.
- [22] J. Winarta, B. Shan, S. M. Mcintyre, L. Ye, C. Wang, J. Liu, B. Mu, *Cryst. Growth Des.* **2020**, *20*, 1347–1362.
- [23] Y. J. Colón, R. Q. Snurr, *Chem. Soc. Rev.* **2014**, *43*, 5735–5749.
- [24] L.-M. Yang, E. Ganz, S. Svelle, M. Tilset, *J. Mater. Chem. C* **2014**, *2*, 7111–7125.
- [25] B. Ni, W. Sun, J. Kang, Y. Zhang, *J. Phys. Chem. C* **2020**, *124*, 11595–11608.
- [26] S. Grimme, *J. Comput. Chem.* **2006**, *27*, 1787–1799.
- [27] A. V. Krukau, O. A. Vydrov, A. F. Izmaylov, G. E. Scuseria, *J. Chem. Phys.* **2006**, *125*, 224106.
- [28] J. Paier, M. Marsman, K. Hummer, G. Kresse, I. C. Gerber, J. G. Ángyán, *J. Chem. Phys.* **2006**, *125*, 249901.
- [29] A. J. Garza, G. E. Scuseria, *J. Phys. Chem. Lett.* **2016**, *7*, 4165–4170.
- [30] M. Nishiwaki, H. Fujiwara, *Comput. Mater. Sci.* **2020**, *172*, 109315.
- [31] M. A. F. Afzal, C. Cheng, J. Hachmann, *J. Chem. Phys.* **2018**, *148*, 241712.
- [32] R. F. Ligorio, A. Krawczuk, L. H. R. Dos Santos, *J. Phys. Chem. A* **2020**, *124*, 10008–10018.

- [33] M. Ernst, L. H. R. Dos Santos, P. Macchi, *CrystEngComm* **2016**, *18*, 7339–7346.
- [34] S. R. Batten, N. R. Champness, X.-M. Chen, J. Garcia-Martinez, S. Kitagawa, L. Öhrström, M. O’Keeffe, M. Paik Suh, J. Reedijk, *Pure Appl. Chem.* **2013**, *85*, 710.
- [35] J. L. Rowsell, O. M. Yaghi, *Microporous Mesoporous Mat.* **2004**, *73*, 3–14.
- [36] J. Fonseca, T. Gong, L. Jiao, H.-L. Jiang, *J. Mater. Chem. A Mater.* **2021**, *9*, 10562–10611.
- [37] N. Ma, S. Horike, *Chem. Rev.* **2022**, *122*, 4163–4203.
- [38] O. M. Yaghi, G. Li, H. Li, *Nature* **1995**, *378*, 703–706.
- [39] W. Lu, Z. Wei, Z.-Y. Gu, T.-F. Liu, J. Park, J. Park, J. Tian, M. Zhang, Q. Zhang, T. Gentle, M. Bosch, H.-C. Zhou, *Chem. Soc. Rev.* **2014**, *43*, 5561–5593.
- [40] G. K. H. Shimizu, R. Vaidhyanathan, J. M. Taylor, *Chem. Soc. Rev.* **2009**, *38*, 1430–1449.
- [41] L. S. Xie, G. Skorupskii, M. Dincă, *Chem. Rev.* **2020**, *120*, 8536–8580.
- [42] H. Li, M. Eddaoudi, M. O’Keeffe, O. M. Yaghi, *Nature* **1999**, *402*, 276–279.
- [43] F. Millange, C. Serre, G. Férey, *Chem. Commun.* **2002**, 822–823.
- [44] F. Millange, N. Guillou, R. I. Walton, J.-M. Grenèche, I. Margiolaki, G. Férey, *Chem. Commun.* **2008**, 4732–4734.
- [45] C. Volkringer, T. Loiseau, N. Guillou, G. Férey, E. Elkaïm, A. Vimont, *Dalton. Trans.* **2009**, 2241–2249.
- [46] J. P. Mowat, S. R. Miller, A. M. Slawin, V. R. Seymour, S. E. Ashbrook, P. A. Wright, *Microporous Mesoporous Mat.* **2011**, *142*, 322–333.
- [47] S. Jakobsen, D. Gianolio, D. S. Wragg, M. H. Nilsen, H. Emerich, S. Bordiga, C. Lamberti, U. Olsbye, M. Tilset, K. P. Lillerud, *Phys. Rev. B* **2012**, *86*, 263.
- [48] C. Falaise, C. Volkringer, J.-F. Vigier, N. Henry, A. Beaurain, T. Loiseau, *Chemistry* **2013**, *19*, 5324–5331.
- [49] C. Falaise, J.-S. Charles, C. Volkringer, T. Loiseau, *Inorg. Chem.* **2015**, *54*, 2235–2242.
- [50] M. Lammert, M. T. Wharmby, S. Smolders, B. Bueken, A. Lieb, K. A. Lomachenko, D. de Vos, N. Stock, *Chem. Commun.* **2015**, *51*, 12578–12581.
- [51] K. Barthelet, J. Marrot, D. Riou, G. Férey, *Angew. Chem. Int. Ed. Engl.* **2002**, *41*, 281.

## 2 Theoretical background

- [52] T. Loiseau, C. Serre, C. Huguenard, G. Fink, F. Taulelle, M. Henry, T. Bataille, G. Férey, *Chemistry* **2004**, *10*, 1373–1382.
- [53] E. V. Anokhina, M. Vougo-Zanda, X. Wang, A. J. Jacobson, *J. Am. Chem. Soc.* **2005**, *127*, 15000–15001.
- [54] V. Guillerm, F. Ragon, M. Dan-Hardi, T. Devic, M. Vishnuvarthan, B. Campo, A. Vimont, G. Clet, Q. Yang, G. Maurin, G. Férey, A. Vittadini, S. Gross, C. Serre, *Angew. Chem.* **2012**, *124*, 9401–9405.
- [55] S. Yuan, J.-S. Qin, C. T. Lollar, H.-C. Zhou, *ACS Cent. Sci.* **2018**, *4*, 440–450.
- [56] D. Zou, D. Liu, *Mater. Today Chem.* **2019**, *12*, 139–165.
- [57] M. Eddaoudi, J. Kim, N. Rosi, D. Vodak, J. Wachter, M. O’Keeffe, O. M. Yaghi, *Science* **2002**, *295*, 469–472.
- [58] S. T. Meek, J. J. Perry, S. L. Teich-McGoldrick, J. A. Greathouse, M. D. Allendorf, *Cryst. Growth Des.* **2011**, *11*, 4309–4312.
- [59] J.-S. Qin, S. Yuan, Q. Wang, A. Alsalmé, H.-C. Zhou, *J. Mater. Chem. A Mater.* **2017**, *5*, 4280–4291.
- [60] S. Abednatanzi, P. Gohari Derakhshandeh, H. Depauw, F.-X. Coudert, H. Vrielinck, P. van der Voort, K. Leus, *Chem. Soc. Rev.* **2019**, *48*, 2535–2565.
- [61] P. Z. Moghadam, A. Li, X.-W. Liu, R. Bueno-Perez, S.-D. Wang, S. B. Wiggin, P. A. Wood, D. Fairen-Jimenez, *Chem. Sci.* **2020**, *11*, 8373–8387.
- [62] S. M. Moosavi, A. Nandy, K. M. Jablonka, D. Ongari, J. P. Janet, P. G. Boyd, Y. Lee, B. Smit, H. J. Kulik, *Nat. Commun.* **2020**, *11*, 4068.
- [63] M. O’Keeffe, M. A. Peskov, S. J. Ramsden, O. M. Yaghi, *Acc. Chem. Res.* **2008**, *41*, 1782–1789.
- [64] O. Ioannidou, A. Zabaniotou, *Renew. Sust. Energ. Rev.* **2007**, *11*, 1966–2005.
- [65] S. S. Kaye, A. Dailly, O. M. Yaghi, J. R. Long, *J. Am. Chem. Soc.* **2007**, *129*, 14176–14177.
- [66] A. Schaate, P. Roy, A. Godt, J. Lippke, F. Waltz, M. Wiebcke, P. Behrens, *Chemistry* **2011**, *17*, 6643–6651.
- [67] Le Han, J. Zhang, Y. Mao, W. Zhou, W. Xu, Y. Sun, *Ind. Eng. Chem. Res.* **2019**, *58*, 15489–15496.

- [68] I. M. Hönicke, I. Senkovska, V. Bon, I. A. Baburin, N. Bönisch, S. Raschke, J. D. Evans, S. Kaskel, *Angew. Chem. Int. Ed. Engl.* **2018**, *57*, 13780–13783.
- [69] A. Dhakshinamoorthy, Z. Li, H. Garcia, *Chem. Soc. Rev.* **2018**, *47*, 8134–8172.
- [70] H. Li, K. Wang, Y. Sun, C. T. Lollar, J. Li, H.-C. Zhou, *Mater. Today* **2018**, *21*, 108–121.
- [71] Y. Cheng, S. J. Datta, S. Zhou, J. Jia, O. Shekhah, M. Eddaoudi, *Chem. Soc. Rev.* **2022**, *51*, 8300–8350.
- [72] G. Cai, P. Yan, L. Zhang, H.-C. Zhou, H.-L. Jiang, *Chem. Rev.* **2021**, *121*, 12278–12326.
- [73] L. E. Kreno, K. Leong, O. K. Farha, M. Allendorf, R. P. van Duyne, J. T. Hupp, *Chem. Rev.* **2012**, *112*, 1105–1125.
- [74] M.-X. Wu, Y.-W. Yang, *Adv. Mater.* **2017**, *29*, 1606134.
- [75] Water Harvesting Inc., <https://wahainc.com/>.
- [76] N. Hanikel, M. S. Prévot, F. Fathieh, E. A. Kapustin, H. Lyu, H. Wang, N. J. Diercks, T. G. Glover, O. M. Yaghi, *ACS Cent. Sci.* **2019**, *5*, 1699–1706.
- [77] J. Arnó, O. K. Farha, W. Morris, P. W. Siu, G. M. Tom, M. H. Weston, P. E. Fuller in 22nd International Conference on Ion Implantation Technology (IIT), **2018**, pp. 227–230.
- [78] C. Zhu, R. E. Gerald, J. Huang, *IEEE Sensors J.* **2021**, *21*, 19647–19661.
- [79] E. Redel, Z. Wang, S. Walheim, J. Liu, H. Gliemann, C. Wöll, *Appl. Phys. Lett.* **2013**, *103*, 091903.
- [80] Y. Huang, C.-A. Tao, R. Chen, L. Sheng, J. Wang, *Nanomaterials* **2018**, *8*, 676.
- [81] N. C. Keppler, K. D. J. Hindricks, P. Behrens, *RSC Adv.* **2022**, *12*, 5807–5815.
- [82] S. Øien, D. Wragg, H. Reinsch, S. Svelle, S. Bordiga, C. Lamberti, K. P. Lillerud, *Cryst. Growth Des.* **2014**, *14*, 5370–5372.
- [83] L. Valenzano, B. Civalleri, S. Chavan, S. Bordiga, M. H. Nilsen, S. Jakobsen, K. P. Lillerud, C. Lamberti, *Chem. Mater.* **2011**, *23*, 1700–1718.
- [84] S. Biswas, J. Zhang, Z. Li, Y.-Y. Liu, M. Grzywa, L. Sun, D. Volkmer, P. van der Voort, *Dalton. Trans.* **2013**, *42*, 4730–4737.
- [85] Z. Chen, S. L. Hanna, L. R. Redfern, D. Alezi, T. Islamoglu, O. K. Farha, *Coord. Chem. Rev.* **2019**, *386*, 32–49.

## 2 Theoretical background

- [86] F. Vermoortele, M. Vandichel, B. van de Voorde, R. Ameloot, M. Waroquier, V. van Speybroeck, D. E. de Vos, *Angew. Chem. Int. Ed. Engl.* **2012**, *51*, 4887–4890.
- [87] S. Biswas, P. van der Voort, *Eur. J. Inorg. Chem.* **2013**, *2013*, 2154–2160.
- [88] Z. Hu, Y. Peng, Z. Kang, Y. Qian, D. Zhao, *Inorg. Chem.* **2015**, *54*, 4862–4868.
- [89] S. J. Garibay, S. M. Cohen, *Chem. Commun.* **2010**, *46*, 7700–7702.
- [90] M. Kandiah, M. H. Nilsen, S. Usseglio, S. Jakobsen, U. Olsbye, M. Tilset, C. Larabi, E. A. Quadrelli, F. Bonino, K. P. Lillerud, *Chem. Mater.* **2010**, *22*, 6632–6640.
- [91] G. Wißmann, A. Schaate, S. Lilienthal, I. Bremer, A. M. Schneider, P. Behrens, *Microporous Mesoporous Mat.* **2012**, *152*, 64–70.
- [92] H. Furukawa, F. Gándara, Y.-B. Zhang, J. Jiang, W. L. Queen, M. R. Hudson, O. M. Yaghi, *J. Am. Chem. Soc.* **2014**, *136*, 4369–4381.
- [93] G. Zahn, H. A. Schulze, J. Lippke, S. König, U. Sazama, M. Fröba, P. Behrens, *Microporous Mesoporous Mat.* **2015**, *203*, 186–194.
- [94] Z. Yan, Y. Gong, B. Chen, X. Wu, Q. Liu, L. Cui, S. Xiong, S. Peng, *Sep. Purif. Technol.* **2020**, *239*, 116514.
- [95] W. Xu, O. M. Yaghi, *ACS Cent. Sci.* **2020**, *6*, 1348–1354.
- [96] M. Schulz, N. Marquardt, M. Schäfer, D. P. Warwas, S. Zailskas, A. Schaate, *Chemistry* **2019**, *25*, 13598–13608.
- [97] W. Liang, R. Babarao, D. M. D’Alessandro, *Inorg. Chem.* **2013**, *52*, 12878–12880.
- [98] J. Jacobsen, L. Wegner, H. Reinsch, N. Stock, *Dalton. Trans.* **2020**, *49*, 11396–11402.
- [99] K. S. Park, Z. Ni, A. P. Côté, J. Y. Choi, R. Huang, F. J. Uribe-Romo, H. K. Chae, M. O’Keeffe, O. M. Yaghi, *Proc. Natl. Acad. Sci. USA* **2006**, *103*, 10186–10191.
- [100] S. Lee, D. Nam, D. C. Yang, W. Choe, *Small* **2023**, *19*, e2300036.
- [101] X.-C. Huang, Y.-Y. Lin, J.-P. Zhang, X.-M. Chen, *Angew. Chem. Int. Ed. Engl.* **2006**, *45*, 1557–1559.
- [102] L. Pauling, *Z. Kristallogr.* **1930**, *74*, 213–225.
- [103] H. Shen, H. Zhao, E. Benassi, L. Chou, H. Song, *CrystEngComm* **2023**, *25*, 3308–3316.
- [104] R. Banerjee, A. Phan, B. Wang, C. Knobler, H. Furukawa, M. O’Keeffe, O. M. Yaghi, *Science* **2008**, *319*, 939–943.

- [105] Y.-Q. Tian, S.-Y. Yao, D. Gu, K.-H. Cui, D.-W. Guo, G. Zhang, Z.-X. Chen, D.-Y. Zhao, *Chemistry* **2010**, *16*, 1137–1141.
- [106] S. Horike, K. Kadota, T. Itakura, M. Inukai, S. Kitagawa, *Dalton Trans.* **2015**, *44*, 15107–15110.
- [107] K. Kadota, E. Sivaniah, S. Bureekaew, S. Kitagawa, S. Horike, *Inorg. Chem.* **2017**, *56*, 8744–8747.
- [108] J. López-Cabrelles, J. Romero, G. Abellán, M. Giménez-Marqués, M. Palomino, S. Valencia, F. Rey, G. Mínguez Espallargas, *J. Am. Chem. Soc.* **2019**, *141*, 7173–7180.
- [109] O. Karagiari, M. B. Lalonde, W. Bury, A. A. Sarjeant, O. K. Farha, J. T. Hupp, *J. Am. Chem. Soc.* **2012**, *134*, 18790–18796.
- [110] M. E. Schweinefuss, S. Springer, I. A. Baburin, T. Hikov, K. Huber, S. Leoni, M. Wiebcke, *Dalton Trans.* **2014**, *43*, 3528–3536.
- [111] W. Morris, C. J. Doonan, H. Furukawa, R. Banerjee, O. M. Yaghi, *J. Am. Chem. Soc.* **2008**, *130*, 12626–12627.
- [112] Y. Ban, Y. Li, Y. Peng, H. Jin, W. Jiao, X. Liu, W. Yang, *Chemistry* **2014**, *20*, 11402–11409.
- [113] S. S. Mondal, M. Hovestadt, S. Dey, C. Paula, S. Glomb, A. Kelling, U. Schilde, C. Janiak, M. Hartmann, H.-J. Holdt, *CrystEngComm* **2017**, *19*, 5882–5891.
- [114] B. Chen, Z. Yang, Y. Zhu, Y. Xia, *J. Mater. Chem. A Mater.* **2014**, *2*, 16811–16831.
- [115] G. Lu, J. T. Hupp, *J. Am. Chem. Soc.* **2010**, *132*, 7832–7833.
- [116] F. M. Hinterholzinger, A. Ranft, J. M. Feckl, B. Rühle, T. Bein, B. V. Lotsch, *J. Mater. Chem.* **2012**, *22*, 10356.
- [117] R. G. Parr, *Density-Functional Theory of Atoms and Molecules*, Oxford University Press, Cary, **1989**.
- [118] A. Szabo, N. S. Ostlund, *Modern quantum chemistry: Introduction to advanced electronic structure theory*, 1st publ., unabr., unaltered republ. of the 1st ed., New York 1989, Dover Publications, Mineola, New York, **1996**.
- [119] W. Koch, *A Chemist's Guide to Density Functional Theory*, 2nd ed., Wiley-VCH, Weinheim, **2001**.
- [120] P. Hohenberg, W. Kohn, *Phys. Rev.* **1964**, *136*, B864–B871.

## 2 Theoretical background

- [121] P.-O. Löwdin, *Int. J. Quantum Chem.* **1985**, *28*, 19–37.
- [122] W. Kohn, L. J. Sham, *Phys. Rev.* **1965**, *140*, A1133–A1138.
- [123] R. O. Jones, O. Gunnarsson, *Rev. Mod. Phys.* **1989**, *61*, 689–746.
- [124] NobelPrize.org, The Nobel Prize in Chemistry 1998, **1998**, <https://www.nobelprize.org/prizes/chemistry/1998/summary/> (visited on 07/01/2023).
- [125] J. P. Perdew, K. Schmidt in AIP Conference Proceedings, AIP, **2001**, pp. 1–20.
- [126] J. P. Perdew, A. Ruzsinszky, J. Tao, V. N. Staroverov, G. E. Scuseria, G. I. Csonka, *J. Chem. Phys.* **2005**, *123*, 62201.
- [127] J. P. Perdew, Kieron, M. Ernzerhof, *Phys. Rev. Lett.* **1996**, *77*, 3865–3868.
- [128] N. Mardirossian, M. Head-Gordon, *Mol. Phys.* **2017**, *115*, 2315–2372.
- [129] A. D. Becke, *J. Chem. Phys.* **1993**, *98*, 5648–5652.
- [130] C. Adamo, V. Barone, *J. Chem. Phys.* **1999**, *110*, 6158–6170.
- [131] J. Heyd, G. E. Scuseria, M. Ernzerhof, *J. Chem. Phys.* **2003**, *118*, 8207–8215.
- [132] S. Kozuch, J. M. L. Martin, *J. Comput. Chem.* **2013**, *34*, 2327–2344.
- [133] S. Grimme, *J. Comput. Chem.* **2004**, *25*, 1463–1473.
- [134] S. Grimme, J. Antony, S. Ehrlich, H. Krieg, *J. Chem. Phys.* **2010**, *132*, 154104.
- [135] E. Caldeweyher, S. Ehlert, A. Hansen, H. Neugebauer, S. Spicher, C. Bannwarth, S. Grimme, *J. Chem. Phys.* **2019**, *150*, 154122.
- [136] A. Tkatchenko, M. Scheffler, *Phys. Rev. Lett.* **2009**, *102*, 073005.
- [137] J. C. Slater, *Phys. Rev.* **1930**, *36*, 57–64.
- [138] S. F. Boys, *Proc. R. Soc. Lond. A* **1950**, *200*, 542–554.
- [139] F. Jensen, *Introduction to computational chemistry*, 3rd ed., Wiley, Chichester, West Sussex, Hoboken, NJ, and Oxford, **2017**.
- [140] F. Weigend, R. Ahlrichs, *Phys. Chem. Chem. Phys.* **2005**, *7*, 3297–3305.
- [141] D. S. Sholl, J. A. Steckel, *Density functional theory: A practical introduction*, Wiley, Hoboken, N.J., **2009**.
- [142] M. Fox, *Optical properties of solids*, Reprinted., Oxford Univ. Press, Oxford, **2008**.



- [143] S. Adachi, *Optical Properties of Crystalline and Amorphous Semiconductors: Materials and Fundamental Principles*, Springer US, New York, **1999**.
- [144] F. Wooten, *Optical Properties of Solids*, Elsevier Science, Burlington, **1972**.
- [145] R. de L. Kronig, *J. Opt. Soc. Am.* **1926**, *12*, 547.
- [146] J. H. Lambert, *Photometria Sive De Mensura Et Gradibus Luminis, Colorum Et Umbrae: Photometry, or, On the measure and gradations of light intensity, colors, and shade*, Klett, Augsburg, **1760**.
- [147] S. Singh, *Phys. Scr.* **2002**, *65*, 167–180.
- [148] *The Properties of Optical Glass*, (Ed.: H. Bach), Springer, Berlin and New York, **1998**.
- [149] H. Ehrenreich, M. H. Cohen, *Phys. Rev.* **1959**, *115*, 786–790.
- [150] H. Ibach, H. Lüth, *Festkörperphysik*, Springer Berlin Heidelberg, Berlin, Heidelberg, **2009**.
- [151] M. Dressel, G. Grüner, *Electrodynamics of solids: Optical properties of electrons in matter*, Cambridge University Press, Cambridge, New York, and Melbourne, **2002**.
- [152] L. van Hove, *Phys. Rev.* **1953**, *89*, 1189–1193.
- [153] A. M. Lee, S. M. Colwell, *J. Chem. Phys.* **1994**, *101*, 9704–9709.
- [154] S. M. Colwell, N. C. Handy, Lee, *Phys. Rev. A* **1996**, *53*, 1316–1322.
- [155] A. G. Ioannou, S. M. Colwell, R. D. Amos, *Chem. Phys. Lett.* **1997**, *278*, 278–284.
- [156] S. J. Clark, M. D. Segall, C. J. Pickard, P. J. Hasnip, M. I. J. Probert, K. Refson, M. C. Payne, *Z. Kristallogr.* **2005**, *220*, 567–570.
- [157] R. Dovesi, A. Erba, R. Orlando, C. M. Zicovich–Wilson, B. Civalleri, L. Maschio, M. Rérat, S. Casassa, J. Baima, S. Salustro, B. Kirtman, *WIREs Comput. Mol. Sci.* **2018**, *8*, e1360.
- [158] A. Jabłuszewska, A. Krawczuk, L. H. R. Dos Santos, P. Macchi, *ChemPhysChem* **2020**, *21*, 2155–2165.
- [159] L. Lorenz, *Ann. Phys. Chem.* **1880**, *247*, 70–103.
- [160] H. A. Lorentz, *Ann. Phys. Chem.* **1880**, *245*, 641–665.
- [161] H. Kragh, *Substantia* **2018**, *2*, 7–18.



## 3 Results and discussion

In the following sections the simulation approaches developed in this work and the results of the corresponding studies are presented. The first study introduces a simulation approach aiming at the precise calculation of the RI of MOFs using periodic boundary conditions (PBC). This simulation approach is applied and validated using UiO-66 and derivatives. Furthermore, the optical properties of these compounds are discussed. Subsequently, a second study is presented in which the PBC-based simulation approach is utilized to calculate the optical properties of UiO-66 and its halogenated analogues with a focus on high RI values and transparency in the visible spectral region. Finally, a third publication is presented dealing with the development of a simulation approach that overcomes the high computational effort of the PBC-based simulation approach. Therefore, a fragmentation scheme for MOFs is introduced allowing the fragment-based, efficient calculation of the RI of MOFs.

### 3.1 Tuning the optical properties of the metal-organic framework UiO-66 via ligand functionalization

#### Preface

This work was published as full paper in the journal “Physical chemistry chemical physics: PCCP” of the Royal Society of Chemistry. The detailed investigation of the electronic structure of MOFs is presented to gain a better understanding of the refractive index of MOFs as fundamental optical property. The UiO-66 MOF is a prominent Zr-based MOF with high chemical and thermal stability. Therefore it was considered as a prototype for the development of novel materials. It is well-known, that the electronic and optical properties of UiO-66 can be altered by introducing functional groups to the *bdc* linker. Apart from the following publication, there were only qualitative calculations of the RI of UiO-66 and its derivatives present in literature. These studies are based on GGA level DFT calculations of the electronic structure and optical properties and employ small basis sets. To reproduce correct band gap values, a scissors operator was applied to those calculations breaking the sum rule and thus leading to overestimated RI values.

In this work, a simulation approach was developed to precisely calculate the RI of MOFs using DFT. The correct description of the electronic structure and thus the optical properties of MOFs by this approach was validated with UV-Vis DRS. To ensure reliable results, carefully converged

### 3 Results and discussion

plane-wave basis sets and fully relaxed models were used allowing a precise description of crystal structures of the studied MOFs. Therefore, a XC functional benchmark at GGA level was performed for UiO-66 and its analogues to determine suitable XC functionals for the energy minimization of the prepared models. Subsequently, the electronic structures and the optical properties were calculated at hGGA level using the HSE06 functional. The effect on the optical properties due to the introduction of electron donating (“push”) and withdrawing (“pull”) functional groups to the *bdc* linker was studied with UiO-66 and its amino (UiO-66-NH<sub>2</sub>) and nitro (UiO-66-NO<sub>2</sub>) derivatives, respectively.

In addition, a novel bifunctional UiO-66 derivative was presented, synthesized, and fully characterized. The UiO-66-(NH<sub>2</sub>,NO<sub>2</sub>) MOF introduces “push” and “pull” groups into the framework within one linker. This allows a further tuning of the RI of the parent UiO-66 MOF. Finally, this concept of a bifunctional push-pull linker was extended and used to design three additional novel UiO-66 analogues, that were characterized with DFT methods. As a result, a series of UiO-66-type MOFs was obtained possessing a broad range of RI values. This demonstrates the capabilities of MOFs as materials for optical applications and highlights the design of MOFs with tailored optical properties via the functionalization of linker molecules.

The author of this thesis developed the simulation approach presented in this work, performed all calculations, evaluated the experimental UV-Vis DRS data provided by Adrian Hannebauer and wrote the majority of the manuscript. Adrian Hannebauer synthesized all MOF samples and analyzed them with powder X-ray diffraction (PXRD), scanning electron microscopy (SEM), thermogravimetric analysis (TGA), UV-Vis DRS and physisorption measurements. Additionally, he wrote the experimental part of the manuscript. The linker used to prepare the novel UiO-66-(NH<sub>2</sub>,NO<sub>2</sub>) MOF was synthesized by Jan L. Budde. The novel MOF was also synthesised for the first time by Jan L. Budde. Dr. Andreas Schaate supervised the work concerning the novel UiO-66-(NH<sub>2</sub>,NO<sub>2</sub>) MOF and wrote the corresponding experimental part of this work. Prof. Dr. Peter Behrens and Dr. Andreas M. Schneider guided this study and edited the initial manuscript. Finally, the scientific computing team of the Leibniz University of Hannover supported the author of this thesis by helping to compile the CASTEP code and set up the required system environment at the Leibniz University IT Services (LUIS) high-performance computing (HPC) cluster system.

The article is reproduced with permission of the Royal Society of Chemistry.

### 3.1 Tuning the optical properties of the metal-organic framework UiO-66 via ligand functionalization

## Tuning the optical properties of the metal-organic framework UiO-66 via ligand functionalization

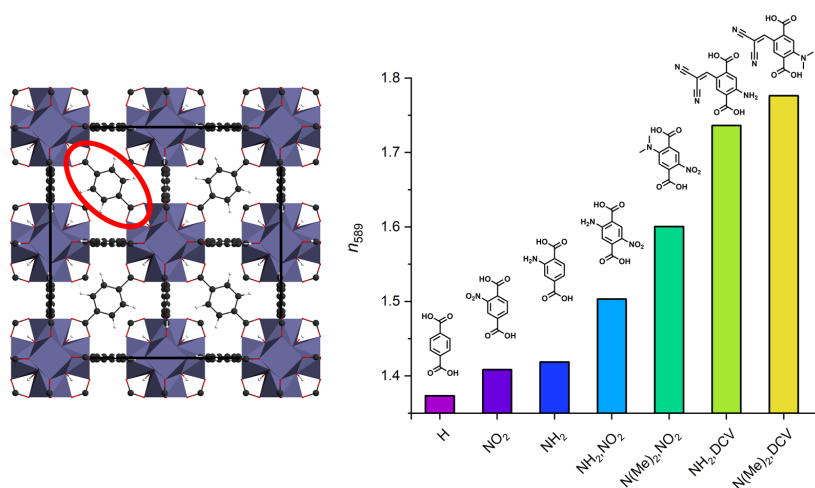
M. Treger, A. Hannebauer, A. Schaate, J. L. Budde, P. Behrens, A. M. Schneider, *Phys. Chem. Chem. Phys.* **2023**, *25*, 6333–6341.

DOI: 10.1039/d2cp03746g

Electronic supplementary information is available at <https://doi.org/10.1039/d2cp03746g>.

### Graphical abstract

Metal-organic frameworks (MOFs) possess a modular construction. By varying the functional groups on the linker unit, the refractive index  $n$  of UiO-66 MOFs can be tuned over a wide range, as high-level band structure calculations show.



PCCP



PAPER

View Article Online  
View Journal | View IssueCite this: *Phys. Chem. Chem. Phys.*,  
2023, 25, 6333

## Tuning the optical properties of the metal–organic framework UiO-66 via ligand functionalization†

Marvin Treger,<sup>ab</sup> Adrian Hannebauer,<sup>a</sup> Andreas Schaate,<sup>ab</sup> Jan L. Budde,<sup>a</sup>  
Peter Behrens<sup>ab</sup> and Andreas M. Schneider<sup>\*ab</sup>

Metal–organic frameworks (MOFs) are a promising class of materials for optical applications, especially due to their modular design which allows fine-tuning of the relevant properties. The present theoretical study examines the Zr-based UiO-66-MOF and derivatives of it with respect to their optical properties. Starting from the well-known monofunctional amino- and nitro-functionalized UiO-66 derivatives, we introduce novel UiO-66-type MOFs containing bifunctional push–pull 1,4-benzenedicarboxylate (*bdc*) linkers. The successful synthesis of such a novel UiO-66 derivative is also reported. It was carried out using a *para*-nitroaniline (PNA)-based *bdc*-analogue linker. Applying density functional theory (DFT), suitable models for all UiO-66-MOF analogues were generated by assessing different exchange–correlation functionals. Afterwards, HSE06 hybrid functional calculations were performed to obtain the electronic structures and optical properties. The detailed HSE06 electronic structure calculations were validated with UV-Vis measurements to ensure reliable results. Finally, the refractive index dispersion of the seven UiO-66-type materials is compared, showing the possibility to tailor the optical properties by the use of functionalized linker molecules. Specifically, the refractive index can be varied over a wide range from 1.37 to 1.78.

Received 14th August 2022,  
Accepted 2nd February 2023

DOI: 10.1039/d2cp03746g

rsc.li/pccp

### Introduction

Metal–organic frameworks (MOFs) are an important class of porous organic–inorganic hybrid materials built up by metal ions or metal-oxide clusters as inorganic building units (IBUs) connected by organic ligands acting as linkers.<sup>1,2</sup> Based on the intrinsic porosity of the frameworks, MOFs have been discussed intensively with regard to classical applications of such materials, like catalysis, gas separation, gas storage, or gas sensing.<sup>3–5</sup>

More recently, the use of MOFs for optical applications has gathered increasing attention.<sup>6–10</sup> Due to their modular design, the electronic and optical properties of MOFs can be tailored by making use of the possibilities to employ different metal centers, different linkers, and to exploit the pore space for storing guest molecules.<sup>11–13</sup> This versatility and adaptability enables the development of new materials for optical components with precisely adjusted properties. Compared to classical optical materials like

glasses, MOFs furthermore offer the advantage of low temperature preparation routes, thus simplifying and cheapening the production processes of optical systems. Further work is needed in order to prepare MOF entities with optical quality, *e.g.* as highly transparent thin films, generated, *e.g.*, *via* layer-by-layer synthesis, direct crystallisation or spin-coating techniques.<sup>7,13–15</sup>

Zr-based frameworks represent a promising family of MOFs, consisting of numerous different compounds, most of which feature exceptional chemical and thermal stability, promoting Zr-based MOFs for materials development.<sup>16</sup> In this study we focus on the Zr-based MOF UiO-66 and its functionalized derivatives. The UiO-66 framework is built up from zirconium-oxo-hydroxo clusters [Zr<sub>6</sub>O<sub>4</sub>(OH)<sub>4</sub>] which are 12-fold coordinated by 1,4-benzenedicarboxylate (*bdc*) forming an expanded cubic closed-packed structure.<sup>17</sup> The use of amino- or nitro-functionalized *bdc* linkers results in the well-established UiO-66-NH<sub>2</sub> and UiO-66-NO<sub>2</sub> MOFs sharing the UiO-66 topology and exhibiting a high stability as well.<sup>18,19</sup> While the framework topology remains, these derivatives show differences in the porosity and chemical nature of the pores, as well as different electronic, spectral and optical properties.<sup>20–22</sup>

This study aims to gain a better understanding of a basic optical property of MOFs, namely the refractive index. The refractive index is of importance in many optical applications, but in the case of MOFs has been somewhat overlooked. Only in the last few years, the

<sup>a</sup> Institute of Inorganic Chemistry, Leibniz University Hannover, 30167, Hannover, Germany. E-mail: andreas.schneider@acb.uni-hannover.de

<sup>b</sup> Cluster of Excellence PhoenixD (Photonics, Optics, and Engineering – Innovation Across Disciplines), Hannover, Germany

† Electronic supplementary information (ESI) available: Synthesis procedures, argon sorption isotherm, TG analysis, NMR analysis, UV-Vis spectra, details of DFT calculations. See DOI: <https://doi.org/10.1039/d2cp03746g>

### 3.1 Tuning the optical properties of the metal-organic framework UiO-66 via ligand functionalization

View Article Online

Paper

PCCP

interest in the evaluation of the refractive index of MOFs has increased somewhat.<sup>7,13</sup> Changes in refractive index have been measured, mostly *via* ellipsometry on thin films (not all of which were of optical quality), often with the idea to use the measured variations as sensor signals.<sup>15,23–29</sup> In a similar vein, variations in signal intensities on waveguides covered with MOFs were measured.<sup>30,31</sup> These experiments thus used the empty pore space of the MOFs.

Here, we focus instead on the linker chemistry to test its influence on the refractive index of the frameworks themselves. Especially, we want to determine the range of accessible refractive indices which can be achieved by the addition of functional groups to a “standard” MOF linker, namely terephthalate. For this purpose, we calculate the electronic properties of UiO-66 derivatives containing linkers with additional functional groups which give the linker molecules push–pull properties. These linker molecules contain “push” groups like amino (NH<sub>2</sub>) or dimethylamino (N(Me)<sub>2</sub>) and “pull” groups like nitro (NO<sub>2</sub>) or dicyanovinyl (DCV) and are shown in Fig. 1d–f. Results obtained on UiO-66-MOF structures with these linkers will be compared to those gained on the simpler congeners UiO-66, UiO-66-NH<sub>2</sub> and UiO-66-NO<sub>2</sub>, containing the linkers depicted in Fig. 1a–c. The introduction of push–pull-linkers allows advanced band gap modulation and leads to materials with tailored optical properties. The electronic and optical properties of UiO-66 MOFs containing the linker molecules depicted in Fig. 1 are characterized by applying density functional theory (DFT). Assessing different exchange–correlation functionals and dispersion corrections within the (meta) generalized gradient approximation (GGA, mGGA) we obtain adequate structural descriptions of the UiO-66 analogues. Subsequently, we use the range-separated hybrid functional HSE06 to determine both, the electronic structure and optical properties of UiO-66 and its derivatives with high accuracy.<sup>32–35</sup> To the best of our knowledge, this is the first study of MOFs examining the electronic and optical properties relying completely on hybrid DFT calculations. To gain full benefit of this high level of theory calculations and reliable results, we use carefully converged plane-wave basis sets and fully relaxed models with a precise representation of the studied structures

eliminating influences of the basis set size and variations of the cell volume on the calculated optical properties.

Furthermore, in the experimental part of the work, we report the synthesis of a novel bifunctional UiO-66 derivative featuring a terephthalate-based *para*-nitroaniline linker (*pnadc*: 2-amino-5-nitrobenzene-1,4-dicarboxylate) introducing amino- and nitro-groups into the framework within one linker. We fully characterize this novel MOF which is only the second framework containing this special linker.<sup>36</sup>

With the novel UiO-66-(NH<sub>2</sub>,NO<sub>2</sub>), UiO-66-MOFs with the linkers depicted in Fig. 1a–d are available for experimental investigations. We have determined the band gaps of these substances experimentally from their UV-Vis spectra and compare the obtained values to the calculated ones.

With a better understanding of how the various modular components – metal oxide clusters, linkers, guest molecules – influence the refractive index, MOFs can qualify as optical materials beyond the application of guest-selective coatings. They can be employed as coatings for mirrors and lenses, or as optical media in more complex devices like waveguiding elements, optical filters or in Fabry–Pérot devices.

## Methods

### Experimental details

UiO-66 was synthesized according to the synthetic route of Shearer *et al.*<sup>37</sup> All three UiO-66 derivatives were synthesized in a 100 mL Pyrex glass vessel by dissolving specific amounts of a Zr(IV)-source, water, modulator and linker successively in DMF. The exact values are given in ESI,† Section S1. The glass vessels were sealed and heated at 120 °C for 24 h (150 °C and 12 h for UiO-66-(NH<sub>2</sub>,NO<sub>2</sub>)). After cooling to room temperature, the precipitate was separated *via* centrifugation, washed with DMF and acetone and dried under vacuum. To further purify the material, each powder was Soxhlet-extracted with acetone for 24 h and activated at 150 °C under vacuum.

Powder X-Ray diffraction (PXRD) was carried out in transmission mode using a Stoe Stadi-P diffractometer operated with Ge (111)-monochromatized CuK $\alpha_1$  radiation ( $\lambda = 1.54060$  Å). A Mythen 1K detector was used and the diffractograms were recorded from 5 to 50° 2 $\theta$ . UV-Vis diffuse reflectance spectroscopy (UV-Vis DRS) was performed on the MOF powders using a Praying Mantis device on a Cary 4000 from Agilent Technologies. For this purpose, the MOF powder was mortared with BaSO<sub>4</sub> to gain better quality measurements. For further characterization, MOF samples were digested according to the procedure of Chu *et al.* and transferred to liquid-state <sup>1</sup>H-NMR-spectroscopy.<sup>38</sup> For this instance, 15 mg of MOF were digested in 1 M NH<sub>4</sub>CO<sub>3</sub> solution in D<sub>2</sub>O for 2 h. <sup>1</sup>H-NMR spectra were recorded on a Bruker Ascend 400 MHz Spectrometer. Argon physisorption measurements were performed at 87 K on a 3Flex instrument from micromeritics. The samples (25 mg) were activated at 150 °C under secondary vacuum for 20 h. For the analysis of the data the associated software was used. BET areas were determined by the BET-auto function of the software and total pore volumes were calculated with single-point

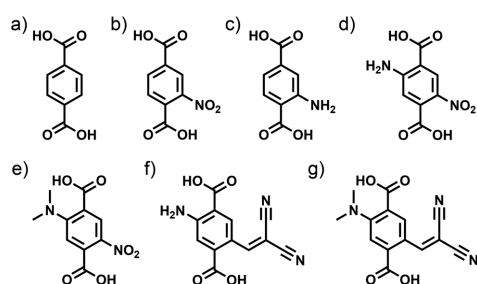


Fig. 1 Linkers in the UiO-66 MOFs investigated with (a) no functionalization, (b) NO<sub>2</sub> group (c) NH<sub>2</sub> group; and novel bifunctional linker molecules with (d) NH<sub>2</sub> and NO<sub>2</sub>, (e) N(Me)<sub>2</sub> and NO<sub>2</sub>, (f) NH<sub>2</sub> and DCV and (g) N(Me)<sub>2</sub> and DCV groups.

method at a relative pressure of 0.95. Scanning electron microscope (SEM) images were recorded with a JEOL JSM-6700F microscope using an accelerating voltage of 2 kV with a working distance of 8 mm. The SEM samples were prepared by dispersion of small amounts of MOF powder in ethanol using an ultrasonic bath. The dispersion was dropped onto a polished graphite block and dried at room temperature. Thermogravimetric measurements were performed on a Netzsch STA 449 F5 Jupiter in synthetic air ( $N_2$ ,  $O_2$ ) with a heating rate of  $5 \text{ K min}^{-1}$  using 10 mg of MOF powder.

#### Computational details

Kohn–Sham density functional theory calculations were performed using the CASTEP code (version 20.1) employing a plane-wave basis set in combination with pseudopotentials.<sup>39,40</sup> UiO-66 and its analogues were modelled with primitive cells of the fcc lattice with 114 to 198 atoms depending on the functionalisation. The convergence of the plane-wave kinetic energy cutoff and the Brillouin zone sampling were examined with respect to the lattice parameters (see ESI,† Section S2) and set to 1000 eV for UiO-66 and 800 eV for the derivatives with  $\Gamma$ -point sampling. The pseudopotentials were generated on-the-fly with the Koelling–Harmon method to incorporate relativistic effects into the generated pseudopotentials.<sup>41</sup> The PBEsol exchange–correlation functional was used to fully relax the structures using “on-the-fly” generated ultra-soft pseudopotentials with an SCF convergence criterion of  $5.0 \times 10^{-7}$  eV per atom.<sup>42</sup> Applying a low-memory Broyden–Fletcher–Goldfarb–Shanno (LBFGS) algorithm, structures with an energy change of less than  $5.0 \times 10^{-6}$  eV per atom and a maximal force of  $0.01 \text{ eV \AA}^{-1}$  were obtained. The convergence threshold of the stress and maximal atom displacement were 0.02 GPa and  $5.0 \times 10^{-4} \text{ \AA}$ , respectively.

Subsequently three different exchange–correlation (XC) functionals were assessed with regard to the lattice parameters of the UiO-66 and its analogues to obtain precise structural models for further characterisation. To determine suitable XC functionals, full cell relaxations were performed using the parameters described above. The benchmark included the generalized gradient approximation (GGA) functional of Perdew, Burke, and Ernzerhof (PBE) with D2 and TS dispersion correction, respectively, the PBE expansion for solids (PBEsol) and its dispersion corrected form (PBEsol-TS), and the rSCAN meta-GGA functional.<sup>42–47</sup>

Using the optimized models, single point HSE06 hybrid DFT calculations were performed to obtain the band structures, the corresponding density of states (DOS) and the dispersion of the refractive index.<sup>32</sup> All calculations were carried out using  $\Gamma$ -point Brillouin zone sampling with the determined plane-wave kinetic energy cutoff values and a SCF convergence criterion of  $10^{-9}$  eV per atom. The optical properties were calculated applying the tools provided within CASTEP to evaluate the electronic structure, obtain the complex dielectric function and subsequently the dispersion of the index of refraction.<sup>48</sup>

## Results and discussion

This study is concerned with UiO-66-type MOFs containing the linker molecules depicted in Fig. 1. Of these, UiO-66 as well as

its amino and nitro derivative are well-known. In addition, we have synthesized the novel UiO-66-( $NH_2,NO_2$ ) with the *pnadc* push–pull linker. We first describe the results of the characterization of these experimentally accessible MOFs prior to focussing on the results of the calculations of the electronic and optical properties of MOFs with all the linkers depicted in Fig. 1.

#### Experimental studies on UiO-66-type MOFs

UiO-66 derivatives were synthesized *via* the standard synthesis route with DMF as solvent and using the modulation approach which was introduced for the synthesis of Zr-MOFs by our group.<sup>49</sup> By using this approach the well-known UiO-66 derivatives, as well as the novel UiO-66-( $NH_2,NO_2$ ), were obtained with a high crystallinity as proven by the PXRD measurements depicted in Fig. 2 left. UV-Vis DRS measurements show that unfunctionalized UiO-66 only exhibits absorption in the UV region, whereas its derivatives all feature a second adsorption maximum at a higher wavelength which is contributed by the functional groups introduced into the framework (Fig. 2 right). Whereas this additional absorption is only weak in the case of UiO-66-( $NO_2$ ), it is pronounced upon the incorporation of amino groups into the framework. The successful incorporation of the linker molecules into the framework and the complete removal of solvents during work-up were verified with  $^1H$ -NMR-spectroscopy on digested samples (see ESI,† Fig. S4). The recorded spectra substantiate that the phase-pure samples were solvent-free and that the linker molecules were not altered during the solvothermal synthesis.

Further analysis *via* argon physisorption measurements on the novel UiO-66-( $NH_2,NO_2$ ) reveals the intact porosity of this framework after solvent exchange and activation (see ESI,† Fig. S1). A typical type I isotherm, characteristic for microporous materials like UiO-66 derivatives, was obtained, with a BET area of  $932 \text{ m}^2 \text{ g}^{-1}$  and a pore volume of  $0.385 \text{ cm}^3 \text{ g}^{-1}$ . Thermogravimetric analysis suggests that the framework has thermal stability up to  $300 \text{ }^\circ\text{C}$  (see ESI,† Fig. S2). Scanning electron microscope (SEM) images of UiO-66-( $NH_2,NO_2$ ) show that the material appears as intergrown octahedral particles with a size in the nanometer range (see ESI,† Fig. S3).

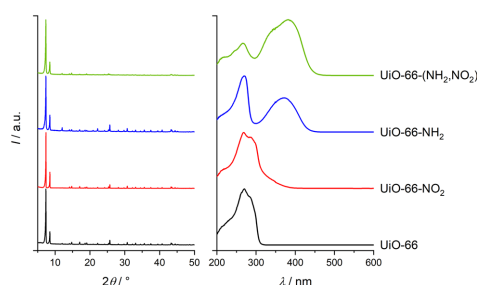


Fig. 2 PXRD patterns (left) and UV-Vis spectra (right) of UiO-66, its monofunctionalized derivatives UiO-66- $NO_2$  and UiO-66- $NH_2$ , and of the novel bifunctional UiO-66-( $NH_2,NO_2$ ).



### 3.1 Tuning the optical properties of the metal-organic framework UiO-66 via ligand functionalization

View Article Online

Paper

PCCP

#### Structure of UiO-66 and its analogues

This comprehensive DFT study includes UiO-66, its well-known amino- and nitro-derivatives and four novel MOFs containing push–pull linkers. With one of the push–pull linkers, amino-nitro benzene dicarboxylate, a UiO-66-MOF was also obtained experimentally for the first time (see above). The “push” units included here are amino and dimethylamino, the “pull” units employed are nitro and dicyanovinyl groups.

UiO-66 crystallizes in space group  $F\bar{4}3m$  with an experimental lattice parameter of  $a = 20.747 \text{ \AA}$  containing four primitive triclinic cells ( $a_p = 14.670 \text{ \AA}$ ).<sup>50</sup> As the PXRD diagrams in Fig. 2 show, the two synthesized monofunctional derivatives (UiO-66-NO<sub>2</sub>, UiO-66-NH<sub>2</sub>) and the novel bifunctional (UiO-66-(NH<sub>2</sub>,NO<sub>2</sub>)) derivative are topologically equivalent with UiO-66 and have closely matching lattice parameters. It was assumed that also the *in silico*-designed bifunctional derivatives will share the UiO-66 topology and lattice parameters. Relying on this hypothesis, suitable XC functionals were assessed to describe the structures with suitable models by comparing the calculated lattice parameters with experimental ones of the pure UiO-66 (see ESI,† Section S3). It was found, that the PBEsol and rSCAN functionals lead to fully optimized structures with an error of less than 1% for the average lattice parameter  $a_p$  while the use of the PBEsol functional with TS dispersion correction (PBEsol-TS) consistently results in structures with less than 0.2% error (see Table 1). Only in the case of the unmodified UiO-66 the meta-GGA rSCAN functional outperforms the PBEsol-TS functional, proving the improved performance of dispersion-corrected GGA functionals and the capability of the PBEsol functional regarding the accurate description of crystal structures.

In this study, all UiO-66 derivatives were modelled within space group  $P1$ , which introduces higher degrees of freedom during the cell relaxation. As a result, the lattice constants are optimized independently and an average lattice parameter  $a_p$  was introduced. Although slight distortions of the primitive cells occurred compared to UiO-66, the shape of the primitive cells basically remained unchanged and stayed comparable to the one of UiO-66, confirming that the functionalisation of the UiO-66 leads to isostructural derivatives with nearly unchanged lattice parameters. This underlines the stability of the UiO-66 topology regarding the use of functionalized linker molecules and shows that even linkers carrying large push–pull motifs can be incorporated. Additionally, the fact that calculated lattice parameters lie close to experimental ones shows that the

careful convergence of the basis set allows very precise structural descriptions of the examined MOFs.

#### Electronic structure of UiO-66 and its analogues

It has been repeatedly shown that the electronic structure of UiO-66 derivatives can be altered by introducing further functional groups on the *bdc* linker. Thus, also the optical properties of UiO-66 depend on the type of functionalisation.<sup>8,12,22,51</sup> In this section we focus on the electronic structure of UiO-66 and its analogues to evaluate the effect of the mono- and bifunctional linker functionalisation.

We carried out electronic structure calculations on hybrid DFT level (see ESI,† Section S4) and validated the results with regard to band gaps extracted from solid state UV-Vis DRS (see Fig. 2 right) determined using Tauc plots (see ESI,† Fig. S5) of phase-pure samples of the experimentally accessible MOFs. The calculated band gaps are compared with the experimental ones in Fig. 3. The HSE06 calculations reproduce the experimental trend and are in good agreement with the measured band gaps; additionally, the calculated values are coherent with the HSE06 studies of UiO-66 and UiO-66-NH<sub>2</sub> in literature.<sup>8,12,52,53</sup> Moreover, we report the first HSE06 electronic structure calculation of UiO-66-NO<sub>2</sub>. The calculated band gap is in accordance with

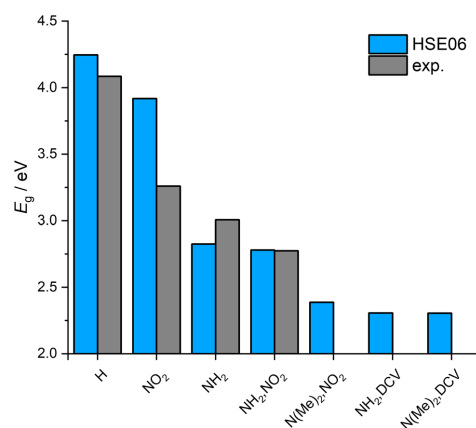


Fig. 3 Comparison of calculated (HSE06) and experimental (exp.) band gaps.

Table 1 Details of the DFT study and generated structural models of UiO-66 derivatives: plane-wave kinetic energy cutoff, exchange–correlation functional, average lattice parameter of the optimized primitive cell and its deviation compared with the experimental UiO-66 value

MOF	Abbreviation	$E_{\text{cutoff}}/\text{eV}$	XC functional	$a_p/\text{\AA}$	Deviation/%
UiO-66 (exp.) <sup>50</sup>				14.670	
UiO-66	H	1000	rSCAN	14.677	0.050
UiO-66-NO <sub>2</sub>	NO <sub>2</sub>	800	PBEsol-TS	14.652 ± 0.004	0.123
UiO-66-NH <sub>2</sub>	NH <sub>2</sub>	800	PBEsol-TS	14.647 ± 0.010	0.154
UiO-66-(NH <sub>2</sub> ,NO <sub>2</sub> )	NH <sub>2</sub> , NO <sub>2</sub>	800	PBEsol-TS	14.674 ± 0.023	0.025
UiO-66-(N(Me) <sub>2</sub> ,NO <sub>2</sub> )	N(Me) <sub>2</sub> , NO <sub>2</sub>	800	PBEsol-TS	14.691 ± 0.021	0.146
UiO-66-(NH <sub>2</sub> ,DCV)	NH <sub>2</sub> , DCV	800	PBEsol-TS	14.675 ± 0.074	0.034
UiO-66-(N(Me) <sub>2</sub> ,DCV)	N(Me) <sub>2</sub> , DCV	800	PBEsol-TS	14.669 ± 0.023	0.006

the published HSE03-based study of Flage-Larsen *et al.*<sup>22</sup> The band structure calculation of UiO-66-(NH<sub>2</sub>,NO<sub>2</sub>) yields a band gap of 2.78 eV, which compares well to the experimental value of 2.91 eV. Furthermore the predicted small difference in the band gap values of UiO-66-NH<sub>2</sub> and UiO-66-(NH<sub>2</sub>,NO<sub>2</sub>) was observed in the experiment.

In general, the functionalisation of UiO-66 reduces the band gap. In particular, electron-donating “push” substituents lower the band gap more than electron-withdrawing “pull” ones. A direct look on the calculated band structures as depicted in Fig. 4 gives further information. Electron-donating groups like the amino group mainly introduce new states above the valence band maximum (VBM) of unfunctionalized UiO-66, basically forming band gap states with regard to the parent UiO-66 band structure. On the contrary, electron withdrawing groups like the nitro group only introduce states located near to the VBM, resulting in a discernible, but smaller influence on the band gap (see Fig. 4). By analysing the projected density of states (PDOS), it becomes clear, that the small influence of the electron-withdrawing substituents on the band gap originates from the strongly bound electrons forming localized states.

In the case of the NO<sub>2</sub>-functionalisation, the VBM states belong to the oxygen atoms of the nitro-groups (O<sub>NO<sub>2</sub></sub>) while the nitrogen atom forms unoccupied states in the conduction band. The strongly bound electrons of O<sub>NO<sub>2</sub></sub> lead to eigenstates with just slightly more energy than those of the oxygen atoms forming the IBU (O<sub>IBU</sub>). This increases the density of states at the top of the valence band but has only a small effect on the band gap. In contrast, the band gap states introduced by the electron-donating substituents are generated by unbound delocalized electrons, which in the case of the amino-substituents are formed by the free electron pair of the nitrogen atoms and the electrons of the benzene ring. These states have a significant higher energy compared to the O<sub>IBU</sub> states, leading to the formation of separated states which increase the VBM and correspondingly lower the band gap notably.

Using the characteristics of the nitro- and amino-model systems, we proceed with describing the electronic structures of UiO-66 derivatives containing bifunctional linkers featuring an electron-withdrawing and an electron-donating substituent within the same linker molecule. This leads to the insertion of further band gap states and of states at the conduction band

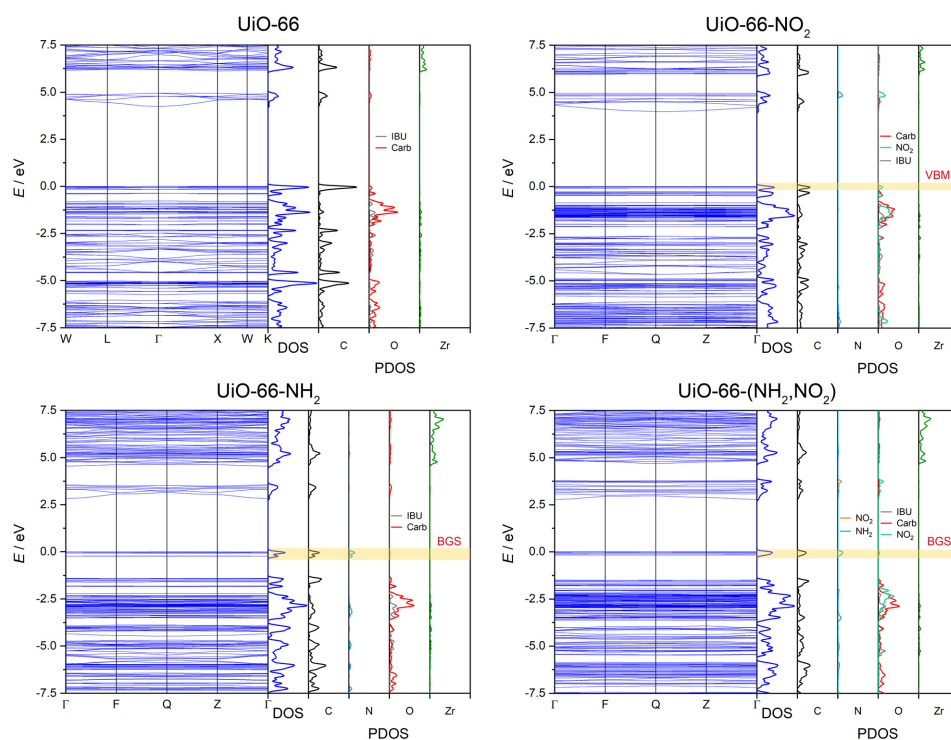


Fig. 4 Band structures with density of states (DOS) and projected density of states (PDOS) of UiO-66, UiO-66-NO<sub>2</sub>, UiO-66-NH<sub>2</sub> and UiO-66-(NH<sub>2</sub>,NO<sub>2</sub>). The valence band maximum (VBM) and band gap states (BGS) are highlighted.

### 3.1 Tuning the optical properties of the metal-organic framework UiO-66 via ligand functionalization

Paper

View Article Online

PCCP

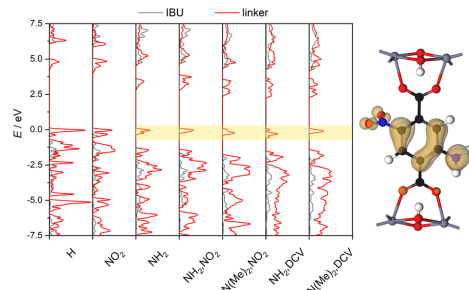


Fig. 5 Left: Projected density of states of IBU (grey) and of linker atoms (red) with highlighted band gap states. Right: Projected electron density of UiO-66-(NH<sub>2</sub>,NO<sub>2</sub>) band gap states (isosurface value 0.03 e Å<sup>-3</sup>).

minimum (CBM), both influencing the band gap and thus allowing for tuning the resulting optical properties. For instance, the bifunctional UiO-66-(NH<sub>2</sub>,NO<sub>2</sub>) features the VBM states characteristics of the amino-functionalisation and the CBM states typical of the nitro-functionalisation. Insertion of these states results in a smaller band gap while increasing the number of states at the CBM and VBM. This should lead to a higher refractive index in the visible range, due on the one hand to the red shift and on the other to the higher intensity of the absorption coupled with an increased polarizability which allows the tailoring of UiO-66-based optical materials using bifunctional linkers.

To analyze the effect of the different bifunctional linkers on the electronic structure of the resulting MOFs, the PDOS of the IBU and the corresponding linker including the oxygen atoms of the carboxylate are compared (Fig. 5). In the case of UiO-66-(NH<sub>2</sub>,NO<sub>2</sub>) the PDOS of the linker highlights the increased number of VBM and CBM states with regard to the MOFs with monofunctional linkers. The projected electron density of the UiO-66-(NH<sub>2</sub>,NO<sub>2</sub>) band gap states reveals the influence of the free electrons originating from the nitrogen atom of the

electron-donating amino group and underlines that the electron-withdrawing nitro group with its free electrons located at the oxygen atoms also contributes to the VBM. Thus, the use of a bifunctional push-pull-linker enables band gap tuning by altering the VBM and CBM states simultaneously.

With the introduction of our novel bifunctional linkers, the number of band gap and CBM states were extended inducing a further reduction of the band gap. Especially, the expansion of the VBM states occurring in all systems with N(Me)<sub>2</sub>- and DCV-groups enhances the polarizability of the linker, leading to a more intense absorption and thus promoting a higher index of refraction, regardless of the small changes in the band gap.

#### Optical properties of UiO-66 and its analogues

We used hybrid DFT calculations to determine the dielectric function and obtain the dispersion of the refractive index (RI) of the studied UiO-66 materials. Fig. 6 shows impressively the broad range of RI values accessible with one framework topology *via* modification of the linker functionalisation. The parent UiO-66 shows a band gap larger than 4 eV leading to a typical RI dispersion in the visible range for an insulator. At 589 nm UiO-66 exhibits a RI of 1.37 increasing towards shorter wavelengths (due to the upcoming absorption in the UV) and decreasing monotonically with longer wavelengths to finally become constant. Our HSE06-based calculation of the optical properties results in a static RI of about 1.35. This is below the reported values of 1.5 and 1.47 presented in previous studies using the PBE functional with an applied scissors operator to correct the underestimated band gap.<sup>9,54</sup> The latter values might be overestimated, because the sole application of the scissors operator without further correction to satisfy the sum rule can lead to overrated amplitudes in the dielectric function and thus to a shifted refractive index.<sup>55</sup> Using the PBE functional without a scissors operator results in even larger RI values due to the well-known underestimation of the band gap by the PBE functional (see ESI,<sup>†</sup> Section S6).

The monofunctional UiO-66 derivatives show reduced band gaps and higher electron densities at the VBM and CBM,

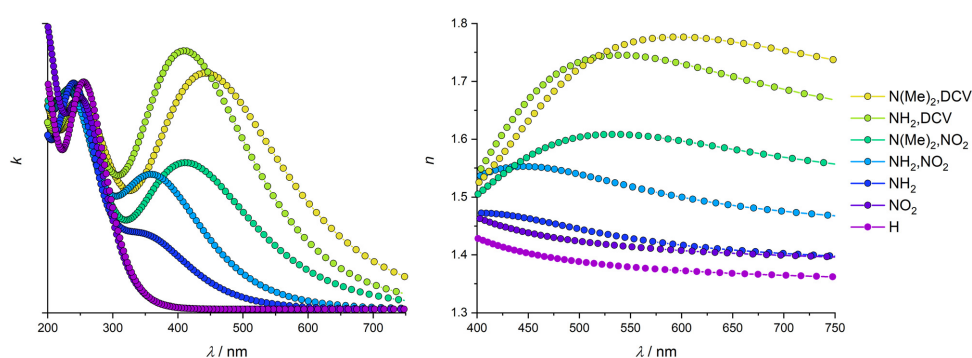


Fig. 6 Calculated complex refractive index dispersion. Left: Extinction coefficient (imaginary part); right: refractive index (real part).

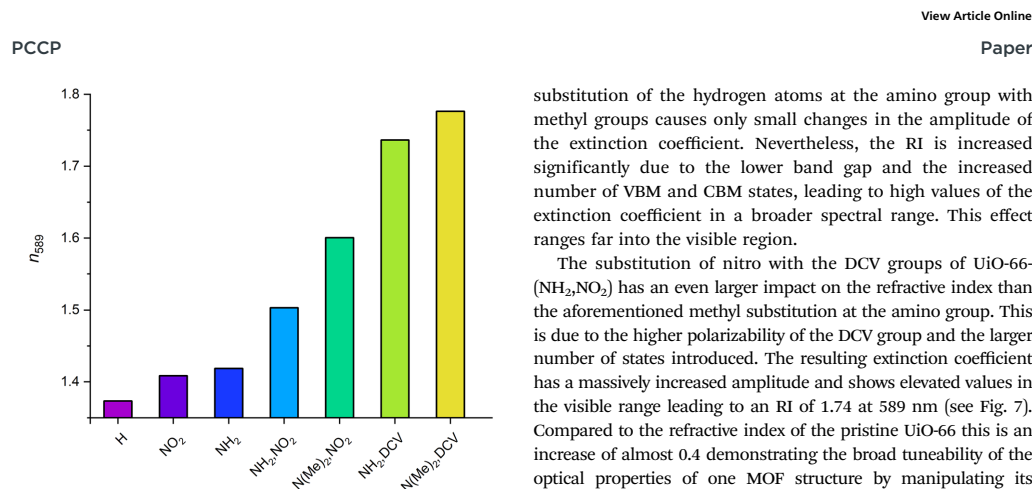


Fig. 7 Comparison of the calculated refractive indices of UiO-66 and its analogues at 589 nm.

respectively, in comparison to bare UiO-66, leading to a redshift of the maximum of the extinction coefficient (see Fig. 6) and thus to slightly higher indices of refraction, namely 1.41 and 1.42 for UiO-66-NH<sub>2</sub> and UiO-66-NO<sub>2</sub>, respectively (see Fig. 7). In general, all dispersion curves exhibit a comparable trend. At the low energy end of the dispersion the amino- and nitro-derivatives are very similar, but they diverge towards higher energies. The plateau visible in the dispersion curve of UiO-66-NH<sub>2</sub> around 400 nm is caused by the lower band gap of that congener resulting in the absorption of light with wavelengths just below the visible range. This corresponds to the increased extinction in the visible range caused by a maximum at around 360 nm. In contrast, the UiO-66-NO<sub>2</sub> shows a dispersion profile similar to UiO-66, as its band gap is larger than that of UiO-66-NH<sub>2</sub> and polarizability is lower.

On the contrary, UiO-66-(NH<sub>2</sub>,NO<sub>2</sub>) has a significantly higher RI (1.50 at 589 nm) due to its smaller band gap and the larger number of states at the CBM and VBM, elevating the polarizability of the linker and enabling more excitations with an energy just above the band gap to take place; this leads to a more intense absorption corresponding to a strong increase in the extinction coefficient. This absorption takes place in the blue region of the visible light due to the smaller band gap. The absorption of visible light corresponds to the yellow colour of this compound which was also investigated experimentally. However, such an absorption in the visible range might prevent the application of the UiO-66-(NH<sub>2</sub>,NO<sub>2</sub>) in certain devices where materials which are transparent in the visible range of the light are needed; nevertheless, UiO-66-(NH<sub>2</sub>,NO<sub>2</sub>) provides a robust material with reasonably high RI for optical systems applied at longer wavelengths.

The bifunctional UiO-66 analogues with more extended electron-donating or -withdrawing groups follow the trend of the UiO-66-(NH<sub>2</sub>,NO<sub>2</sub>) and show higher RIs while having a larger bathochromic shift (see ESI,† Table S2). A comparison of the extinction coefficients of UiO-66-(NH<sub>2</sub>,NO<sub>2</sub>) and UiO-66-(NMe<sub>2</sub>,NO<sub>2</sub>) reveals that the

substitution of the hydrogen atoms at the amino group with methyl groups causes only small changes in the amplitude of the extinction coefficient. Nevertheless, the RI is increased significantly due to the lower band gap and the increased number of VBM and CBM states, leading to high values of the extinction coefficient in a broader spectral range. This effect ranges far into the visible region.

The substitution of nitro with the DCV groups of UiO-66-(NH<sub>2</sub>,NO<sub>2</sub>) has an even larger impact on the refractive index than the aforementioned methyl substitution at the amino group. This is due to the higher polarizability of the DCV group and the larger number of states introduced. The resulting extinction coefficient has a massively increased amplitude and shows elevated values in the visible range leading to an RI of 1.74 at 589 nm (see Fig. 7). Compared to the refractive index of the pristine UiO-66 this is an increase of almost 0.4 demonstrating the broad tuneability of the optical properties of one MOF structure by manipulating its linkers.

The highest RI values are accessible with the UiO-66-(N(Me)<sub>2</sub>,DCV) which, however, is also non-transparent for roughly half of the visible spectrum. This can be ascribed to the small band gap and the large polarizability. Despite that, it might be used as a highly refractive material for applications in the near infra-red regime.

Altogether, UiO-66 and its derivatives are promising materials for optical applications based on their high chemical stability and the tuneability of their RIs. They enable the construction of optical systems using light from the upper half of the visible range and from the near IR region. The wide range of refractive indices allows the design of complex optical systems needing materials with different RIs, for example optical filter or coatings.

## Conclusions

The electronic structure and the resulting optical properties of the Zr-based UiO-66 MOF and of mono- and bifunctional derivatives have been investigated using the hybrid HSE06 DFT functional. Four novel bifunctional push-pull linkers were introduced for theoretical calculations; for one of those linkers, the successful synthesis of the novel UiO-66-(NH<sub>2</sub>,NO<sub>2</sub>)-MOF is reported which contains the *bdc* analogue of *para*-nitroaniline.

Utilising carefully converged plane-wave basis sets, periodic models were fully relaxed with different functionals to assess a suitable and precise representation of each material. The lattice parameters of the resulting functionalized structures are comparable with the ones of the pristine UiO-66 showing the broad possibilities for substitution within the isostructural UiO-66 family. These structural models were then used to conduct electronic structure calculations. The approach used here is based on carefully converged basis sets and an XC functional benchmark for each structure. To the best of our knowledge, this is the first work that fully relies on computationally demanding hybrid DFT calculations to obtain optical properties of MOFs. The method was validated by comparing the calculated band gaps with experimentally determined ones obtained from DRS UV-Vis measurement. The good agreement shows

### 3.1 Tuning the optical properties of the metal-organic framework UiO-66 via ligand functionalization

View Article Online

Paper

PCCP

that high-level precise electronic structure calculations are able to provide reliable values for the band gap. Precise electronic structures also ensure the calculation of trustworthy values of the refractive index as a major optical material property. Incorporating bifunctional linker molecules, the band gaps were found to be drastically reduced. Further analysis *via* the PDOS of the materials showed that the reduction of the band gap occurs due to the introduction of numerous states at the CBM and in the band gap of the parent UiO-66, resulting for the derivatives in a new CBM at lower energies as well as a new VBM. Subsequently, the dispersion curves of the refractive index were calculated for each material. This reveals the direct influence of, on the one hand, the band gap energy on the refractive index; on the other hand, it also becomes clear that higher density of states at the VBM and CBM lead to significantly increased extinction coefficients, in turn also giving rise to higher refractive indices.

In total, the wide range spanned by the indices of refraction determined in this work demonstrates the capabilities offered by MOFs as optical materials. Their modular design allows to obtain materials tuned for specific optical applications, also ones which require high refractive indices. In particular, the functionalisation of linker molecules has been presented as simple and effective method to generate materials with the same topology and similar synthesis protocols, but featuring distinct optical properties.

The MOFs treated here, based on push-pull systems, are very well suited for applications in the near IR. The absorption in the visible range of wavelengths may, however, cause problems in applications addressing this range of wavelengths. From our study we propose that future work to circumvent this problem should focus on providing linker functions with high polarizabilities, but without the introduction of extended push-pull systems. MOFs with such linkers should provide high refractive indices combined with band gaps above 3 eV. Thus, the extinction maximum lies in the UV region and the resulting material should be transparent in the visible range.

#### Conflicts of interest

There are no conflicts to declare.

#### Acknowledgements

We acknowledge the support of the cluster system team at the Leibniz University of Hannover, Germany in the production of this work. This work is funded by the DFG under Germany's Excellence Strategy within the Cluster of Excellence PhoenixD (EXC 2122, Project ID 390833453). A. H. is grateful for being funded by the Hannover School for Nanotechnology (HSN) at the Laboratory of Nano and Quantum Engineering (LNQE). The HSN is funded by the Ministry of Science and Culture of Lower Saxony.

#### Notes and references

- 1 S. R. Batten, N. R. Champness, X.-M. Chen, J. Garcia-Martinez, S. Kitagawa, L. Öhrström, M. O'Keeffe, M. Paik Suh and J. Reedijk, *Pure Appl. Chem.*, 2013, **85**, 710.
- 2 J. L. Rowsell and O. M. Yaghi, *Microporous Mesoporous Mater.*, 2004, **73**, 3.
- 3 A. Dhakshinamoorthy, Z. Li and H. Garcia, *Chem. Soc. Rev.*, 2018, **47**, 8134.
- 4 H. Li, K. Wang, Y. Sun, C. T. Lollar, J. Li and H.-C. Zhou, *Mater. Today*, 2018, **21**, 108.
- 5 L. E. Kreno, K. Leong, O. K. Farha, M. Allendorf, R. P. van Duyne and J. T. Hupp, *Chem. Rev.*, 2012, **112**, 1105.
- 6 Y. Zheng, F.-Z. Sun, X. Han, J. Xu and X.-H. Bu, *Adv. Opt. Mater.*, 2020, **8**, 2000110.
- 7 Y. Huang, C.-A. Tao, R. Chen, L. Sheng and J. Wang, *Nanomaterials*, 2018, **8**, 676.
- 8 B. Ni, W. Sun, J. Kang and Y. Zhang, *J. Phys. Chem. C*, 2020, **124**, 11595.
- 9 H. Li, L. Zhang, H. He, Y. Yang, Y. Cui and G. Qian, *Sci. China Mater.*, 2021, **64**, 698.
- 10 K.-T. Hsu, P. Thanasekaran, T.-W. Hsu, C.-H. Su, B.-C. Chang, Y.-H. Liu, C.-H. Hung and K.-L. Lu, *CrystEngComm*, 2021, **23**, 824.
- 11 M. A. Syzgantseva, C. P. Ireland, F. M. Ebrahim, B. Smit and O. A. Syzgantseva, *J. Am. Chem. Soc.*, 2019, **141**, 6271.
- 12 K. Hendrickx, D. E. P. Vanpoucke, K. Leus, K. Lejaeghere, A. van Yperen-De Deyne, V. van Speybroeck, P. van der Voort and K. Hemelsoet, *Inorg. Chem.*, 2015, **54**, 10701.
- 13 W. Yin, C.-A. Tao, F. Wang, J. Huang, T. Qu and J. Wang, *Sci. China Mater.*, 2018, **61**, 391.
- 14 K. Müller, K. Fink, L. Schöttner, M. Koenig, L. Heinke and C. Wöll, *ACS Appl. Mater. Interfaces*, 2017, **9**, 37463.
- 15 N. C. Keppler, K. D. J. Hindricks and P. Behrens, *RSC Adv.*, 2022, **12**, 5807.
- 16 Y. Bai, Y. Dou, L.-H. Xie, W. Rutledge, J.-R. Li and H.-C. Zhou, *Chem. Soc. Rev.*, 2016, **45**, 2327.
- 17 J. H. Cavka, S. Jakobsen, U. Olsbye, N. Guillou, C. Lamberti, S. Bordiga and K. P. Lillerud, *J. Am. Chem. Soc.*, 2008, **130**, 13850.
- 18 S. J. Garibay and S. M. Cohen, *Chem. Commun.*, 2010, **46**, 7700.
- 19 M. Kandiah, M. H. Nilsen, S. Usseglio, S. Jakobsen, U. Olsbye, M. Tilset, C. Larabi, E. A. Quadrelli, F. Bonino and K. P. Lillerud, *Chem. Mater.*, 2010, **22**, 6632.
- 20 G. E. Cmarik, M. Kim, S. M. Cohen and K. S. Walton, *Langmuir*, 2012, **28**, 15606.
- 21 F. Vermoortele, M. Vandichel, B. van de Voorde, R. Ameloot, M. Waroquier, V. van Speybroeck and D. E. de Vos, *Angew. Chem., Int. Ed.*, 2012, **51**, 4887.
- 22 E. Flage-Larsen, A. Røyset, J. H. Cavka and K. Thorshaug, *J. Phys. Chem. C*, 2013, **117**, 20610.
- 23 W. Vandezande, K. P. F. Janssen, F. Delpont, R. Ameloot, D. E. de Vos, J. Lammertyn and M. B. J. Roeffaers, *Anal. Chem.*, 2017, **89**, 4480.
- 24 K.-J. Kim, P. Lu, J. T. Culp and P. R. Ohodnicki, *ACS Sens.*, 2018, **3**, 386.

### 3 Results and discussion

View Article Online

PCCP

Paper

- 25 A. Demessence, C. Boissière, D. Grosso, P. Horcajada, C. Serre, G. Férey, G. J. A. A. Soler-Illia and C. Sanchez, *J. Mater. Chem.*, 2010, **20**, 7676.
- 26 O. Dalstein, D. R. Ceratti, C. Boissière, D. Grosso, A. Cattoni and M. Faustini, *Adv. Funct. Mater.*, 2016, **26**, 81.
- 27 P. Horcajada, C. Serre, D. Grosso, C. Boissière, S. Perruchas, C. Sanchez and G. Férey, *Adv. Mater.*, 2009, **21**, 1931.
- 28 E. Redel, Z. Wang, S. Walheim, J. Liu, H. Gliemann and C. Wöll, *Appl. Phys. Lett.*, 2013, **103**, 91903.
- 29 W. Yin, C.-A. Tao, X. Zou, F. Wang, T. Qu and J. Wang, *Nanomaterials*, 2017, **7**, 242.
- 30 L. Zheng, N. Keppler, H. Zhang, A. Günther, P. Behrens and B. Roth, in *Integrated Optics: Devices, Materials, and Technologies XXVI*, SPIE, 2022, p. 15.
- 31 L. Zheng, N. Keppler, H. Zhang, P. Behrens and B. Roth, *Adv. Mater. Technol.*, 2022, **7**, 2200395.
- 32 A. V. Krukau, O. A. Vydrov, A. F. Izmaylov and G. E. Scuseria, *J. Chem. Phys.*, 2006, **125**, 224106.
- 33 J. Paier, M. Marsman, K. Hummer, G. Kresse, I. C. Gerber and J. G. Ángyán, *J. Chem. Phys.*, 2006, **125**, 249901.
- 34 A. J. Garza and G. E. Scuseria, *J. Phys. Chem. Lett.*, 2016, **7**, 4165.
- 35 M. Nishiwaki and H. Fujiwara, *Comput. Mater. Sci.*, 2020, **172**, 109315.
- 36 K. Markey, M. Krüger, T. Seidler, H. Reinsch, T. Verbiest, D. E. de Vos, B. Champagne, N. Stock and M. A. van der Veen, *J. Phys. Chem. C*, 2017, **121**, 25509.
- 37 G. C. Shearer, S. Chavan, J. Ethiraj, J. G. Vitillo, S. Svelle, U. Olsbye, C. Lamberti, S. Bordiga and K. P. Lillerud, *Chem. Mater.*, 2014, **26**, 4068.
- 38 J. Chu, F.-S. Ke, Y. Wang, X. Feng, W. Chen, X. Ai, H. Yang and Y. Cao, *Commun. Chem.*, 2020, **3**, 5.
- 39 S. J. Clark, M. D. Segall, C. J. Pickard, P. J. Hasnip, M. I. J. Probert, K. Refson and M. C. Payne, *Z. Kristallogr.*, 2005, **220**, 567.
- 40 W. Kohn and L. J. Sham, *Phys. Rev.*, 1965, **140**, A1133–A1138.
- 41 D. D. Koelling and B. N. Harmon, *J. Phys. C: Solid State Phys.*, 1977, **10**, 3107.
- 42 J. P. Perdew, A. Ruzsinszky, G. I. Csonka, O. A. Vydrov, G. E. Scuseria, L. A. Constantin, X. Zhou and K. Burke, *Phys. Rev. Lett.*, 2008, **100**, 136406.
- 43 J. P. Perdew, K. Burke and M. Ernzerhof, *Phys. Rev. Lett.*, 1996, **77**, 3865.
- 44 S. Grimme, *J. Comput. Chem.*, 2006, **27**, 1787.
- 45 A. Tkatchenko and M. Scheffler, *Phys. Rev. Lett.*, 2009, **102**, 73005.
- 46 W. A. Al-Saidi, V. K. Voora and K. D. Jordan, *J. Chem. Theory Comput.*, 2012, **8**, 1503.
- 47 A. P. Bartók and J. R. Yates, *J. Chem. Phys.*, 2019, **150**, 161101.
- 48 A. J. Morris, R. J. Nicholls, C. J. Pickard and J. R. Yates, *Comput. Phys. Commun.*, 2014, **185**, 1477.
- 49 A. Schaate, P. Roy, A. Godt, J. Lippke, F. Waltz, M. Wiebeke and P. Behrens, *Chem. – Eur. J.*, 2011, **17**, 6643.
- 50 S. Øien, D. Wragg, H. Reinsch, S. Svelle, S. Bordiga, C. Lamberti and K. P. Lillerud, *Cryst. Growth Des.*, 2014, **14**, 5370.
- 51 T. Musho, J. Li and N. Wu, *Phys. Chem. Chem. Phys.*, 2014, **16**, 23646.
- 52 K. Hendrickx, D. E. P. Vanpoucke, K. Leus, K. Lejaeghere, A. van Yperen-De Deyne, V. van Speybroeck, P. van der Voort and K. Hemelsoet, *Inorg. Chem.*, 2015, **54**, 10701.
- 53 K. L. Svane, J. K. Bristow, J. D. Gale and A. Walsh, *J. Mater. Chem. A*, 2018, **6**, 8507.
- 54 L.-M. Yang, E. Ganz, S. Svelle and M. Tilset, *J. Mater. Chem. C*, 2014, **2**, 7111.
- 55 M. Nishiwaki and H. Fujiwara, *Comput. Mater. Sci.*, 2020, **172**, 109315.

## 3.2 Development of high refractive index UiO-66 framework derivatives via ligand halogenation

### Preface

This study was published as full paper in the journal “Physical chemistry chemical physics: PCCP” of the Royal Society of Chemistry and is based on the simulation approach presented in the previous publication. Here, the electronic structures of UiO-66-type MOFs are studied to elaborate the influences of the halogenation of the *bdc* linker regarding the refractive index of the resulting compounds. The correct description of the electronic structure and thus the optical properties of the investigated MOFs was validated with UV-Vis DRS. The effect on the optical properties due to the introduction of halogen atoms to the *bdc* linker was studied with the monohalogenated UiO-66 derivatives denoted as UiO-66-*X* (*X* = F, Cl, Br, I). The optical properties of these monohalogenated UiO-66 analogues are compared with the qualitative calculations already present in literature. Furthermore, a novel dihalogenated UiO-66 derivative featuring a *bdc* linker with two iodine atoms in *para* position was presented, synthesized, and fully characterized. The obtained UiO-66-I<sub>2</sub> MOF shows high RI values due to the introduction of a large number of delocalised electrons resulting a high polarisability of the framework.

In total, it was proven that the halogenation of linkers is a simple but effective method to exploit the modular design of MOFs to obtain materials with tailored optical properties. In addition, two shortcomings of the previous study were eliminated. First, the materials described here are transparent in the Vis spectral region and some of them even enable applications in the UV region widening up the field of possible applications. Second, the halogenation of the linkers preserves the porosity of the framework enabling the incorporation of guest molecules to further tune the RI or perform gas sensing.

The author of this thesis performed all calculations, evaluated the experimental UV-Vis DRS data provided by Adrian Hannebauer and wrote the majority of the manuscript. Adrian Hannebauer synthesized all MOF samples and analyzed them with PXRD, SEM, TGA, UV-Vis DRS and physisorption measurements. Furthermore, he wrote the experimental part of the manuscript. This study was guided by Prof. Dr. Peter Behrens and Dr. Andreas M. Schneider who also edited the initial manuscript. Finally, the scientific computing team of the Leibniz University of Hannover supported the author of this thesis by helping to compile the CASTEP code and set up the required system environment at the LUIS HPC cluster system.

The article is reproduced with permission of the Royal Society of Chemistry.

## Development of high refractive index UiO-66 framework derivatives via ligand halogenation

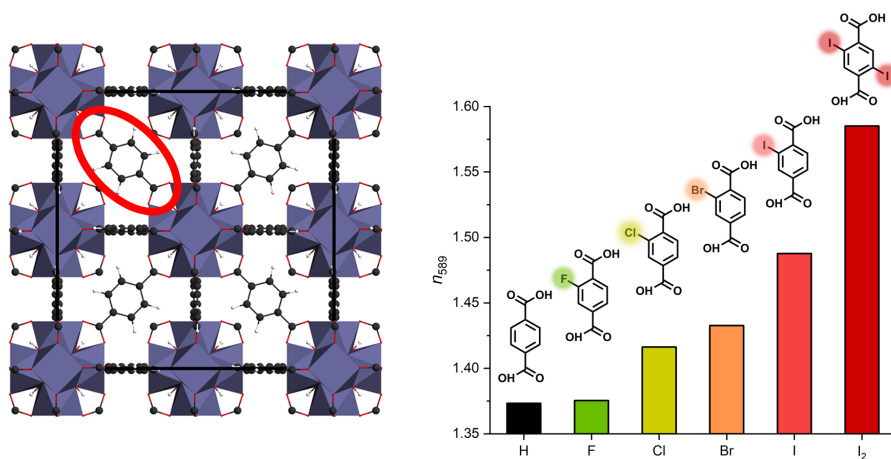
M. Treger, A. Hannebauer, P. Behrens, A. M. Schneider, *Phys. Chem. Chem. Phys.* **2023**, *25*, 15391–15399.

DOI: 10.1039/d3cp01291c

Electronic supplementary information is available at <https://doi.org/10.1039/d3cp01291c>.

### Graphical abstract

Metal-organic frameworks (MOFs) possess a modular construction. By introducing halogen atoms on the linker unit, the refractive index  $n$  of UiO-66 MOFs can be tuned over a wide range, as high-level hybrid DFT calculations show.





PCCP



PAPER



Cite this: *Phys. Chem. Chem. Phys.*,  
2023, 25, 15391

Received 22nd March 2023,  
Accepted 16th May 2023

DOI: 10.1039/d3cp01291c

rsc.li/pccp

## Development of high refractive index UiO-66 framework derivatives via ligand halogenation†‡

Marvin Treger,<sup>ab</sup> Adrian Hannebauer,<sup>a</sup> Peter Behrens<sup>ab</sup> and  
Andreas M. Schneider<sup>ab\*</sup>

UiO-66 is a Zr-based metal–organic framework (MOF) with exceptional chemical and thermal stability. The modular design of a MOF allows the tuning of its electronic and optical properties to obtain tailored materials for optical applications. Making use of the halogenation of the 1,4-benzenedicarboxylate (*bdc*) linker, the well-known monohalogenated UiO-66 derivatives were examined. In addition, a novel diiodo *bdc* based UiO-66 analogue is introduced. The novel UiO-66-I<sub>2</sub> MOF is fully characterized experimentally. By applying density functional theory (DFT), fully relaxed periodic structures of the halogenated UiO-66 derivatives are generated. Subsequently, the HSE06 hybrid DFT functional is used to calculate the electronic structures and optical properties. The obtained band gap energies are validated with UV-Vis measurements to assure a precise description of the optical properties. Finally, the calculated refractive index dispersion curves are evaluated underlining the capabilities to tailor the optical properties of MOFs by linker functionalization.

### Introduction

Metal–organic frameworks (MOFs) are a prominent class of porous organic–inorganic hybrid materials built up by inorganic building units (IBUs) connected by organic ligands acting as linkers.<sup>1,2</sup> Due to the intrinsic porosity of the frameworks, MOFs have a large potential with regard to classical applications of porous materials, like catalysis, gas separation, gas storage, or gas sensing.<sup>3–5</sup>

Apart from these traditional applications for porous materials, the use of MOFs as materials for optical applications has risen in the last years.<sup>6–9</sup> Compared to classical materials used in optics like polymers, glasses and metal oxides, the electronic and optical properties of MOFs can be tailored in a very broad range. This is due to their modular design paired with porosity allowing the deployment of different metal centers, linkers and guest molecules.<sup>10–13</sup> Additionally, optical properties of MOFs can be altered dynamically for example by reversible adsorption of guest molecules.<sup>14,15</sup> The unique modulation of the characteristics of a MOF by its design paired with the dynamically adjustable optical properties allows the development of new, highly adapted

materials for optical applications as well as the design of novel optical systems. Moreover, the design and development of an optical system itself is not only driven by the available materials and their properties but also by their processability. Here MOFs offer the advantage of low temperature preparation routes facilitating simpler and cheaper production processes of optical systems, *e.g.* via layer-by-layer synthesis, direct crystallization or spin-coating techniques.<sup>12,15,16</sup>

One of the most promising family of MOFs is formed by Zr-based frameworks. Most of these compounds feature exceptional chemical and thermal stability due to their high metal–ligand bond strength, facilitating the development of Zr-based MOFs for practical applications.<sup>17</sup> Here, we focus on the prominent Zr-based MOF UiO-66 and its halogenated derivatives. The UiO-66 framework is built up from well-known Zr<sub>6</sub>-containing IBUs formed by zirconium-oxo-hydroxo clusters (Zr<sub>6</sub>O<sub>4</sub>(OH)<sub>4</sub>) which are 12-fold coordinated by 1,4-benzenedicarboxylate (*bdc*) linkers leading to an expanded cubic closed-packed structure.<sup>18</sup> The use of monohalogenated *bdc* linkers results in the halogenated UiO-66 derivatives denoted as UiO-66-F, UiO-66-Cl, UiO-66-Br and UiO-66-I sharing the UiO-66 topology and exhibiting a high chemical and thermal stability as well.<sup>19–22</sup> These halogenated derivatives are isostructural to UiO-66, but show differences in the porosity and chemical nature of the pores, as well as different electronic and optical properties.<sup>23–25</sup>

While optical properties of MOFs in terms of the absorption and emission of light and nonlinear effects have been focused in several studies, the refractive index (RI) as a basic optical property has only recently gathered increasing attention.<sup>6,12,15</sup>

<sup>a</sup> Institute of Inorganic Chemistry, Leibniz University Hannover, Hannover, 30167, Germany. E-mail: andreas.schneider@acb.uni-hannover.de

<sup>b</sup> Cluster of Excellence PhoenixD (Photonics, Optics, and Engineering – Innovation Across Disciplines), Hannover, Germany

† Dedicated to the memory of Professor Peter Behrens.

‡ Electronic supplementary information (ESI) available: Synthesis procedures, argon sorption isotherm, TG analysis, NMR analysis, UV-Vis spectra, details of DFT calculations. See DOI: <https://doi.org/10.1039/d3cp01291c>

In addition, studies aiming on the evaluation and modulation of the RI of MOFs are rare, but changes of the RI due to external stimuli have been used as sensor signal in many applications.<sup>26</sup> However, knowledge of the RI is of importance for optical elements and systems like filters, mirrors, antireflective coatings, and wave guides, and some of these applications require high or low RI values or a combination of both.<sup>27–30</sup>

In a previous study, we explored the options of modulating the RI of UiO-66 type MOFs by linker functionalization to obtain materials with distinct optical properties having with the same topology and without changing the synthesis protocol.<sup>31</sup> These materials feature novel *bdc* linker-based push-pull motifs and were suited for near IR applications due to the absorption of light in the visible range. Here, we focus not only on the modulation of the RI, but also on the design of materials with a broad range of transparency, especially in the visible range to widen up the field of possible applications. Hence, we employ established halogenated versions of the terephthalate linker containing a single halogen atom and a novel dihalogenated linker depicted in Fig. 1. Aiming for high RI values, we do not examine the established dihalogenated UiO-66 derivatives but present a novel *bdc*-I<sub>2</sub>-based UiO-66 derivative.<sup>32</sup> The introduction of halogen atoms into the *bdc* linker increases the polarizability and allows to modulate the band gap of the resulting MOF leading to tailored optical properties. To understand these effects on the electronic structure and optical properties, we characterize the halogenated UiO-66 derivatives by applying density functional theory (DFT). In a first step different exchange–correlation functionals and dispersion corrections within the (*meta*) generalised gradient approximation (GGA, *m*GGA) are assessed to obtain adequate structural descriptions of the UiO-66 analogues. Subsequently, we use the range-separated hybrid functional HSE06 to determine both, the electronic structure and optical properties of the fully relaxed UiO-66 structure and its halogenated derivatives with high accuracy.<sup>33–36</sup> By using carefully converged plane-wave basis sets and fully relaxed models we follow our previously published strategy to ensure a precise characterization.<sup>31</sup>

In addition to the computational studies, we report the synthesis of a novel dihalogenated UiO-66 derivative featuring a linker with two iodine atoms (2,5-diiodo-1,4-dicarboxylate) extending the series of experimentally accessible dihalogenated UiO-66 derivatives.<sup>32</sup> We fully characterized this novel MOF which is only the second framework containing this terephthalate linker with two iodine atoms in *para* position.<sup>37</sup> Furthermore, we determined the band gaps of all materials *via* UV-Vis diffuse reflectance spectroscopy (UV-Vis DRS) and compared them with the theoretical values.

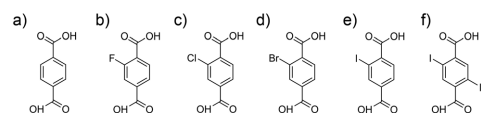


Fig. 1 UiO-66 linker molecules with (a) no functionalization, (b) fluoro, (c) chloro, (d) bromo, (e) iodo and (f) novel diiodo functionalization.

## Materials and methods

### Experimental details

UiO-66 was synthesized according to the synthetic route of Shearer *et al.*<sup>38</sup> All five UiO-66 derivatives reported were synthesized each in a 100 mL Pyrex glass vessel by dissolving specific amounts of ZrCl<sub>4</sub>, water, formic acid and linker successively in DMF. The detailed synthesis procedure and amounts are given in ESI,† Section 1. The glass vessels were sealed and heated at 120 °C for 24 h. After cooling to room temperature, the precipitate was separated *via* centrifugation, washed once with DMF and twice with acetone and dried under vacuum overnight. For purification, the obtained powder materials were Soxhlet-extracted with acetone for 24 h and activated at 120 °C under vacuum.

Powder X-Ray diffraction (PXRD) was carried out in transmission mode using a Stoe Stadi-P diffractometer operated with Ge(111)-monochromatized CuKα<sub>1</sub> radiation ( $\lambda = 1.54060 \text{ \AA}$ ). A Mythen 1 K detector was used and the diffractograms were recorded from 5 to 50° 2 $\theta$ . UV-Vis DRS was performed on MOF powders using a Praying Mantis device on a Cary 4000 from Agilent Technologies. For this purpose, the MOF powder was mortared with BaSO<sub>4</sub> to gain better quality measurements. For further characterization, digested MOF samples were analyzed *via* liquid <sup>1</sup>H-NMR spectroscopy. Therefore, two different digestion methods were necessary depending on the functionalization of the linker. For UiO-66-F and UiO-66-Cl, 15 mg of MOF were dispersed in 800  $\mu$ L of DMSO-D<sub>6</sub>, 15  $\mu$ L of HF (40%) were added and the mixture was stirred overnight. After complete dissolution of the MOFs, small amounts of calcium chloride dihydrate were added to react with excess HF. Afterwards the suspension was decanted. All other MOF samples were digested according to the procedure of Chu *et al.*<sup>39</sup> For this purpose, 15 mg of MOF were digested in 1 M (NH<sub>4</sub>)<sub>2</sub>CO<sub>3</sub> solution in D<sub>2</sub>O for 2 h. <sup>1</sup>H NMR spectra were recorded on a Bruker Ascend 400 MHz Spectrometer. Argon physisorption measurements were performed at 87 K on a Micromeritics 3Flex instrument. The samples (25 mg) were activated at 120 °C under secondary vacuum for 20 h. For the analysis of the data the associated software was used. BET areas were determined by the BET-auto function of the software and total pore volumes were calculated with single-point method at a relative pressure of 0.90. Scanning electron microscope (SEM) images were recorded with a JEOL JSM-6700F microscope using an accelerating voltage of 2 kV with a working distance of 3 mm. SEM samples were prepared by dispersion of small amounts of MOF powder in ethanol using an ultrasonic bath. The dispersion was dropped onto a polished graphite block and dried at room temperature. Thermogravimetric measurements were performed on a Netzsch STA 449 F5 Jupiter in synthetic air (N<sub>2</sub>, O<sub>2</sub>) with a heating rate of 5 K min<sup>-1</sup> using 10 mg of MOF powder.

### Computational details

All Kohn–Sham density functional theory calculations in this study were executed with the CASTEP code (version 20.1) which uses a plane-wave basis set and pseudopotentials.<sup>40,41</sup> The

### 3.2 Development of high refractive index UiO-66 framework derivatives via ligand halogenation

PCCP

Paper

unmodified UiO-66 and its halogenated derivatives were modelled with primitive cells of the fcc lattice containing 114 atoms. The convergence of the plane-wave kinetic energy cutoff and the Brillouin zone sampling were determined by the change in lattice parameters of the primitive cells (see ESI,† Section 2) and set to 1000 eV for UiO-66 and 700 eV for the derivatives with  $\Gamma$ -point sampling. The pseudopotentials were generated on-the-fly with the Koelling–Harmon method to incorporate relativistic effects into the generated pseudopotentials.<sup>42</sup> To obtain the adequate basis set size and Brillouin zone sampling, all cells were fully relaxed employing the PBEsol exchange–correlation functional and “on-the-fly” generated ultra-soft pseudopotentials with an SCF convergence criterion of  $5.0 \times 10^{-7}$  eV per atom.<sup>43</sup> The implemented low-memory Broyden–Fletcher–Goldfarb–Shanno (LBFGS) algorithm was used to generate structures with an energy change of less than  $5.0 \times 10^{-6}$  eV per atom and a maximal force of  $0.01 \text{ eV \AA}^{-1}$  with the convergence threshold of the stress and maximal atom displacement set to 0.02 GPa and  $5.0 \times 10^{-4} \text{ \AA}$ , respectively.

The basis set parameters obtained in the first step were used to assess different exchange–correlation (XC) functionals with regard to the lattice parameters of UiO-66 and its halogenated analogues in comparison with the experimental ones to generate precise structural models for further characterisation. Relying on the XC functional benchmark of our previous study, full cell relaxations were performed using the PBE expansion for solids (PBEsol) as well as its dispersion corrected form (PBEsol-TS) and the rSCAN *meta*-GGA functional.<sup>31,44,45</sup>

Subsequently, the best models of each benchmark were used to perform single point HSE06 hybrid DFT calculations to obtain accurate band structures, density of states (DOS) and the dispersion of the RI. All hybrid DFT calculations were carried out using  $\Gamma$ -point Brillouin zone sampling with the plane-wave kinetic energy cutoff values determined in the initial step of our simulation approach and a SCF convergence criterion of  $10^{-9}$  eV per atom. In a final step, the optical properties were assessed by applying the tools provided with the CASTEP code to evaluate the electronic structure, calculate the complex dielectric function and subsequently the dispersion of the index of refraction.<sup>46</sup>

## Results and discussion

This study deals with the electronic and optical properties of halogenated UiO-66-type MOFs containing the linker molecules shown in Fig. 1. Of these, UiO-66 as well as its monohalogenated derivatives are well-known. Additionally, we have synthesized a novel compound, UiO-66-I<sub>2</sub> which is built by the terephthalate linker with two iodine atoms in *para* position. At first, we discuss the characterization of the synthesized MOFs. Afterwards, we focus on the results of the calculated electronic and optical properties of the MOFs in a second part.

### Experimental studies on halogenated UiO-66-type MOFs

The synthesis of the UiO-66 derivatives was carried out using the modulation approach with formic acid in DMF, which was

introduced for the Zr-MOFs by our group.<sup>47</sup> By using this approach, the well-known halogenated UiO-66 derivatives, as well as the novel UiO-66-I<sub>2</sub>, were obtained with a high crystallinity as proven by the PXRD measurements depicted in Fig. 2. UV-Vis DRS measurements show that UiO-66 and its derivatives only exhibit absorption in the UV region. UiO-66 shows a single absorption maximum with a small shoulder at higher wavelengths, whereas its derivatives feature two distinct adsorption maxima with a second one at a higher wavelength each. The splitting of the absorption maximum is caused by the halogen atoms introduced into the framework (Fig. 2 right). This second adsorption maximum shifts to higher wavelengths with increasing polarizability of the halogen atoms (from fluorine to iodine). Therefore, the novel UiO-66-I<sub>2</sub> exhibits the largest shift of this maximum. The successful incorporation of the linker molecules into the framework and the complete removal of solvents during work-up were verified with <sup>1</sup>H-NMR-spectroscopy on digested samples (see ESI,† Fig. S4). In addition, the configuration of the 2,5-diiodo-1,4-dibenzoic acid linker molecule was verified with <sup>13</sup>C-NMR-spectroscopy (see ESI,† Section 1 and Fig. S5). The recorded spectra substantiate that the phase-pure samples were solvent-free and that the linker molecules are not altered during solvothermal synthesis. Furthermore, the spectra of all derivatives show the incorporation of modulator molecules (formic acid) in the frameworks indicating missing linker defects.

Further analysis *via* argon physisorption measurements on the novel UiO-66-I<sub>2</sub> reveals the intact porosity of this framework after solvent exchange and activation (see ESI,† Fig. S1). A typical type I isotherm, characteristic for microporous materials like UiO-66 derivatives, was obtained, with a BET-surface area of roughly  $500 \text{ m}^2 \text{ g}^{-1}$  and a pore volume of  $0.23 \text{ cm}^3 \text{ g}^{-1}$ . SEM images of UiO-66-I<sub>2</sub> show that the MOF crystallized in individual particles with a size below 100 nm (see ESI,† Fig. S2). From thermogravimetric analysis the thermal stability was found to be at a high temperature of 400 °C (see ESI,† Fig. S3).

### Structure of UiO-66 and its halogenated analogues

The DFT study presented is based on the generation of accurate structural models with precise representation of the experimental

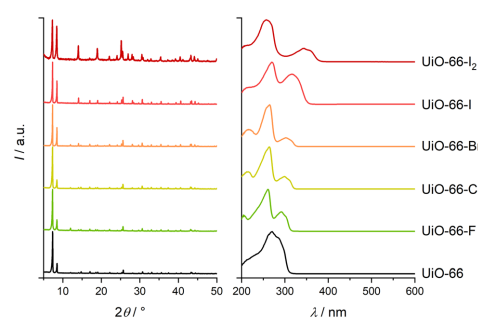


Fig. 2 PXRD patterns (left) and UV-Vis spectra (right) of UiO-66 and its mono- and dihalogenated derivatives.

### 3 Results and discussion

Paper

lattice parameters. The cubic phase of UiO-66 crystallizes in space group  $F\bar{4}3m$  with an experimental lattice parameter of  $a = 20.747 \text{ \AA}$  and contains four primitive triclinic cells ( $a_p = 14.668 \text{ \AA}$ ).<sup>48</sup> The monohalogenated UiO-66 derivatives and the novel diiodo derivative are isostructural with the parent UiO-66 and have closely matching lattice parameters as shown in the PXRD patterns (see Fig. 2). Hence, the lattice parameters of the fully relaxed cells of all derivatives were compared with the experimental ones of pristine UiO-66 to assess suitable XC functionals to obtain structural models (see ESI,† Section 3). In contrast to the unmodified UiO-66, all models of the halogenated derivatives have a reduced symmetry (space group  $R\bar{3}$ ), but share the primitive cell of UiO-66. The comparison of the lattice parameter  $a_p$  of all UiO-66 type MOF models with the experimental value of UiO-66 resulted for all XC functionals in an error of less than 0.5%. The smallest error of 0.05% for the fully relaxed UiO-66 cell was observed with the rSCAN functional. In the case of all monohalogenated UiO-66 analogues, the use of the PBEsol-TS functional yielded models with an error of less than 0.1% in the lattice parameter  $a_p$ , while the PBEsol and rSCAN functional led to comparable results with errors larger than 0.3% (see ESI,† Table S1). The benchmark with the novel UiO-66-I<sub>2</sub> shows a different outcome, all functionals lead to structures with an error above 0.1%. The models generated with the PBEsol and PBEsol-TS functional indicate the steric demand of the two iodine atoms of the linker leading to a slight widening of the structure. The smallest error is achieved by choosing the rSCAN functional leading to a slight underestimation of the lattice parameter with an error of 0.13%. In total, a model with an error in the lattice parameter of approximately a tenth of a percent for all investigated UiO-66 type MOFs was generated (see ESI,† Table S1). This confirms the experimental PXRD study and underlines the robustness of the UiO-66 topology regarding the introduction of functional groups to the linker. Furthermore, the results of this benchmark show, that a decent basis set size is required to obtain a precise structural description of the MOFs and to predict the lattice parameters of novel MOFs.

#### Electronic structure of UiO-66 and its halogenated analogues

It is well known, that the electronic structure of UiO-66 is altered by the use of functionalized linkers. The functionalization can be used to tune the band gap of the resulting materials and thus the optical properties of the UiO-66 derivatives.<sup>25,31,49,50</sup> This section deals with a detailed discussion of the electronic structures of the halogenated UiO-66 derivatives in order to understand the effects of the different halogenated linkers on the resulting MOFs.

On the basis of the fully relaxed structures, the electronic structures of UiO-66 and its halogenated derivatives were calculated employing the HSE06 hybrid DFT functional (see ESI,† Section 5). In a first step, we compared the calculated band gaps of UiO-66 with experimental values (see ESI,† Fig. S6 and Table S2) to validate the electronic structure calculations shown in Fig. 3. The band gap energies obtained from DFT calculations follow the trend of the measured ones and reproduce the experimental values in very good agreement. Furthermore, the theoretical band gap values of the monohalogenated

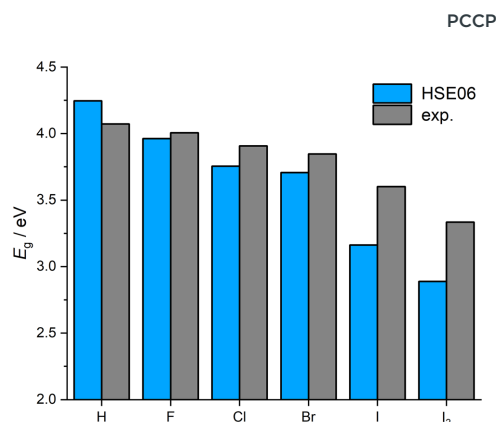


Fig. 3 Comparison of the calculated (HSE06) band gaps of UiO-66 and its halogenated derivatives with experimental (exp.) values.

UiO-66 analogues are consistent with the HSE06 values reported by Ni *et al.*<sup>25</sup> The comparison of the band gaps in Fig. 3 reveals that the experimental values of both iodo-based derivatives have an unexpected deviation of about 0.5 eV from the calculated values. A possible explanation for this discrepancy might be the fact, that the theoretical band gaps were calculated with ideal defect-free crystal structures, whereas the prepared samples might contain a larger numbers of missing linker defects due to the higher steric demand of the iodine-based linkers. The missing linker defects are compensated by the incorporation of modulator molecules into the framework, which is visible in the ESI,† Fig. S4 by the presence of formic acid. The effect of defects in UiO-66 on its electronic structure was already studied by Svane *et al.*<sup>51</sup> Moreover, the evaluation of band gaps of MOFs with UV-Vis DRS has some uncertainty, which can be seen in the values given for UiO-66-type MOFs in the literature.<sup>31,50,52</sup> Additionally, the switching of light sources in region between 300 and 375 nm introduces a possible error to the spectra of UiO-66-I and UiO-66-I<sub>2</sub> and the corresponding Tauc plots (see ESI,† Fig. S6). All in all, the trend of the calculated band gaps is in very good agreement with the experimental values.

The comparison of the band gaps in Fig. 3 shows clearly that the halogenation of the UiO-66 linker leads to a lowering of the band gap. This effect increases with the installation of heavier halogens and can be enhanced with the use of dihalogenated linkers. The following analysis of the calculated band structures, corresponding density of states (DOS) and projected density of states (PDOS) allows a deeper understanding.

In general, flat bands with almost no dispersion are typically observed for extended systems like MOFs. Starting with the band structure of UiO-66-F the effect of a halogenated linker is readily traceable. The density of states of the pristine UiO-66 shows a single maximum at the valence band maximum (VBM) which is mainly formed by the delocalized electrons of the aromatic system of the linker (see Fig. 4 and ESI,† Fig. S19). These VBM states are divided into two maxima in the case of the UiO-66-F. The VBM of the fluorinated UiO-66 is formed by

### 3.2 Development of high refractive index UiO-66 framework derivatives via ligand halogenation

PCCP

Paper

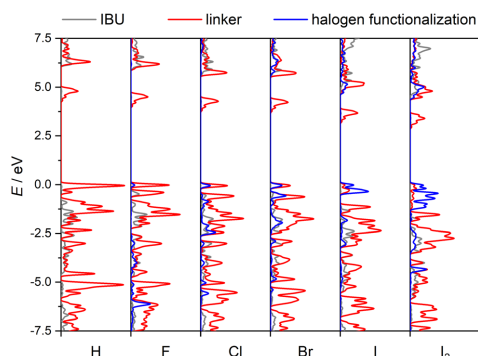


Fig. 4 PDOS of UiO-66, its monohalogenated derivatives and the novel compound UiO-66-I<sub>2</sub>.

the free electrons of the fluorine atoms and delocalized electrons of the aromatic system depicted in Fig. 5. The second maximum at the VBM also consists of  $\pi$ -electrons of the aromatic system and free electrons of both, oxygen atoms at the carboxylate group of the linker as well as oxygen atoms incorporated into the IBU. The projected electron densities of both maxima are shown in Fig. 5(a) and (b). Simultaneously, the conduction band minimum (CBM) stays the same compared to the pristine UiO-66. These features are observed for every monohalogenated UiO-66 derivative. The p-electrons of the fluorine atoms are strongly bound leading only to a small number of associated states at the VBM. The effect by the fluorination of the linker is rather small on the parent UiO-66 band gap, which is only lowered by about 0.3 eV. For the same reason no significant changes in the polarizability of the UiO-66-F compared to the UiO-66 are expected, which in consequence will result in a comparable RI of the UiO-66-F compared to the pristine UiO-66.

The splitting of the VBM states observed for UiO-66-F increases for UiO-66-Cl (see Fig. 4 and ESI,† Fig. S21) and is caused by the weaker bound valence electrons of the chlorine atom. This leads to a further narrowing of the band gap. Additionally, the higher number of p-electrons of the chlorine atom leads to the formation of states at the second maximum at

the VBM and more states at the low-energy region of the valence band (VB) resulting in a system with higher polarizability. The red shift of the band gap due to the larger splitting of the VBM states and the increased polarizability will finally lead to a higher RI in the visible region compared to the unmodified UiO-66 as shown below.

The introduction of bromine atoms leads only to a slightly smaller band gap compared to UiO-66-Cl ( $\Delta E_g = 0.05$  eV). Again, the CBM stays unchanged and compared to UiO-66-Cl the VBM states do not change notably as well. The splitting of states at the VBM does only increase slightly compared to the UiO-66-Cl, but the second maximum at the VBM is in turn more pronounced because of the weaker bound and larger number of p-electrons of the bromine atoms (see Fig. 4 and ESI,† Fig. S22). The higher number of states at the top of the VB results in an increased polarizability of the UiO-66-Br promoting also a higher RI in the visible region compared to the chloro analogue.

In contrast to the halogen derivatives already discussed, the VBM of the UiO-66-I shows more distinct features than two isolated maxima. The increased delocalization of the p-electrons of the iodine atoms results in a reduced energy of the corresponding states leading to a decomposition of the DOS maximum at the VBM into two maxima. These new VBM states are dominated by states of the iodine atoms (see Fig. 4 and 6). The analysis of the projected electron densities of these two DOS maxima at the VBM reveals that the splitting of the parent VBM states is caused by the two different orientations of the non-bonding p-orbitals of the iodine atom. The first maximum of those states at the VBM is mainly formed by the electrons of the p-orbitals of the iodine atom orientated perpendicular to the phenyl group of the *bdc* linker allowing a larger delocalization of the electrons *via* conjugation with the aromatic system (see Fig. 6a). The second maximum at the VBM of UiO-66-I is mainly formed by the electrons of the p-orbitals of the iodine atoms which are orientated parallel to the phenyl group of the *bdc* linker preventing a conjugation with the aromatic system and leading to more localized states with an higher energy (see Fig. 6b). Furthermore, the initial splitting of the VBM states into two isolated maxima observed at the monohalogenated UiO-66 analogues increases further leading to a notable reduction of the band gap compared to the UiO-66-Br of about 0.55 eV. In contrast to the other monohalogenated UiO-66 derivatives, the second maximum of the splitted VBM states of UiO-66-I is

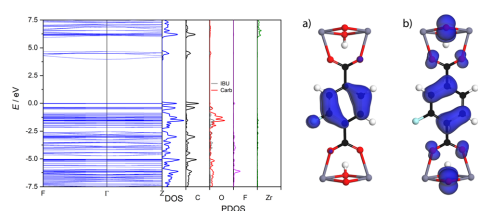


Fig. 5 Band structure, DOS and PDOS of UiO-66-F and projected electron densities of (a) the first and (b) the second DOS maximum of the VBM (isosurface value  $0.04 \text{ e} \text{ \AA}^{-3}$ ).

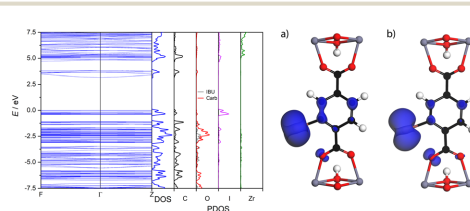


Fig. 6 Band structure, DOS and PDOS of UiO-66-I and projected electron densities of (a) the first and (b) the second DOS maximum at the VBM (isosurface value  $0.04 \text{ e} \text{ \AA}^{-3}$ ).

located at about  $-1$  eV. This maximum is formed mainly by states of the aromatic system. The delocalized states of the halogen atoms are now located at the VBM because of the diffuse character of the p-electrons of the iodine atom. The large number of delocalized states at the VBM leads to a system with high polarizability. Additionally, the band gap is diminished further resulting in a material with a high RI.

The introduction of a second iodine atom to the iodo *bdc* linker leads to the novel MOF UiO-66-I<sub>2</sub> whose band gap is about 0.3 eV smaller compared to the UiO-66-I. In contrast to the discussed electronic structures of the monohalogenated UiO-66 analogues no splitting of the states at the VBM can be observed (see Fig. 4 and ESI,† Fig. S24). In case of the diiodo UiO-66 derivative, the introduction of the large number of delocalized p-electrons by the iodine atoms leads to a domination of those at the top of the VB, the splitting of states at the VBM vanish. The electrons of the aromatic system of the *bdc* linker are still located at about  $-1$  eV. A detailed analysis of the iodine atom states at the top of the VB reveals the occurrence of a fine splitting. Here, the first two maxima of the UiO-66-I VBM are still present, but each of those parent maxima shows two new maxima. Comparable to UiO-66-I the first group of two maxima at the VBM originates from p-orbitals of the iodine atoms that are perpendicular to the benzene ring of the linker and are delocalized due to conjugation. The second set of maxima belongs to p-orbitals of the iodine atoms that are parallel orientated to the aromatic system of the linker. The observed fine splitting at the VBM states of UiO-66-I<sub>2</sub> is caused by different linker orientations. The first maximum of each pair of maxima belongs to linker that show no rotation and are parallel orientated to the plane of the corresponding carboxylate groups. The second maximum of those pairs belongs to linker molecules that are rotated out of the plane of the corresponding carboxylate groups. This different linker orientations are observed due to the steric demand of the two iodine atoms per linker preventing a simultaneous in-plane orientation of all linker molecules. Furthermore, the underlying UiO-66-I<sub>2</sub> model possess two groups

of symmetry equivalent linkers leading to the observation of only two distinct linker orientations. Thus, the fine splitting of the VBM states is only an artifact and has no relevant influence on the electronic structure and the resulting optical properties. The fine splitting of VBM states will vanish for a dynamic model without symmetry constraints featuring a broad range of different linker orientations. Finally, the large amount of states introduced to the VBM combined with the further reduced band gap result in a highly polarizable system and thus the resulting UiO-66-I<sub>2</sub> shows further tuned optical properties. This underlines the tuneability of the optical properties of the monohalogenated UiO-66 frameworks by the introduction of a second halogen atom to the linker.

#### Optical properties of UiO-66 and its halogenated analogues

Applying the HSE06 hybrid DFT functional we calculated the dielectric function and subsequently the complex refractive index of UiO-66 and its mono- and dihalogenated derivatives. The dispersion curves of the refractive indices (RI) in the visible range and the values at the sodium D-line (589 nm) of the investigated UiO-66 analogues are shown in Fig. 7. The impressively wide range of RI values covered with the halogenated UiO-66 derivatives shows clearly the potential of MOFs as optical materials and highlights the linker functionalization as versatile method to tune the optical properties of MOFs within a given framework topology.

The RI of UiO-66 and its monohalogenated derivatives show the typical normal dispersion of optical materials in the visible range due to the absorption of UV light. The RI dispersion of UiO-66 and UiO-66-F are almost identical in the visible region (1.37 and 1.38 at 589 nm) but differ towards the UV region. On the one hand this is caused by the comparable polarizabilities of the *bdc* and *bdc*-F linkers resulting in similar values for the static refractive index. On the other hand, the UiO-66-F has a reduced band gap compared with UiO-66 leading to a red shift of the absorption maximum and thus of a red shift of the maximum of the RI. This shift leads to differences of the RI of UiO-66 and UiO-66-F in the blue light and UV region, in which

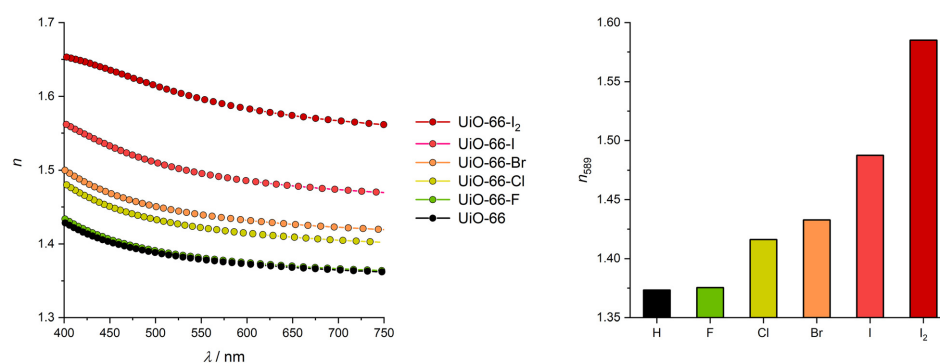


Fig. 7 Calculated refractive index of UiO-66 and its mono- and dihalogenated derivatives: dispersion curves of the refractive index (left) and values at the sodium D-line (589 nm) (right).

## 3.2 Development of high refractive index UiO-66 framework derivatives via ligand halogenation

PCCP

Paper

the UiO-66-F has higher RI values. The similarity of the RI values of UiO-66 and its fluoro analogue were also reported by Ni *et al.* with values of 1.476 and 1.484, respectively.<sup>25</sup> The discrepancy in absolute values is caused by the calculation method by Ni *et al.*, who used a combination of the PBE GGA functional and a scissors operator to correct the underestimation of the band gap by the PBE functional. This approach might be suitable to determine trends in the RI, but lacks a precise description of the optical properties. To obtain a precise description of the optical properties further corrections are required to satisfy the sum rule, since the sole use of the scissors operator leads to overestimated amplitudes in the dielectric function resulting in higher values of the RI.<sup>36</sup>

In contrast to the UiO-66-F, the introduction of a chlorine or bromine atom leads to a remarkable increase of the RI (see Fig. 7). Both materials, UiO-66-Cl as well as UiO-66-Br show reduced band gaps compared to the UiO-66-F and higher electron densities at the VBM. This results in systems with a red shifted maximum of the RI and higher polarizability promoting higher RI values in the visible region of the light. The RI of the chloro and bromo derivatives are 1.42 and 1.43 at 589 nm, respectively, corresponding to an increase of the RI compared to the parent UiO-66 of about 0.04 due to the chloro functionalization. Substitution of the chlorine atoms with bromine atoms leads to a further increase of about 0.02 in the RI. These raises of the RI are consistent with the values of Ni *et al.*, whereas the absolute values differ as pointed out before.<sup>25</sup> The increase of the RI due to the incorporation of chlorine atoms instead of fluorine atoms is twice times higher than the effect of the substitution of the chlorine atoms with bromine atoms. This can be ascribed to two factors. First the introduction of chlorine instead of fluorine atoms is followed by a large increase of the electron density at the VBM while the substitution of chlorine with bromine atoms has less effect on the VBM states, since the new states are not located directly at the VBM. Second, the redshift of the band gap energy by the chlorine substitution is four times larger compared to the red shift caused by the bromo substitution, resulting in similar RI values for UiO-66-Cl and UiO-66-Br.

The substitution of the bromine with iodine atoms allows a further tuning of the RI. UiO-66-I shows a RI of 1.49 at 589 nm corresponding to an increase of about 0.05 compared to UiO-66-Br being in line with the reported increment of Ni *et al.*<sup>25</sup> This relatively large increase in the RI is caused by the large polarizability of the iodo functionalized linker which is a result of the large number of delocalized iodine states at the VBM coupled with an additional decrease of the band gap. The band gap of the UiO-66-I is close to the visible range of the light, shifting the maximum of the RI analogously towards the visible range causing high RI values.

The introduction of a second iodine atom to the *bdc*-I linker results in the UiO-66-I<sub>2</sub> MOF featuring a linker with a large polarizability. This leads to an even larger RI value of 1.59 at 589 nm which is an increase of the RI of UiO-66-I of 0.1 and opens up the field for advanced optical systems requiring a large modulation of the RI. The application of the UiO-66-I<sub>2</sub> is

only limited by its absorption of blue light visible as a plateau in the dispersion of the RI. This absorption at the edge of the visible range is caused by the band gap reduction due to the introduction of a second iodine atom to the linker, although this red shift of the band gap next to the large density of states at the VBM enables the large RI values of this material.

Overall, the functionalization of UiO-66 by halogenation of the *bdc* linker leads to promising derivatives for optical applications sharing the high chemical stability of the parent material. While UiO-66-F shows only differences of the RI in the UV region, all other mono- and dihalogenated UiO-66 analogues described above allow a broad range tuning of the RI in the visible light within a single crystal topology. Furthermore, the halogenation of the *bdc* linker not only leads to UiO-66 type MOFs with a broad range of RI, but additionally preserves the porosity of the framework resulting in versatile materials for optical applications. This allows the use of these materials for example in the construction of optical filters of coating as well as optical gas sensors due to their porosity *e.g.* by the coating of waveguides. Finally, this study makes reliable RI values for UiO-66 and its derivatives available. In 2018, Hunag *et al.* published a first attempt to characterize the RI of UiO-66, but the used films were not of optical quality and the complete removal of solvents out of the porosity was not monitored.<sup>53</sup> Here, with the presented optical properties in this study the development and calculation of optical systems incorporating UiO-66 materials is facilitated.

## Conclusions

The functionalization of the Zr-based UiO-66 MOF *via* halogenation of the *bdc* linker was studied. The resulting mono-halogenated derivatives as well as a novel diiodo derivative were characterized *via* their electronic structures and the resulting optical properties. For this purpose, we applied our previously established simulation approach featuring the HSE06 hybrid DFT functional. Furthermore, we report the successful synthesis and characterization of the novel UiO-66-I<sub>2</sub> MOF which contains a *bdc* linker with two iodine atoms in *para* position.

Deploying accurate converged plane-wave basis sets with respect to the total energy and the lattice parameters of the systems, fully relaxed periodic models were generated by assessing different XC functionals to obtain precise representations of the investigated materials. All halogenated derivatives are found to be isostructural and have comparable lattice parameters underlining the versatile and modular design of MOFs. Subsequently, electronic structure calculations were performed and the obtained band gap energies were validated with UV-Vis DRS measurements. The closely matching experimental and theoretical band gaps ensure a reliable calculation of the refractive index in the next step. The use of halogenated linkers leads to a series of decreasing band gaps with increasing size of the halogen atom which can be enhanced by introducing two halogen atoms to a single linker. To gain a deeper understanding of the electronic structure, the materials were

analyzed *via* PDOS revealing that the halogenation of the *bdc* linker leads to a splitting of the VBM states. The electron density in this region increases with the introduction of heavier halogen atoms leading to higher polarizabilities. Afterwards the dispersion curves of the RI were calculated at hybrid DFT level. The differences in the RI of the different derivatives were characterized and reduced to the reduction of the band gap energies and introduction of more delocalized states at the VBM due to the incorporation of more diffuse halogen atoms.

Overall, this work underlines the potential of MOFs as optical materials offering a broad range of accessible refractive indices. The halogenation of linkers was proven to be a simple but effective method to exploit the modular design of MOFs to obtain materials with tailored optical properties. This allows the use of MOFs in several optical systems like filters requiring high and low refracting materials in a single design. Especially in systems with layered designs MOFs have great potential offering different RI values within a single topology and synthesis protocol. Furthermore, the halogenation of the linkers preserves the porosity of the framework enabling the incorporation of guest molecules to further tune the RI or perform sensing. Additionally, the halogenated derivatives are transparent in the visible range of the light and some of them even enable applications in the UV region widening up the field of possible applications.

### Conflicts of interest

There are no conflicts to declare.

### Acknowledgements

We acknowledge the support of the cluster system team at the Leibniz University of Hannover, Germany in the production of this work. This work is funded by the DFG under Germany's Excellence Strategy within the Cluster of Excellence PhoenixD (EXC 2122, Project ID 390833453). A. H. is grateful for being funded by the Hannover School for Nanotechnology (HSN) at the Laboratory of Nano and Quantum Engineering (LNQE). The HSN is funded by the Ministry of Science and Culture of Lower Saxony.

### Notes and references

- J. L. Rowsell and O. M. Yaghi, *Microporous Mesoporous Mater.*, 2004, **73**, 3.
- S. R. Batten, N. R. Champness, X.-M. Chen, J. Garcia-Martinez, S. Kitagawa, L. Öhrström, M. O'Keeffe, M. Paik Suh and J. Reedijk, *Pure Appl. Chem.*, 2013, **85**, 710.
- L. E. Kreno, K. Leong, O. K. Farha, M. Allendorf, R. P. van Duyne and J. T. Hupp, *Chem. Rev.*, 2012, **112**, 1105.
- H. Li, K. Wang, Y. Sun, C. T. Lollar, J. Li and H.-C. Zhou, *Mater. Today*, 2018, **21**, 108.
- A. Dhakshinamoorthy, Z. Li and H. Garcia, *Chem. Soc. Rev.*, 2018, **47**, 8134.
- T. N. Nguyen, F. M. Ebrahim and K. C. Stylianou, *Coord. Chem. Rev.*, 2018, **377**, 259.
- Y. Zheng, F.-Z. Sun, X. Han, J. Xu and X.-H. Bu, *Adv. Opt. Mater.*, 2020, **8**, 2000110.
- K.-T. Hsu, P. Thanasekaran, T.-W. Hsu, C.-H. Su, B.-C. Chang, Y.-H. Liu, C.-H. Hung and K.-L. Lu, *CrystEngComm*, 2021, **23**, 824.
- H. Li, L. Zhang, H. He, Y. Yang, Y. Cui and G. Qian, *Sci. China: Mater.*, 2021, **64**, 698.
- K. Hendrickx, D. E. P. Vanpoucke, K. Leus, K. Lejaeghere, A. van Yperen-De Deyne, V. van Speybroeck, P. van der Voort and K. Hemelsoet, *Inorg. Chem.*, 2015, **54**, 10701.
- M. A. Syzgantseva, C. P. Ireland, F. M. Ebrahim, B. Smit and O. A. Syzgantseva, *J. Am. Chem. Soc.*, 2019, **141**, 6271.
- W. Yin, C.-A. Tao, F. Wang, J. Huang, T. Qu and J. Wang, *Sci. China: Mater.*, 2018, **61**, 391.
- M. D. Allendorf, M. E. Foster, F. Léonard, V. Stavila, P. L. Feng, F. P. Doty, K. Leong, E. Y. Ma, S. R. Johnston and A. A. Talin, *J. Phys. Chem. Lett.*, 2015, **6**, 1182.
- E. Redel, Z. Wang, S. Walheim, J. Liu, H. Gliemann and C. Wöll, *Appl. Phys. Lett.*, 2013, **103**, 91903.
- N. C. Keppler, K. D. J. Hindricks and P. Behrens, *RSC Adv.*, 2022, **12**, 5807.
- J. E. Ellis, S. E. Crawford and K.-J. Kim, *Mater. Adv.*, 2021, **2**, 6169.
- Y. Bai, Y. Dou, L.-H. Xie, W. Rutledge, J.-R. Li and H.-C. Zhou, *Chem. Soc. Rev.*, 2016, **45**, 2327.
- J. H. Cavka, S. Jakobsen, U. Olsbye, N. Guillou, C. Lamberti, S. Bordiga and K. P. Lillerud, *J. Am. Chem. Soc.*, 2008, **130**, 13850.
- F. Vermoortele, M. Vandichel, B. van de Voorde, R. Ameloot, M. Waroquier, V. van Speybroeck and D. E. de Vos, *Angew. Chem., Int. Ed.*, 2012, **51**, 4887.
- M. Kandiah, M. H. Nilsen, S. Usseglio, S. Jakobsen, U. Olsbye, M. Tilset, C. Larabi, E. A. Quadrelli, F. Bonino and K. P. Lillerud, *Chem. Mater.*, 2010, **22**, 6632.
- S. J. Garibay and S. M. Cohen, *Chem. Commun.*, 2010, **46**, 7700.
- S. Biswas, J. Zhang, Z. Li, Y.-Y. Liu, M. Grzywa, L. Sun, D. Volkmer and P. van der Voort, *Dalton Trans.*, 2013, **42**, 4730.
- W. Liang, R. Babarao and D. M. D'Alessandro, *Inorg. Chem.*, 2013, **52**, 12878.
- L. Shen, R. Liang, M. Luo, F. Jing and L. Wu, *Phys. Chem. Chem. Phys.*, 2015, **17**, 117.
- B. Ni, W. Sun, J. Kang and Y. Zhang, *J. Phys. Chem. C*, 2020, **124**, 11595.
- C. Zhu, R. E. Gerald and J. Huang, *IEEE Sens. J.*, 2021, **21**, 19647.
- H.-Y. Pan, X. Chen and X.-L. Xia, *Renewable Sustainable Energy Rev.*, 2022, **161**, 112361.
- A. K. Oskouei, L. A. Emmert, W. Rudolph, M. Steinecke, M. Jupé, L. O. Jensen and D. Ristau, *Optical Interference Coatings Conference (OIC)*, OSA, Washington, DC, ThB.2, 2019.
- H. K. Raut, V. A. Ganesh, A. S. Nair and S. Ramakrishna, *Energy Environ. Sci.*, 2011, **4**, 3779.



### 3.2 Development of high refractive index UiO-66 framework derivatives via ligand halogenation

- | PCCP  | Paper   |
|---|---|
| 30 Y. Kokubun, N. Funato and M. Takizawa, <i>IEEE Photon. Technol. Lett.</i> , 1993, <b>5</b> , 1297.   | 42 D. D. Koelling and B. N. Harmon, <i>J. Phys. C: Solid State Phys.</i> , 1977, <b>10</b> , 3107.  |
| 31 M. Treger, A. Hannebauer, A. Schaate, J. L. Budde, P. Behrens and A. M. Schneider, <i>Phys. Chem. Chem. Phys.</i> , 2023, <b>25</b> , 6333.                          | 43 J. P. Perdew, A. Ruzsinszky, G. I. Csonka, O. A. Vydrov, G. E. Scuseria, L. A. Constantin, X. Zhou and K. Burke, <i>Phys. Rev. Lett.</i> , 2008, <b>100</b> , 136406.                  |
| 32 S. Biswas and P. van der Voort, <i>Eur. J. Inorg. Chem.</i> , 2013, 2154.  | 44 W. A. Al-Saidi, V. K. Voora and K. D. Jordan, <i>J. Chem. Theory Comput.</i> , 2012, <b>8</b> , 1503.  |
| 33 A. V. Krukau, O. A. Vydrov, A. F. Izmaylov and G. E. Scuseria, <i>J. Chem. Phys.</i> , 2006, <b>125</b> , 224106.  | 45 A. P. Bartók and J. R. Yates, <i>J. Chem. Phys.</i> , 2019, <b>150</b> , 161101.   |
| 34 J. Paier, M. Marsman, K. Hummer, G. Kresse, I. C. Gerber and J. G. Ángyán, <i>J. Chem. Phys.</i> , 2006, <b>125</b> , 249901.  | 46 A. J. Morris, R. J. Nicholls, C. J. Pickard and J. R. Yates, <i>Comput. Phys. Commun.</i> , 2014, <b>185</b> , 1477.   |
| 35 A. J. Garza and G. E. Scuseria, <i>J. Phys. Chem. Lett.</i> , 2016, <b>7</b> , 4165.   | 47 A. Schaate, P. Roy, A. Godt, J. Lippke, F. Waltz, M. Wiebcke and P. Behrens, <i>Chem. – Eur. J.</i> , 2011, <b>17</b> , 6643.  |
| 36 M. Nishiwaki and H. Fujiwara, <i>Comput. Mater. Sci.</i> , 2020, <b>172</b> , 109315.  | 48 S. Øien, D. Wragg, H. Reinsch, S. Svelle, S. Bordiga, C. Lamberti and K. P. Lillerud, <i>Cryst. Growth Des.</i> , 2014, <b>14</b> , 5370.  |
| 37 K. Cui, J. Ma, X.-K. Huo and J.-X. Zhang, <i>Z. Naturforsch. B</i> , 2014, <b>69</b> , 859.  | 49 K. Hendrickx, D. E. P. Vanpoucke, K. Leus, K. Lejaeghere, A. van Yperen-De Deyne, V. van Speybroeck, P. van der Voort and K. Hemelsoet, <i>Inorg. Chem.</i> , 2015, <b>54</b> , 10701. |
| 38 G. C. Shearer, S. Chavan, J. Ethiraj, J. G. Vitillo, S. Svelle, U. Olsbye, C. Lamberti, S. Bordiga and K. P. Lillerud, <i>Chem. Mater.</i> , 2014, <b>26</b> , 4068. | 50 E. Flage–Larsen, A. Røyset, J. H. Cavka and K. Thorshaug, <i>J. Phys. Chem. C</i> , 2013, <b>117</b> , 20610.  |
| 39 J. Chu, F.-S. Ke, Y. Wang, X. Feng, W. Chen, X. Ai, H. Yang and Y. Cao, <i>Commun. Chem.</i> , 2020, <b>3</b> , 5.   | 51 K. L. Svane, J. K. Bristow, J. D. Gale and A. Walsh, <i>J. Mater. Chem. A</i> , 2018, <b>6</b> , 8507.   |
| 40 W. Kohn and L. J. Sham, <i>Phys. Rev.</i> , 1965, <b>140</b> , A1133–A1138.  | 52 T. Musho, J. Li and N. Wu, <i>Phys. Chem. Chem. Phys.</i> , 2014, <b>16</b> , 23646.   |
| 41 S. J. Clark, M. D. Segall, C. J. Pickard, P. J. Hasnip, M. I. J. Probert, K. Refson and M. C. Payne, <i>Z. Kristallogr.</i> , 2005, <b>220</b> , 567.                | 53 Y. Huang, C.-A. Tao, R. Chen, L. Sheng and J. Wang, <i>Nanomaterials</i> , 2018, <b>8</b> , 676.   |

### 3.3 Fragment-based approach for the efficient calculation of the refractive index of metal-organic frameworks

#### Preface

This work was published as full paper in the journal “Physical chemistry chemical physics: PCCP” of the Royal Society of Chemistry and is focused on the development of a simulation approach for the efficient calculation of the refractive index of metal-organic frameworks. The simulation approach presented in the first publication and also applied in the second publication is based on DFT methods with PBC. These calculations are computationally demanding but allow a detailed understanding of the electronic structure of MOFs and their optical properties. To identify MOFs suitable for specific optical applications or with an extraordinary high or low RI, computational screenings are required due to the large number experimental accessible MOFs. These screenings should rely on methods with reasonable computational effort to be applicable. Furthermore, the prediction of the RI of novel compounds should be straightforward to guide the materials development. In literature, different simulation protocols are presented allowing the calculation of the RI of materials at reduced computational costs. These methods were developed for molecular materials and materials consisting of one-dimensional chains. Accordingly, a novel simulation approach is presented in this work allowing to efficiently calculate the RI of MOFs. The developed method relies on a fragmentation scheme for MOFs for the decomposition of the framework into ionic (multi-atom) fragments. These fragments can be evaluated with molecular DFT calculations and the sum of their polarizabilities is used to reconstruct the polarizability of the MOF. Finally, the static RI can be calculated using the Lorenz-Lorentz equation.

In a first step of this study, XC functional benchmark calculations were performed to select a suitable functional. Subsequently, a set of 24 MOFs consisting of Zr-based MOFs, ZIFs, and one p-element-based MOF was examined using the novel fragment-based approach. The obtained RI values were validated using the established DFT method using PBC published previously. The comparison to the PBC-based approach led to an estimated maximum error of 4%. Furthermore, the calculated RI value of ZIF-8 was compared with the experimental one revealing an error below 1%. Additionally, a speed up of the calculation of the RI of up to 600 times was found. This underlines the capability of the proposed method to obtain precise RI values at remarkably reduced computational effort.

### *3.3 Fragment-based approach for the efficient calculation of the refractive index of metal-organic frameworks*

The author of this thesis developed the simulation approach presented in this work, performed all calculations and wrote the initial manuscript. Prof. Dr. Peter Behrens, Prof. Carolin König and Dr. Andreas M. Schneider guided this study. The initial manuscript was edited by Dr. Andreas M. Schneider and Prof. Carolin König. Furthermore, the scientific computing team of the Leibniz University of Hannover supported the author of this thesis by helping to compile the CASTEP code and set up the required system environment at the LUIS HPC cluster system.

The article is reproduced with permission of the Royal Society of Chemistry.

## Fragment-based approach for the efficient calculation of the refractive index of metal-organic frameworks

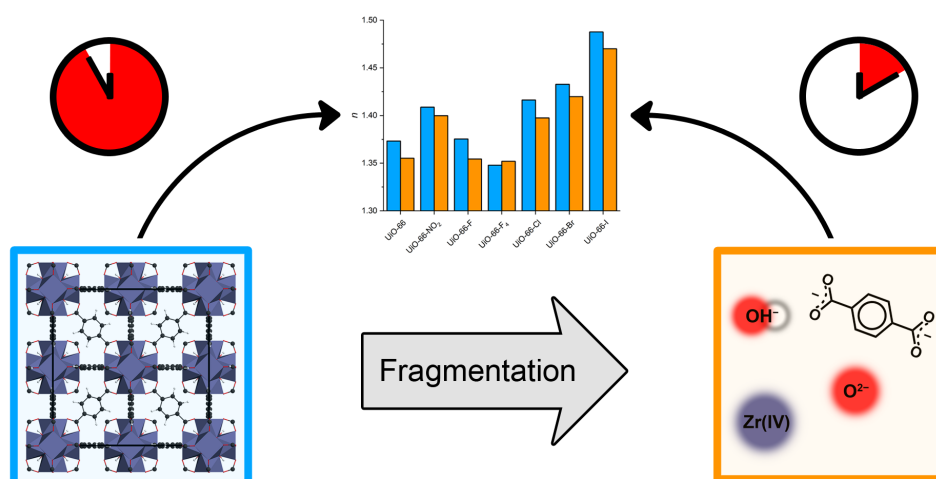
M. Treger, C. König, P. Behrens, A. M. Schneider, *Phys. Chem. Chem. Phys.* **2023**, *25*, 19013–19023.

DOI: 10.1039/d3cp02356g

Electronic supplementary information is available at <https://doi.org/10.1039/d3cp02356g>.

### Graphical abstract

Metal-organic frameworks (MOFs) possess a modular construction. By applying a fragmentation scheme the refractive index  $n$  of MOFs can be calculated in an efficient way.



PCCP



PAPER



Cite this: *Phys. Chem. Chem. Phys.*, 2023, 25, 19013

## Fragment-based approach for the efficient calculation of the refractive index of metal-organic frameworks†‡

Marvin Treger,<sup>id</sup> <sup>ab</sup> Carolin König,<sup>id</sup> <sup>bc</sup> Peter Behrens<sup>id</sup> <sup>ab</sup> and Andreas M. Schneider<sup>id</sup> <sup>\*ab</sup>

Increasing demands on materials in the field of optical applications require novel materials. Metal-organic frameworks (MOFs) are a prominent class of hybrid inorganic-organic materials with a modular layout. This allows the fine-tuning of their optical properties and the tailored design of optical systems. In the present theoretical study, an efficient method to calculate the refractive index (RI) of MOFs is introduced. For this purpose, the MOF is split into disjoint fragments, the linkers and the inorganic building units. The latter are disassembled until metal ions are obtained. The static polarizabilities are calculated individually using molecular density functional theory (DFT). From these, the MOF's RI is calculated. To obtain suitable polarizabilities, an exchange-correlation functional benchmark was performed first. Subsequently, this fragment-based approach was applied to a set of 24 MOFs including Zr-based MOFs and ZIFs. The calculated RI values were compared to the experimental values and validated using HSE06 hybrid functional DFT calculations with periodic boundary conditions. The examination of the MOF set revealed a speed up of the RI calculations by the fragment-based approach of up to 600 times with an estimated maximal deviation from the periodic DFT results below 4%.

Received 23rd May 2023,  
Accepted 30th June 2023

DOI: 10.1039/d3cp02356g

rsc.li/pccp

### Introduction

The refractive index (RI) is one of the determining optical properties when considering a material for application in optical systems. Anti-reflective coatings require materials with low RI values, whereas mirrors and filters require a combination of materials with high as well as low RI values, to name just two examples.<sup>1–3</sup> The development of high refractive index polymers (HRIPs) with full transparency in the visible spectral range is still challenging.<sup>4,5</sup>

In the last years, the use of metal-organic frameworks (MOFs) as materials for optical applications and the examination of the RI of MOFs has gathered increasing attention.<sup>6–13</sup> MOFs are a class of porous organic-inorganic hybrid materials built up by inorganic building units (IBUs) connected by organic ligands

serving as linkers.<sup>14,15</sup> This modular design and the inherent porosity allows the fine tuning of the electronic and optical properties of MOFs in a broad range by incorporating different metal centers, linkers and guest molecules.<sup>10,11,16–18</sup>

The development of novel MOF-based optical materials and systems requires precise knowledge about their optical properties with a focus on the RI. Today, more than 90 000 MOFs are experimentally accessible.<sup>19</sup> To assess suitable MOFs for possible applications from this large set, computational screenings are a convenient approach.<sup>20</sup> The precise calculation of the optical properties of MOFs requires the use of hybrid density functional theory (DFT) exchange-correlation (XC) functionals and periodic boundary conditions (PBC) making these calculations computationally demanding and time consuming.<sup>12,13,21</sup> This computational effort prevents the fast screening of MOFs regarding their RI. Thus, other methods are required to allow a fast screening of the RI of MOFs.

There are several methods reported enabling the high-throughput screening of materials and their RI for optical applications. Afzal *et al.* established an efficient protocol to calculate the RI of polymers.<sup>22,23</sup> The protocol is based on the linear correlation of the size of an oligomer and its polarizability. This correlation is used to extrapolate the polarizability of a polymer chain. Additionally, the number density is calculated *via* a machine learning model enabling the prediction of

<sup>a</sup> Institute of Inorganic Chemistry, Leibniz University Hannover, Callinstr. 9, 30167 Hannover, Germany. E-mail: andreas.schneider@acb.uni-hannover.de

<sup>b</sup> Cluster of Excellence PhoenixD (Photonics, Optics, and Engineering – Innovation Across Disciplines), Hannover, Germany

<sup>c</sup> Institute of Physical Chemistry and Electrochemistry, Leibniz University Hannover, Callinstr. 3A, 30167 Hannover, Germany

† Dedicated to the memory of Professor Peter Behrens.

‡ Electronic supplementary information (ESI) available: Details of DFT calculations, polarizabilities of the MOF fragments and calculated refractive indices. See DOI: <https://doi.org/10.1039/d3cp02356g>

### 3 Results and discussion

Paper

PCCP

the RI of a polymer. Ligorio *et al.* used a partitioning scheme provided by the quantum theory of atoms in molecules (QTAIM) to reduce the computational effort of RI calculations of crystalline molecular materials.<sup>24</sup> Therefore, calculations with molecular aggregates were carried out, followed by a partitioning of the polarizabilities to obtain the polarizability of a single interacting molecule. This allows the calculation of the RI of the molecular materials without computationally demanding fully periodic DFT calculations. Ernst *et al.* also used a partitioning scheme provided by QTAIM to calculate the RI of metal-organic networks built up by chains of amino acids and metal ions.<sup>25</sup> They used clusters of the secondary building units of this metal-organic network chains and calculated the atomic polarizabilities of the atoms of the asymmetric unit. Those polarizabilities were used to calculate the RI of the crystalline materials.

All aforementioned approaches are suitable for molecular materials or materials formed by (coordination) polymer chains and were developed for dense materials. In contrast, MOFs are built up by IBUs coordinated by linkers in two or three dimensions forming porous layers or frameworks. Using the approaches described in literature, the evaluation of extended MOF clusters is necessary to obtain a suitable representation of the interacting atoms forming the material. This translates into systems with several hundred atoms leading to the loss of the initial reduction of the computational demands by the omission of the PBC.

Here, we present a method allowing the evaluation of the RI of MOFs with substantial reduced computational effort. Our approach is based on a fragmentation scheme for MOFs combined with molecular DFT to obtain the static polarizability and RI. More precisely, the MOF is fragmented into metal ions, ligands and linkers, which static polarizabilities are calculated individually. We note that neglecting the metal-ligand bond is a substantial approximation. Furthermore, cutting this bond is often viewed with great skepticism as a fragmentation method for energy calculations.<sup>26–28</sup> However, the proposed fragmentation scheme in this work, benefits from the fact, that the polarizability and optical properties of the investigated MOFs are dominated by their linkers.<sup>10–13,17,29,30</sup> In the following step, the calculated static polarizabilities of the fragments are used to obtain the static polarizability of the corresponding MOF. Therefore, the polarizabilities of the isolated fragments are added up with respect to the composition of the MOF relying on the additivity hypothesis.<sup>31</sup> This approach is known as orientated gas model and has been successfully applied to calculate the optical properties of molecular crystals, crystalline materials and metal-organic networks.<sup>25,32,33</sup> Furthermore, the additivity of the polarizability has been used successfully to calculate the RI of minerals.<sup>34,35</sup> Finally, the polarizability of the MOF is used to estimate the corresponding RI by applying the Lorenz-Lorentz equation.<sup>36,37</sup> The use of the Lorenz-Lorentz equation to calculate the static as well as the frequency-dependent RI with polarizabilities obtained by DFT is well established and is not limited to isotropic systems.<sup>38,39</sup> In addition, using the Lorenz-Lorentz equation in combination

with polarizabilities obtained by DFT yields RIs in good agreement with experiments for gases, liquids, and materials.<sup>23,40–42</sup>

The developed fragment-based approach is validated with periodic hybrid DFT calculations based on fully relaxed MOF structures to obtain reliable electronic structures and optical properties using our previously published approach.<sup>12,13</sup> In a first step of this study, we performed a benchmark to select a suitable exchange–correlation (XC) functional for the molecular DFT calculations. Afterwards the fragment approach was tested with 24 MOFs. The selected MOFs are transparent in the near IR and visible region of the light and possess a band gap larger than 3 eV. Hence, they are suited for a broad range of optical applications.

The MOFs selected for this study (see Table 1) mainly belong to the groups of Zr-based MOFs and zeolitic imidazolate frameworks (ZIFs). Their design principles can be found in Fig. 1. The Zr-based MOFs were chosen due to their well-known high chemical and thermal stability promoting the use of this MOF family for practical applications.<sup>43</sup> As representatives of Zr-based MOF materials, UiO-66 and derivatives, MIL-140A and derivatives, *Zr-fum* MOF, and UiO-67 were chosen.<sup>44–46</sup> UiO-66 and its derivatives are very prominent Zr-based MOFs built up by the typical  $Zr_6O_4(OH)_4$  IBU coordinated by 1,4-benzenedicarboxylate (*bdc*) forming an expanded cubic closed-packed structure (see Fig. 1). These MOFs have already been considered as materials for optical applications.<sup>12,13,44,47–51</sup> Analog to the UiO-family, the *Zr-fum* MOF is based on the typical  $Zr_6$ -containing IBU and show the same topology as well, but features fumarate (*fum*) as linker leading to a denser framework.<sup>46</sup> The MIL-140A frameworks are also Zr-based MOFs built up by the *bdc* linker, but have a one-dimensional IBU leading to a different topology and higher density compared to the UiO-family MOFs.<sup>45</sup> In contrast, ZIFs are based on the topology of zeolites and are formed by imidazolate (*im*) linkers coordinating transition metal ions.<sup>52</sup> ZIFs and especially ZIF-8 have already been examined for and used in different optical applications, *e.g.* as thin films of optical quality or coatings in optical sensor systems. Hence, we also applied our fragment approach to nine different ZIFs.<sup>11,53–56</sup> ZIF-8 is one of the most prominent ZIFs consisting of zinc ions coordinated by 2-methylimidazolate (*mim*) linkers crystallizing with the SOD topology (see Fig. 1).<sup>52</sup> Besides ZIF-8, four additional zinc-based ZIFs featuring the SOD topology all built up by different imidazolate derivatives (SOD-ZIF-71, ZIF-90, ZIF-318 and SALEM-2) were assessed.<sup>57–60</sup> Furthermore, three ZIFs next to SALEM-2 consisting of the *im* linker and zinc ions (ZIF-1, ZIF-10, ZIF-64) with different topologies and densities were included.<sup>52,61</sup> In addition, ZIF-72 formed by zinc ions and 4,5-dichloroimidazolate (*dcim*) analog to SOD-ZIF-71 was also part of this study.<sup>61</sup> Apart from the Zr-based MOFs and ZIFs, the high temperature (ht) phase of the well-known Al-MIL-53 MOF (see Fig. 1) was also studied to show the transferability of our approach for non-transition metal containing MOFs.<sup>62</sup>

Finally, we compared the experimental determined RI value of ZIF-8 with the calculated value obtained by using our fragment-based approach as well as our protocol with PBC

### 3.3 Fragment-based approach for the efficient calculation of the refractive index of metal-organic frameworks

PCCP

Paper

**Table 1** Overview of all selected MOFs with their linkers, IBUs, compositions (A = IBU and B = linker) and nets (RCSR).<sup>65</sup> MIL-140A and Al-MIL-53 possess a one-dimensional IBU (\*)

	MOF	Linker	IBU	Composition	Net	
Zr-based	UiO-66	<i>bdc</i>	1,4-Benzenedicarboxylate	$[\text{Zr}_6\text{O}_4(\text{OH})_4]^{12+}$	$\text{AB}_6$	<b>fcu</b>
	UiO-66-NO <sub>2</sub>	<i>bdc</i> -NO <sub>2</sub>	2-Nitrobenzene-1,4-dicarboxylate			
	UiO-66-F	<i>bdc</i> -F	2-Fluorobenzene-1,4-dicarboxylate			
	UiO-66-F <sub>4</sub>	<i>bdc</i> -F <sub>4</sub>	2,3,5,6-Tetrafluorobenzene-1,4-dicarboxylate			
	UiO-66-Cl	<i>bdc</i> -Cl	2-Chlorobenzene-1,4-dicarboxylate			
	UiO-66-Br	<i>bdc</i> -Br	2-Bromobenzene-1,4-dicarboxylate			
	UiO-66-I	<i>bdc</i> -I	2-Iodobenzene-1,4-dicarboxylate			
	UiO-67	<i>bpdc</i>	Biphenyl-4,4'-dicarboxylate			
	Zr- <i>fum</i> MOF	<i>fum</i>	Fumarate			
	MIL-140A	<i>bdc</i>		$[\text{ZrO}]^{2+}$ *	AB	<b>bsn</b>
	MIL-140A-NO <sub>2</sub>	<i>bdc</i> -NO <sub>2</sub>				
	MIL-140A-F	<i>bdc</i> -F				
	MIL-140A-Cl	<i>bdc</i> -Cl				
MIL-140A-Br	<i>bdc</i> -Br					
ZIFs	ZIF-8	<i>mim</i>	2-Methyl-imidazolate	$\text{Zn}^{2+}$	$\text{AB}_2$	<b>sod</b>
	ZIF-318	<i>cf<sub>3</sub>mim</i>	2-Trifluoromethyl-imidazolate			
	ZIF-90	<i>lca</i>	Imidazolate-2-carboxyaldehyde			
	SOD-ZIF-71	<i>dcim</i>	4,5-Dichloroimidazolate			
	SALEM-2	<i>im</i>	Imidazolate			
	ZIF-1	<i>im</i>		$\text{Zn}^{2+}$	$\text{AB}_2$	<b>crb</b>
	ZIF-10	<i>im</i>				<b>mer</b>
	ZIF-64	<i>im</i>				<b>crb</b>
	ZIF-72	<i>dcim</i>				<b>les</b>
	Al-MIL-53 (ht)	<i>bdc</i>		$[\text{Al}(\text{OH})]^{2+}$ *	AB	<b>bpq</b>

calculations to highlight the adequacy of the present fragment-based approach.

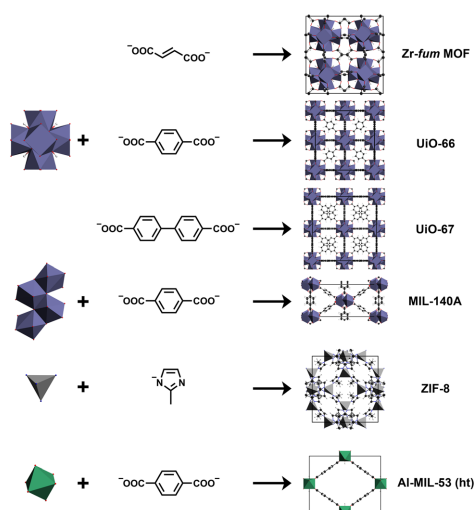


**Fig. 1** Zr-based MOFs, ZIF-8 with SOD topology and Al-MIL-53 (ht). The Zr-*fum* MOF, UiO-66 and UiO-67 share the typical Zr<sub>6</sub>-containing IBU and the expanded cubic closed-packed structure. MIL-140A is based on the *bdc* linker analogously to UiO-66, but has a one-dimensional IBU. ZIF-8 is based on the *mim* linker and show the SOD topology. Al-MIL-53 (ht) is built up by a one-dimensional IBU based on corner-sharing octahedra and the *bdc* linker.

## Methods

### Periodic DFT calculations

Kohn-Sham density functional theory calculations with PBC were used to validate the fragment-based approach and ensure that the studied MOFs are transparent in the visible region by analyzing their band structures in detail.<sup>64</sup> Therefore, a previously published protocol was applied to obtain reliable electronic structures and RI values.<sup>12,13</sup> The calculations were performed using the CASTEP code (version 20.1) employing a plane-wave basis set in combination with pseudopotentials.<sup>65</sup> All MOFs were modelled with primitive cells. The convergence of the plane-wave kinetic energy cutoff and the Brillouin zone sampling were examined with respect to the lattice parameters (see ESI† Section S1). The pseudopotentials were generated on-the-fly using the Koelling-Harmon method to incorporate relativistic effects into the generated pseudopotentials.<sup>66</sup> The PBEsol exchange-correlation (XC) functional was applied to fully relax the structures using “on-the-fly” generated ultra-soft pseudopotentials.<sup>67</sup>

Subsequently three different XC functionals were assessed with regard to the experimental lattice parameters of the MOFs to obtain precise structural models for further characterization (see ESI† Section S1). The experimental reference values were chosen with a focus on single crystal (SC) XRD experiments carried out at low temperatures. To determine suitable XC functionals, full cell relaxations were performed using the parameters described above. The benchmark included the generalized gradient approximation (GGA) functional of Perdew, Burke, and Ernzerhof (PBE) with D2 and TS dispersion correction, respectively, the PBE expansion for solids (PBEsol) as well as its dispersion corrected form (PBEsol-TS), and the rSCAN meta-GGA (mGGA) functional.<sup>67-72</sup>

Using the optimized models, single point HSE06 hybrid DFT calculations were performed to obtain the band structures, the corresponding density of states (DOS) and the dispersion of the refractive index.<sup>73</sup> All calculations were carried out using the determined Brillouin zone sampling and planewave kinetic energy cutoff. The optical properties were calculated applying the tools provided within CASTEP to evaluate the electronic structure, obtain the complex dielectric function and subsequently the dispersion of the index of refraction.<sup>74</sup>

#### Fragmentation scheme for MOFs

A fragmentation scheme was developed to overcome the computationally demanding DFT calculations with PBC to evaluate the RI of a MOF. This scheme yields MOF fragments allowing computationally less expensive molecular DFT calculations to compute polarizabilities and subsequently the calculation the RI of the corresponding MOF.

The developed fragmentation scheme consists of two steps to break down a MOF into fragments. In a first step, the IBU of a MOF is identified and all coordinative IBU-linker bonds are broken heterolytically (see Fig. 2). This results in anionic linker fragments and a cationic IBU residue. In the case of IBUs formed by metal ions *e.g.* ZIF-8, this first step is sufficient to obtain the MOF fragments, because the cationic IBU residue is only a metal cation (see Fig. 2). Therefore, the fragments of such MOFs are anionic linker ions and cationic metal ions. On the contrary, MOFs with a more complex IBU, *e.g.* UiO-66, require a second step to achieve a sufficient fragmentation ensuring a low computational demand. In this second step, all metal-ligand bonds of the IBU are broken heterolytically (see Fig. 2). As a result, metal cations and anionic ligands are obtained. Finally, the fragmentation of MOFs with complex

IBUs results in anionic linker ions, cationic metal ions and anionic ligand ions.

#### Refractive index calculations with MOF fragments

In the MOF fragmentation scheme described above, ionic MOF fragments are employed in isolated molecular DFT calculations. These molecular DFT calculations were performed using the ORCA program (version 4.2.1) with the libXC and libint2 libraries and the def2-QZVP basis set.<sup>75-79</sup> In the first step of all calculations, the structure of the obtained multi-atom fragments were fully relaxed, the details of the calculation parameters are given in the ESI† in Section 3. Afterwards the static polarizability of all fragments was calculated using the coupled-perturbed (CP) SCF method integrated in the ORCA program. The CP SCF method allows the calculation of the polarizability as analytic second derivative of the electronic energy with respect to an applied electric field.<sup>80-82</sup> For further calculations the isotropic polarizability of the fragments was used.

The Lorenz-Lorentz formula relates the polarizability  $\alpha$  and the RI  $n$  of a substance by taking the number density  $N$  into account:<sup>36,37,83</sup>

$$\frac{n^2 - 1}{n^2 + 2} = \frac{4\pi}{3} N \alpha$$

Using the molecular formula of a MOF and number of formula units per unit cell  $Z$ , the total polarizability of the unit cell of a MOF is calculated taking into account the isotropic polarizability of its fragments. An example calculation is given in the ESI† Section 6. The number density of a MOF corresponds to the reciprocal volume of the unit cell of a MOF. Ideally, the unit cell volume  $V$  is obtained from low temperature SC XRD experiments to suit the polarizabilities calculated with

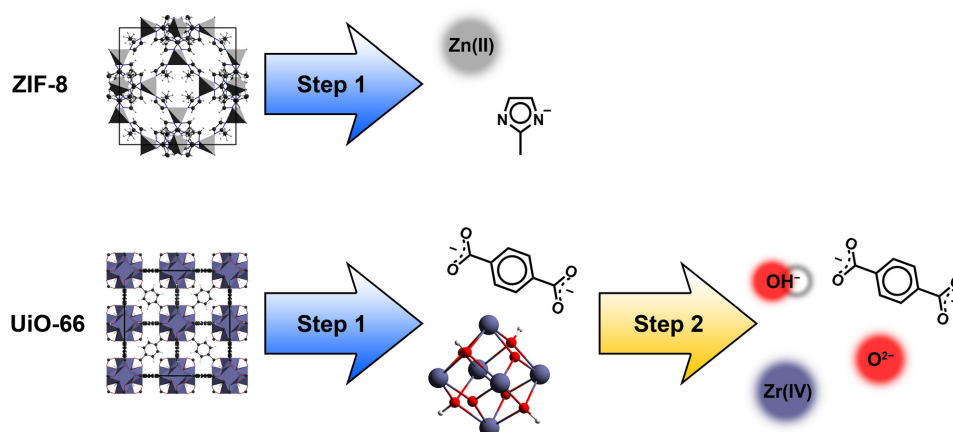


Fig. 2 Fragmentation scheme for MOFs with 2 steps: heterolytic breaking of IBU-linker bonds (step 1) and afterwards heterolytic breaking of residual metal-ligand bonds (step 2).



energy minimized MOF fragments and avoid temperature dependent influences on the RI calculation.

To determine a suitable XC functional for the molecular DFT calculations, benchmark calculations were performed with five hybrid GGA (hGGA) and one hybrid mGGA (hmGGA) XC functional. Following the study of Afzal *et al.* the PBE0 and B3LYP (hGGA) functionals with D3 dispersion correction were tested.<sup>84–86</sup> In addition, both functionals were also assessed without the D3 dispersion correction. According to the study of Ligorio *et al.*, the CAM-B3LYP hGGA and M06-2X hmGGA XC functionals were selected.<sup>87,88</sup> Furthermore, we included the MPW1K and PBE50 hGGA XC functionals.<sup>89,90</sup> Both functionals were part of a benchmark study by Hait *et al.* focusing in the polarizability of small inorganic species.<sup>91</sup> It was shown by Hait *et al.*, that these two functionals were only outperformed by a double hybrid GGA XC functional demanding high computational effort. The Zr-based MOFs UiO-66, MIL-140A and Zr-*fum* MOF were chosen as test set. Using the six mentioned XC functionals, the static RIs of the three MOFs were calculated and compared to reference RI values. The reference values were taken from the RI dispersion curves at 589 nm (D line of sodium vapor) of these MOFs obtained from calculations with our DFT protocol using PBC and the HSE06 hGGA XC functional. Furthermore, materials for optical applications should not show any absorption in the visible region and thus their RI shows only a small frequency dependence making a comparison with static RI values feasible.<sup>22</sup>

Finally, the static RI of 24 MOFs was calculated using the fragment-based approach with the MPW1K XC functional. The RI values were compared to the ones obtained from DFT calculations with PBC and experimental values.

## Results and discussion

This study is concerned with the development of a fragment-based approach for the calculation of the RI of MOFs. This approach should overcome the computationally demanding DFT calculations employing PBC. We first determined a suitable XC functional for the fragment-based approach by examining hGGA and hmGGA functionals with benchmark calculations to validate this novel approach with reference calculations and experimental values.

### XC functional benchmark

To assess a suitable XC functional for the fragment-based calculation of the RI of MOFs, five hGGA and one hmGGA functional were benchmarked. Therefore, the fragment-based approach was applied to the Zr-based MOFs UiO-66, MIL-140A and Zr-*fum* MOF. The MOF UiO-66 is a well-known and widely studied MOF and was chosen as a representative compound.<sup>44,92</sup> The Zr-*fum* MOF features the same topology and IBU as UiO-66 but in contrast it contains the considerably smaller *fum* linker leading to a denser and less porous framework.<sup>46</sup> The MOF MIL-104A consist also the *bdc* linker but possess a one-dimensional IBU forming a denser framework. This allows short-range dispersive interactions between the linkers leading to  $\pi$ -stacking of

these.<sup>45</sup> This collection of MOFs with different linkers showing interacting and isolated arrangements in the frameworks as well as zero- and one-dimensional IBUs, and different patterns of oxo-ligands inside of these IBUs forms a diverse set for the benchmark study. The investigated MOFs are transparent in the visible region as shown by hGGA band structure calculations (see ESI† Section 7). The RI reference values were taken from RI dispersion curves (see ESI† Section 8) at 589 nm obtained from DFT calculations with PBC using our published simulation protocol.<sup>12,13</sup>

The comparison of the static RI values calculated with the fragment-based approach and the reference values (see Fig. 3) shows, that the fragment-based approach is in general a suitable method to calculate the RI of MOFs independently from the choice of the XC functional. All examined XC functionals reproduce the trend of the reference values with acceptable accuracy and allow a qualitative assessment of the RI of the evaluated MOFs. The use of the B3LYP functional with D3 dispersion correction results in the largest mean relative error (MRE) of about 2.5% corresponding to a mean absolute error (MAE) of about 0.035 in the RI (see ESI† Section 4, Fig. S37). Comparing the results obtained with the B3LYP and PBE0 functionals with and without D3 dispersion correction, neglectable differences in the polarizabilities and RIs are observed in the case of the PBE0 functional. In the case of the B3LYP functional, small differences in the polarizability of the *bdc* linker occur due to the altered molecular geometry by the dispersion correction. This is only visible for MIL-140A, because the IBU of MIL-140A is much smaller compared to the Zr<sub>6</sub>-containing IBU of both other MOFs. This results in an increased influence of the polarizability of the linker and thus its molecular geometry on the total polarizability of the MOF. Overall, in contrast to the method for polymers proposed by Afzal *et al.*, no dispersion corrected functionals are needed here. In addition, the benchmark shows that the M06-2X hmGGA functional has the most consistent performance with a MRE smaller than 1% and the smallest standard deviation of all tested XC functionals (see ESI† Section 4 and Fig. S37). PBE50 and MPW1K functionals

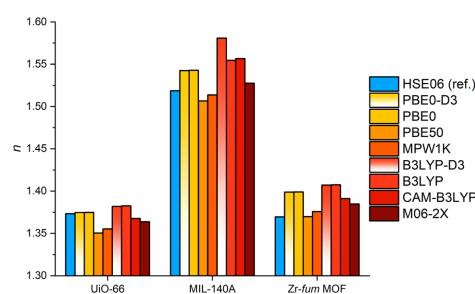


Fig. 3 XC functional benchmark with three Zr-based MOFs. The static RI values obtained with the fragment-based approach (redish) are compared with the reference values at 589 nm obtained using DFT calculations with PBC (blue).

### 3 Results and discussion

Paper

PCCP

show the smallest deviation compared to the HSE06 calculations with PBC, but in the case of PBE50 with a tendency to underestimate the RI. Overall, the MPW1K functional leads to the smallest errors of all tested functionals with a MRE of about 0.7% with the second smallest standard deviation of the benchmark with about 0.5% (see ESI† Section 4 and Fig. S37). Therefore, the MPW1K functional was selected to perform the subsequent calculations.

Although, the fragment-based approach neglects all contributions of the metal–ligand and metal–linker bonds to the polarizability of a MOF as well as the possible interaction of closely packed linker molecules, this benchmark suggests that the chosen fragmentation scheme is valid to obtain more than a coarse qualitative estimate of the RI by using the MPW1K XC functional. Furthermore, a comparison of the CPU times for UiO-66 using the fragment-based approach and the reference calculation with PBC underlines the possible speed up of the RI evaluation by applying the fragment-based approach (see ESI† Section 7 and Tables S5, S6). This comparison reveals a more than 170 times faster calculation of the RI by the fragment-approach with the MPW1K XC functional for UiO-66 with a relative error of about 1.3% and an absolute error of about 0.02 in the RI. This result has encouraged to apply the fragment-based approach using the MPW1K functional to 21 further MOFs.

#### UiO-type MOFs and Zr-*fum* MOF

The fragment-based approach was applied to UiO-66, its monohalogenated derivatives UiO-66-*X* (F, Cl, Br, I), tetrafluoro derivative UiO-66-F<sub>4</sub> and nitro derivative UiO-66-NO<sub>2</sub>.<sup>44,93–96</sup> Additionally, UiO-67 and the Zr-*fum* MOF were evaluated.<sup>44,46</sup> Both share the UiO-66 topology and IBU, but contain a longer (4,4'-biphenyl-dicarboxylate, *bpdc*) and a shorter (*fum*) linker compared to the *bdc* linker of UiO-66, respectively. To ensure the transparency in the visible region band structure calculations were performed at hGGA level (see ESI† Section 8).<sup>12,13</sup> Starting with the Zr-*fum* MOF, the band gaps decrease from 4.41 eV to 3.16 eV for the UiO-66-I MOF (see ESI† Section 8, Fig. S38 and Table S11). The substitution of the acetylenic group of the *fum* linker with the phenylene group in the *bdc* linker results in a reduced band gap of 4.25 eV.<sup>12</sup> The introduction of a second phenylene group to the linker leads to the *bpdc* linker of UiO-67 resulting in a further reduced band gap of 3.51 eV (see ESI† Fig. S40). In the same manner, the functionalization of the *bdc* linker leads to a reduction of the band gap. In the series of UiO-66 derivatives, UiO-66-F MOF shows the largest band gap of 3.96 eV followed by the nitro, tetrafluoro, chloro, bromo and iodo compounds.<sup>13</sup> While the substitution of the acetylenic group in the *fum* linker with phenylene groups increases the polarizability of the resulting linker (see ESI† Table S4), the RI of UiO-66 is only slightly larger compared to the Zr-*fum* MOF and the RI of UiO-67 even decreases (see Fig. 4 and ESI† Fig. S56). This is caused by the different cell volumes and the resulting number densities. The introduction of larger linkers to the expanded cubic closed-packed structures leads to expansion of the framework. This partly compensates the increasing polarizability of the linkers. The fragment-based

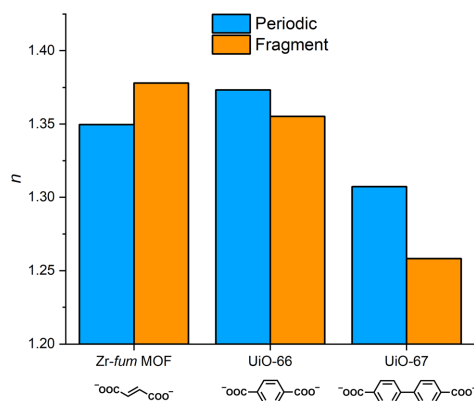


Fig. 4 Comparison of the RI of Zr-*fum* MOF, UiO-66 and UiO-67 (corresponding linkers are shown) calculated with the reference approach with PBC (blue) and the fragment-based approach (orange).

approach reproduces these trends in the RI values reliably with a minimum error of about 0.6% for the Zr-*fum* MOF and a maximum error of about 3.8% for the UiO-67 (see ESI† Table S12 in Section 10).

The introduction of functional groups to the *bdc* linker results in UiO-66 derivatives with tuned optical properties sharing the topology of UiO-66 as well as its cell parameters and thus its number density.<sup>12,13</sup> As a result, the incorporation of linkers into the framework with a lower or higher polarizability than the pristine *bdc* linker leads directly to lower or higher RI values of the resulting MOFs (see Fig. 5 and ESI† Fig. S56). This effect of the linker functionalization is well reproduced by the

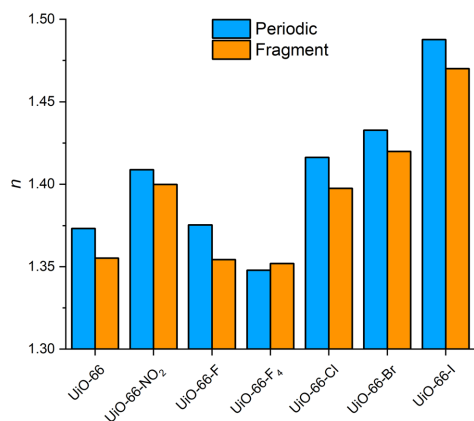


Fig. 5 Comparison of the RI of different UiO-66 derivatives calculated with the reference approach with PBC (blue) and the fragment-based approach (orange).

### 3.3 Fragment-based approach for the efficient calculation of the refractive index of metal-organic frameworks

PCCP

Paper

fragment-based approach with the smallest error of about 0.3% for the UiO-66-F<sub>4</sub> and the largest error of about 1.5% for the UiO-66-F MOF (see ESI† Table S12).

#### MIL-140A and derivatives

MIL-140A MOF is a Zr-based MOF incorporating the *bdc* linker and containing a one-dimensional IBU.<sup>45</sup> This compound is denser compared to UiO-66 allowing short-range dispersive interactions,  $\pi$ -stacking of the linker, and showing a higher number density. The linker interactions result in a large number of delocalized states at the valence band maximum (VBM) (see ESI† Section 8 and Fig. S41), but do not affect the transparency in the visible region ( $E_g = 4.04$  eV). According to the higher number density, MIL-140A has a higher RI compared to UiO-66 (see Fig. 2 and ESI† Fig. S64). Although the fragment-based approach finds on isolated linker fragments without the consideration of intermolecular interactions between the MOF fragments, the RI value of MIL-140A is reproduced in good agreement with an error of about 0.3%.

Analog to UiO-66, the functionalization of the *bdc* linker allows the tuning of the electronic structure and optical properties of MIL-140A (see ESI† Section 8).<sup>97</sup> Additionally, the MIL-140A framework allows the incorporation of functionalized *bdc* linkers without notable changes in the lattice parameters (see ESI† Table S1). Thus, the use of functionalized *bdc* derivatives with increased or decreased polarizabilities results directly in an increase or decrease of the RI of the MIL-140A derivatives compared to the pristine MIL-140A MOF, respectively (see ESI† Section 9 and Fig. S58). This allows the tuning of the RI of MIL-140A frameworks in the remarkable range between about 1.51 (MIL-140A-F) and 1.58 (MIL-140A-Br). The fragment-based approach reproduces this trend (see Fig. 6 and ESI† Table S12) yielding a

minimal error of about 0.4% for the MIL-140A-F and a maximal error of about 2.3% for MIL-140-Br.

#### ZIFs

The ZIF-8 MOF is a prominent representative of the ZIF family formed by zinc ions and *mim* with SOD topology.<sup>52</sup> ZIF-8 shows a band gap of 5.27 eV (see ESI† Fig. S46 and Table S11) and is therefore suitable for optical applications in the visible range as well as in the near infra-red (IR) and ultra-violet (UV) regions.<sup>53,54</sup> The use of differently substituted imidazolate linkers allow the formation of ZIF-8 analog SOD-type ZIFs (see Fig. 7). ZIF-318 and SALEM-2 were modelled as ideal, phase-pure ZIFs without the partial incorporation of the *mim* linker observed in the experiment.<sup>59,60</sup> The band gaps of ZIF-318, ZIF-90, SOD-ZIF-71 and SALEM-2 are larger than 4 eV (see ESI† Section 8). In contrast to the Zr-based MOFs discussed above, these ZIF-8 analogues vary slightly in their lattice parameters causing different number densities (see ESI† Table S1 and S12).<sup>57–60</sup> Nevertheless, the introduction of linkers with higher or lower polarizability results directly in materials with a higher or lower RI, respectively (see Fig. 7 and Fig. S59, ESI†). This allows the tuning of the RI within a given topology in a broad range between 1.26 and 1.39 (at the sodium D-line), while maintaining the transparency in a wide spectrum. The fragment-based approach reproduces this variation of the RI due to the linker functionalization with reasonable precision and a minimal error of about 1% and maximal error of about 3%. Moreover, the fragment-based approach is in very good agreement with the experimental value for ZIF-8 at 589 nm with an error of about 0.7%. Additionally, a comparison of the CPU times for ZIF-8 (see ESI† Section 7 and Table S7, S8) reveals a more than 600 times faster calculation of the RI by the fragment-

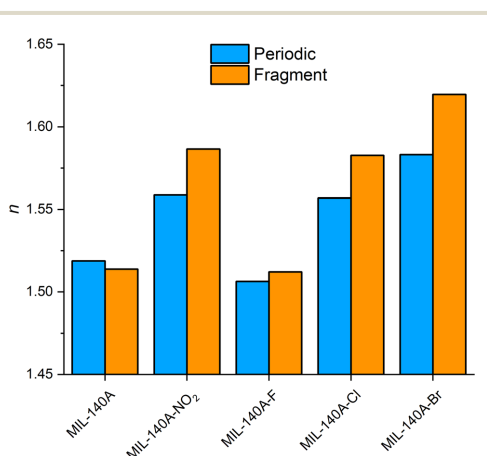


Fig. 6 Comparison of the RI of different MIL-140A derivatives calculated with the reference approach with PBC (blue) and the fragment-based approach (orange).

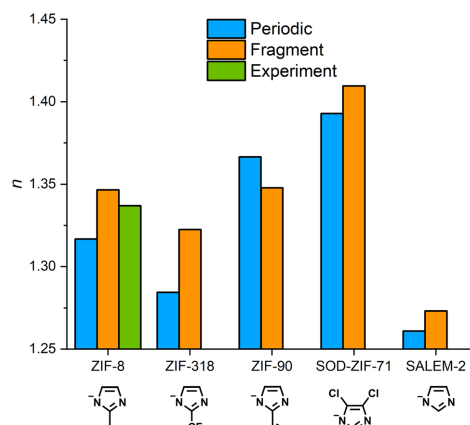


Fig. 7 Comparison of the RI of ZIFs with SOD topology (corresponding linkers are shown): calculated values with the reference approach with PBC (blue) and the fragment-based approach (orange) and experimental value<sup>11</sup> (green) for ZIF-8 (*mim*), ZIF-318 (*cf<sub>3</sub>m*), ZIF-90 (*ica*), SOD-ZIF-71 (*dcim*) and SALEM-2 (*im*).

based approach. This underlines the capability of the fragment-based approach to predict the RI of MOFs efficiently.

In addition to SALEM-2 with SOD topology, further ZIFs based on zinc ions and the *im* linker with different topologies exist, e.g. ZIF-1, ZIF-10 and ZIF-64. The different topologies of those ZIFs involve different lattice parameters (see ESI† Table S1). Due to the identical chemical composition, the electronic structures and band gaps are very similar (see ESI† Section 3) with band gaps of about 5.3 eV. Within this set of MOFs, two pairs of MOFs consisting of SALEM-2 and ZIF-10 as well as ZIF-1 and ZIF-64 (same net, see Table 1) can be distinguished. Each of these pairs have comparable densities leading to analogous RI values (see ESI† Fig. S60 and Table S12). This is well reproduced by the fragment-based approach (see ESI† Fig. S66) with a minimal error of about 0.5% for ZIF-10 and a maximal error of about 3.7% for ZIF-64.

Analog to the zinc-*im*-system, there are also several ZIFs formed by zinc ions and the *dcim* linker with different topologies. Here, ZIF-72 was studied next to SOD-ZIF-71.<sup>61</sup> The band gap of ZIF-72 is only slightly larger (5.18 eV) compared to SOD-ZIF-71 (5.03 eV) (see ESI† Table S11 and Fig. S54), but ZIF-72 has a higher density leading to higher RI values with about 1.48 compared to 1.39 of SOD-ZIF-71 at 589 nm (see ESI† Fig. S61). The fragment-based approach allows a detailed description of this differences in the RI values (see ESI† Fig. S67) with only an error of about 1.2% and 1.0% for SOD-ZIF-71 and ZIF-72, respectively (see ESI† Table S12).

#### Al-MIL-53 (ht)

All afore mentioned MOFs are based on transition metals. To test the fragment-based approach for p-element metals, the ht phase of the well-known Al-MIL-53 MOF was examined. The Al-MIL-53 framework is formed by an one-dimensional Al-based IBU and *bdc* linkers.<sup>62</sup> The MOF is transparent in the visible region with a band gap of 4.48 eV (see ESI† Fig. S55). The RI value at 589 nm of Al-MIL-53 (ht) is slightly larger (1.33) compared to ZIF-8 (1.32) and lower than the value of UiO-66

(1.37) (see ESI† Fig. S62). The dispersion of the RI in the visible region is larger compared to ZIF-8, but very similar to UiO-66. The fragment-based approach allows a reliable calculation of the RI of this p-element-based MOF with an error of about 2.9% (see Fig. 8). Finally, the fragment-based approach allows a more than 70 times faster calculation of the RI (see ESI† Section 7 and Table S9, S10).

#### Comparison of the different MOF sets

In this study, 24 MOFs were examined regarding their RI by applying a fragment-based approach. Of this group, 14 MOFs are Zr-based, 9 MOFs are ZIFs and one MOF is based on aluminum ions. The comparison of the RI of the Zr-based MOFs obtained with the fragment-based approach with reference calculations under PBC shows a mean relative error (MRE) of 1.29% (see Fig. 8) with a minimal and maximal error of 0.30% and 3.75%, respectively. The MRE corresponds to a mean absolute error (MAE) of the RI of about 0.02. The comparison of the calculated RI values of the ZIFs results in a MRE of about 1.9% with a minimal and maximal error of 0.50% and 3.76%, respectively, and a MAE of the RI of about 0.03 (see Fig. 8). The RI of the Al-based MOF was calculated with a relative error of 2.88% and an absolute error of the RI of about 0.04.

The fragment-based approach was developed on the basis of a XC functional benchmark including three different Zr-based MOFs. The results discussed above underline the transferability of the chosen simulation parameters for the fragment-based approach. This approach allows the efficient calculation of the RI of MOFs with a reasonable error compared to demanding DFT calculations with PBC. The MRE of the Zr-based MOFs and ZIFs are below 2% with maximal values below 4%. In the case of the Al-based MOF, the use of the fragment-based approach results in an error below 3%. This points out the capability of the fragment-based approach to predict the RI of MOFs not only qualitatively but also quantitatively. Trends in the RI within a class of MOFs due to linker functionalization as well as effects due to different topologies are also reproduced well. Overall, the fragment-based approach is a promising method to predict the RI of MOFs efficiently with a maximal expected error of approximately 4%.

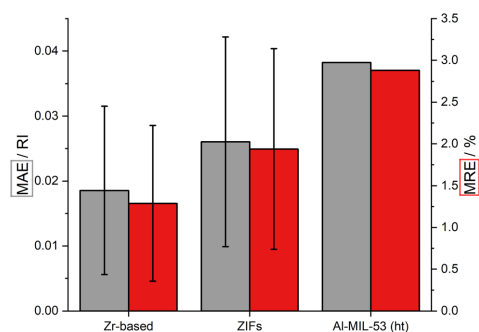


Fig. 8 Comparison of the RI calculated via fragment approach and periodic HSE06 calculation: MAE (gray) and MRE (red) of the examined Zr-based MOFs, ZIFs and Al-MIL-53 (ht).

## Conclusions

An efficient approach for the calculation of the RI of MOFs was developed. The approach is based on a fragmentation scheme for MOFs coupled with molecular DFT calculations. This fragment-based simulation approach allows the calculation of the RI of MOFs circumventing demanding DFT calculations with PBC diminishing the CPU times severely by up to 600 times.

The fragmentation scheme consists of two fundamental steps resulting in anionic linker fragments, cationic metal ions and further anionic ligands in the case of more complex IBUs. Subsequently, molecular DFT calculations are performed to obtain energy minimized fragments and compute their isotropic polarizabilities. Using these polarizabilities, the sum of the polarizabilities of a formula unit of a MOF can be calculated.

### 3.3 Fragment-based approach for the efficient calculation of the refractive index of metal-organic frameworks

PCCP

Paper

This polarizability, the number of formula units per unit cell, and the unit cell volume is then used to calculate the RI of a MOF by applying the Lorenz-Lorentz equation.

To obtain suitable polarizabilities of the MOF fragments, a XC functional benchmark was performed. Therefore, six hGGA and hmGGA XC functionals were assessed using three Zr-based MOFs. As reference, DFT hGGA (HSE06) calculations with PBC were used. The use of the MPW1K functional in combination with the def2-QZVP basis set yielded a MRE below 1% and was chosen for further molecular DFT calculations.

Subsequently, the fragment-based approach was applied to a set of 24 MOFs consisting of 14 Zr-based MOFs, nine ZIFs and one Al-based MOF. The fragment-based approach quantitatively reproduced the trends observed in the RI of the Zr-based MOFs caused by varying lengths of a linker within a given topology as well as different functionalized linkers. Furthermore, the effect of the density of a framework on the RI by using the same linker in two different MOFs (UiO-66 and MIL-140A) was successfully calculated. The MRE for this set of Zr-based MOFs was below 1.5%. The calculations were accelerated by a factor of more than 170 compared to the DFT calculation with PBC. Moreover, the fragment-based approach allowed the calculation of the index of refraction of ZIF-8 and further ZIFs with SOD topology in good agreement with the reference calculations. Here, a reduction of the CPU times of approximately 600 times for ZIF-8 was observed. In addition, the effect of different topologies on the RI of ZIFs within a given metal-linker-system was tested with the fragment-based approach resulting in a precise description of the trends. The MRE for the examined set of ZIFs was below 2% underlining the transferability of the approach. Moreover, the RI value of ZIF-8 obtained with the fragment-based approach was compared to the experimental value revealing an error of less than 1% proving the capability of the fragment-based approach. Finally, the fragment-based approach was used to calculate the RI of the ht phase of Al-MIL-53 to include a non-transition metal-based MOF. Here, the fragment-based approach gave a relative error below 3% while reducing the CPU time more than 70 times. This highlights the reliability and robustness of the developed approach and hints the general applicability of the fragmentation scheme and the chosen combination of XC functional and basis set. All in all, the largest observed relative error of all MOFs was below 4% suggesting an estimated relative error for the prediction of RI values of maximal 4% while massively reducing the required computational effort and thus the calculation time.

Additionally, this study highlights the versatility of MOF as materials for optical applications due to their modular design. Within the chosen set of 24 MOFs, a broad range of RI values between 1.24 (ZIF-10) and 1.58 (MIL-140A-Br) was observed with full transparency in the visible spectral region. In combination with the presented fragment-based approach for the calculation of the RI, this promotes further studies of MOFs as materials for optical applications, e.g. the automated screening of MOF databases and the design of novel MOFs. Aiming for very low and high RI values, this allows the improvement of existing optical systems like coatings of mirrors and lenses as well as

the design of novel optical systems like waveguiding elements, optical filters or in Fabry-Pérot devices.

Finally, we propose from our study that future work should focus on the extension of the presented fragment-based approach allowing the calculation of frequency-dependent polarizabilities. This should allow the efficient calculation of absorption spectra as well as the dispersion of the RI.

#### Conflicts of interest

There are no conflicts to declare.

#### Acknowledgements

This work was supported by the LUH compute cluster, which is funded by the Leibniz University Hannover, Germany, the Lower Saxony Ministry of Science and Culture and the German Research Association (DFG). This work is funded by the DFG under Germany's Excellence Strategy within the Cluster of Excellence PhoenixD (EXC 2122, Project ID 390833453).

#### References

- 1 H. K. Raut, V. A. Ganesh, A. S. Nair and S. Ramakrishna, *Energy Environ. Sci.*, 2011, **4**, 3779.
- 2 C. Rodríguez, S. Günster, D. Ristau and W. Rudolph, *Opt. Express*, 2015, **23**, 31594.
- 3 H.-Y. Pan, X. Chen and X.-L. Xia, *Renewable Sustainable Energy Rev.*, 2022, **161**, 112361.
- 4 E. K. Macdonald and M. P. Shaver, *Polym. Int.*, 2015, **64**, 6.
- 5 D. H. Kim, W. Jang, K. Choi, J. S. Choi, J. Pyun, J. Lim, K. Char and S. G. Im, *Sci. Adv.*, 2020, **6**, eabb5320.
- 6 T. N. Nguyen, F. M. Ebrahim and K. C. Stylianou, *Coord. Chem. Rev.*, 2018, **377**, 259.
- 7 Y. Zheng, F.-Z. Sun, X. Han, J. Xu and X.-H. Bu, *Adv. Optic. Mater.*, 2020, **8**, 2000110.
- 8 K.-T. Hsu, P. Thanasekaran, T.-W. Hsu, C.-H. Su, B.-C. Chang, Y.-H. Liu, C.-H. Hung and K.-L. Lu, *CrystEngComm*, 2021, **23**, 824.
- 9 H. Li, L. Zhang, H. He, Y. Yang, Y. Cui and G. Qian, *Sci. China Mater.*, 2021, **64**, 698.
- 10 W. Yin, C.-A. Tao, F. Wang, J. Huang, T. Qu and J. Wang, *Sci. China Mater.*, 2018, **61**, 391.
- 11 N. C. Keppeler, K. D. J. Hindricks and P. Behrens, *RSC Adv.*, 2022, **12**, 5807.
- 12 M. Treger, A. Hannebauer, A. Schaate, J. L. Budde, P. Behrens and A. M. Schneider, *Phys. Chem. Chem. Phys.*, 2023, **25**, 6333.
- 13 M. Treger, A. Hannebauer, P. Behrens and A. M. Schneider, *Phys. Chem. Chem. Phys.*, 2023, **25**, 15391.
- 14 J. L. Rowsell and O. M. Yaghi, *Microporous Mesoporous Mater.*, 2004, **73**, 3.
- 15 S. R. Batten, N. R. Champness, X.-M. Chen, J. Garcia-Martinez, S. Kitagawa, L. Öhrström, M. O'Keeffe, M. Paik Suh and J. Reedijk, *Pure Appl. Chem.*, 2013, **85**, 710.

### 3 Results and discussion

Paper

PCCP

- 16 M. A. Syzgantseva, C. P. Ireland, F. M. Ebrahim, B. Smit and O. A. Syzgantseva, *J. Am. Chem. Soc.*, 2019, **141**, 6271.
- 17 K. Hendrickx, D. E. P. Vanpoucke, K. Leus, K. Lejaeghere, A. van Yperen-De Deyne, V. van Speybroeck, P. van der Voort and K. Hemelsoet, *Inorg. Chem.*, 2015, **54**, 10701.
- 18 M. D. Allendorf, M. E. Foster, F. Léonard, V. Stavila, P. L. Feng, F. P. Doty, K. Leong, E. Y. Ma, S. R. Johnston and A. A. Talin, *J. Phys. Chem. Lett.*, 2015, **6**, 1182.
- 19 S. M. Moosavi, A. Nandy, K. M. Jablonka, D. Ongari, J. P. Janet, P. G. Boyd, Y. Lee, B. Smit and H. J. Kulik, *Nat. Commun.*, 2020, **11**, 4068.
- 20 Y. J. Colón and R. Q. Snurr, *Chem. Soc. Rev.*, 2014, **43**, 5735.
- 21 B. Ni, W. Sun, J. Kang and Y. Zhang, *J. Phys. Chem. C*, 2020, **124**, 11595.
- 22 M. A. F. Afzal, C. Cheng and J. Hachmann, *J. Chem. Phys.*, 2018, **148**, 241712.
- 23 M. A. F. Afzal and J. Hachmann, *Phys. Chem. Chem. Phys.*, 2019, **21**, 4452.
- 24 R. F. Ligorio, A. Krawczuk and L. H. R. Dos Santos, *J. Phys. Chem. A*, 2020, **124**, 10008.
- 25 M. Ernst, L. H. R. Dos Santos and P. Macchi, *CrystEngComm*, 2016, **18**, 7339.
- 26 M. A. Collins and R. P. A. Bettens, *Chem. Rev.*, 2015, **115**, 5607.
- 27 D. Hua, H. R. Leverentz, E. A. Amin and D. G. Truhlar, *J. Chem. Theory Comput.*, 2011, **7**, 251.
- 28 J. Hellmers, E. D. Hedegård and C. König, *J. Phys. Chem. B*, 2022, **126**, 5400.
- 29 M. R. Ryder, Z. Zeng, K. Titov, Y. Sun, E. M. Mahdi, I. Flyagina, T. D. Bennett, B. Civaleri, C. S. Kelley and M. D. Frogley, *et al.*, *J. Phys. Chem. Lett.*, 2018, **9**, 2678.
- 30 R. Warmbier, A. Quandt and G. Seifert, *J. Phys. Chem. C*, 2014, **118**, 11799.
- 31 D. S. Chemla, J. L. Oudar and J. Jerphagnon, *Phys. Rev. B: Solid State*, 1975, **12**, 4534.
- 32 K. Wu and C. Chen, *J. Cryst. Growth*, 1996, **166**, 533.
- 33 K. Wu, J. G. Snijders and C. Lin, *J. Phys. Chem. B*, 2002, **106**, 8954.
- 34 R. D. Shannon and R. X. Fischer, *Phys. Rev. B: Condens. Matter Mater. Phys.*, 2006, **73**, 235111.
- 35 R. D. Shannon and R. X. Fischer, *Am. Mineral.*, 2016, **101**, 2288.
- 36 L. Lorenz, *Ann. Phys. Chem.*, 1880, **247**, 70.
- 37 H. A. Lorentz, *Ann. Phys. Chem.*, 1880, **245**, 641.
- 38 S. T. Ang, A. Pal and S. Manzhos, *J. Chem. Phys.*, 2018, **149**, 44114.
- 39 A. Pal, S. Arabnejad, K. Yamashita and S. Manzhos, *J. Chem. Phys.*, 2018, **148**, 204301.
- 40 S. S. Park, S. Lee, J. Y. Bae and F. Hagelberg, *Chem. Phys. Lett.*, 2011, **511**, 466.
- 41 C. Haichuan, J. Guozhu, Z. Liang and H. Yinshu, *Phys. Chem. Liq.*, 2014, **53**, 435.
- 42 S. Maekawa, K. Moorthi and Y. Shigeta, *J. Comput. Chem.*, 2016, **37**, 2759.
- 43 Y. Bai, Y. Dou, L.-H. Xie, W. Rutledge, J.-R. Li and H.-C. Zhou, *Chem. Soc. Rev.*, 2016, **45**, 2327.
- 44 J. H. Cavka, S. Jakobsen, U. Olsbye, N. Guillou, C. Lamberti, S. Bordiga and K. P. Lillerud, *J. Am. Chem. Soc.*, 2008, **130**, 13850.
- 45 V. Guillerm, F. Ragone, M. Dan-Hardi, T. Devic, M. Vishnuvarthan, B. Campo, A. Vimont, G. Clet, Q. Yang and G. Maurin, *et al.*, *Angew. Chem.*, 2012, **124**, 9401.
- 46 G. Wißmann, A. Schaate, S. Lilienthal, I. Bremer, A. M. Schneider and P. Behrens, *Microporous Mesoporous Mater.*, 2012, **152**, 64.
- 47 J. H. Cavka, S. Jakobsen, U. Olsbye, N. Guillou, C. Lamberti, S. Bordiga and K. P. Lillerud, *J. Am. Chem. Soc.*, 2008, **130**, 13850.
- 48 S. J. Garibay and S. M. Cohen, *Chem. Commun.*, 2010, **46**, 7700.
- 49 M. Kandiah, M. H. Nilsen, S. Usseglio, S. Jakobsen, U. Olsbye, M. Tilset, C. Larabi, E. A. Quadrelli, F. Bonino and K. P. Lillerud, *Chem. Mater.*, 2010, **22**, 6632.
- 50 B. Ni, W. Sun, J. Kang and Y. Zhang, *J. Phys. Chem. C*, 2020, **124**, 11595.
- 51 Y. Huang, C.-A. Tao, R. Chen, L. Sheng and J. Wang, *Nanomaterial*, 2018, **8**, 676.
- 52 K. S. Park, Z. Ni, A. P. Côté, J. Y. Choi, R. Huang, F. J. Uribe-Romo, H. K. Chae, M. O'Keeffe and O. M. Yaghi, *Proc. Natl. Acad. Sci. U. S. A.*, 2006, **103**, 10186.
- 53 L. Zheng, N. Keppler, H. Zhang, P. Behrens and B. Roth, *Adv. Mater. Technol.*, 2022, **7**, 2200395.
- 54 K.-J. Kim, P. Lu, J. T. Culp and P. R. Ohodnicki, *ACS Sens.*, 2018, **3**, 386.
- 55 W. Vandezande, K. P. F. Janssen, F. Delpont, R. Ameloot, D. E. de Vos, J. Lammertyn and M. B. J. Roefsaers, *Anal. Chem.*, 2017, **89**, 4480.
- 56 G. Lu and J. T. Hupp, *J. Am. Chem. Soc.*, 2010, **132**, 7832.
- 57 M. E. Schweinefuss, S. Springer, I. A. Baburin, T. Hikov, K. Huber, S. Leoni and M. Wiebecke, *Dalton Trans.*, 2014, **43**, 3528.
- 58 W. Morris, C. J. Doonan, H. Furukawa, R. Banerjee and O. M. Yaghi, *J. Am. Chem. Soc.*, 2008, **130**, 12626.
- 59 S. S. Mondal, M. Hovestadt, S. Dey, C. Paula, S. Glomb, A. Kelling, U. Schilde, C. Janiak, M. Hartmann and H.-J. Holdt, *CrystEngComm*, 2017, **19**, 5882.
- 60 O. Karagiari, M. B. Lalonde, W. Bury, A. A. Sarjeant, O. K. Farha and J. T. Hupp, *J. Am. Chem. Soc.*, 2012, **134**, 18790.
- 61 R. Banerjee, A. Phan, B. Wang, C. Knobler, H. Furukawa, M. O'Keeffe and O. M. Yaghi, *Science*, 2008, **319**, 939.
- 62 T. Loiseau, C. Serre, C. Huguenard, G. Fink, F. Taulelle, M. Henry, T. Bataille and G. Férey, *Chemistry*, 2004, **10**, 1373.
- 63 M. O'Keeffe, M. A. Peskov, S. J. Ramsden and O. M. Yaghi, *Acc. Chem. Res.*, 2008, **41**, 1782.
- 64 W. Kohn and L. J. Sham, *Phys. Rev.*, 1965, **140**, A1133–A1138.
- 65 S. J. Clark, M. D. Segall, C. J. Pickard, P. J. Hasnip, M. I. J. Probert, K. Refson and M. C. Payne, *Z. Kristallogr.*, 2005, **220**, 567.
- 66 D. D. Koelling and B. N. Harmon, *J. Phys. C: Solid State Phys.*, 1977, **10**, 3107.

### 3.3 Fragment-based approach for the efficient calculation of the refractive index of metal-organic frameworks

PCCP

Paper

- 67 J. P. Perdew, A. Ruzsinszky, G. I. Csonka, O. A. Vydrov, G. E. Scuseria, L. A. Constantin, X. Zhou and K. Burke, *Phys. Rev. Lett.*, 2008, **100**, 136406.
- 68 J. P. Perdew, K. Burke and M. Ernzerhof, *Phys. Rev. Lett.*, 1996, **77**, 3865.
- 69 S. Grimme, *J. Comput. Chem.*, 2006, **27**, 1787.
- 70 A. Tkatchenko and M. Scheffler, *Phys. Rev. Lett.*, 2009, **102**, 73005.
- 71 W. A. Al-Saidi, V. K. Voora and K. D. Jordan, *J. Chem. Theory Comput.*, 2012, **8**, 1503.
- 72 A. P. Bartók and J. R. Yates, *J. Chem. Phys.*, 2019, **150**, 161101.
- 73 J. Paier, M. Marsman, K. Hummer, G. Kresse, I. C. Gerber and J. G. Ángyán, *J. Chem. Phys.*, 2006, **125**, 249901.
- 74 A. J. Morris, R. J. Nicholls, C. J. Pickard and J. R. Yates, *Comput. Phys. Commun.*, 2014, **185**, 1477.
- 75 F. Neese, *WIREs Comput. Mol. Sci.*, 2012, **2**, 73.
- 76 F. Neese, *WIREs Comput. Mol. Sci.*, 2018, **8**, e1327.
- 77 S. Lehtola, C. Steigemann, M. J. Oliveira and M. A. Marques, *SoftwareX*, 2018, **7**, 1.
- 78 E. F. Valeev, Libint: A library for the evaluation of molecular integrals of many-body operators over Gaussian functions, can be found under <https://libint.valeev.net/>, 2019.
- 79 F. Weigend and R. Ahlrichs, *Phys. Chem. Chem. Phys.*, 2005, **7**, 3297.
- 80 J. A. Pople, R. Krishnan, H. B. Schlegel and J. S. Binkley, *Int. J. Quantum Chem.*, 1979, **16**, 225.
- 81 N. C. Handy, D. J. Tozer, G. J. Laming, C. W. Murray and R. D. Amos, *Isr. J. Chem.*, 1993, **33**, 331.
- 82 B. G. Johnson and M. J. Fisch, *J. Chem. Phys.*, 1994, **100**, 7429.
- 83 H. Kragh, *Substantia*, 2018, **2**, 7.
- 84 C. Adamo and V. Barone, *J. Chem. Phys.*, 1999, **110**, 6158.
- 85 A. D. Becke, *J. Chem. Phys.*, 1993, **98**, 5648.
- 86 S. Grimme, J. Antony, S. Ehrlich and H. Krieg, *J. Chem. Phys.*, 2010, **132**, 154104.
- 87 T. Yanai, D. P. Tew and N. C. Handy, *Chem. Phys. Lett.*, 2004, **393**, 51.
- 88 Y. Zhao and D. G. Truhlar, *Theor. Chem. Acc.*, 2008, **120**, 215.
- 89 B. J. Lynch, P. L. Fast, M. Harris and D. G. Truhlar, *J. Phys. Chem. A*, 2000, **104**, 4811.
- 90 Y. A. Bernard, Y. Shao and A. I. Krylov, *J. Chem. Phys.*, 2012, **136**, 204103.
- 91 D. Hait and M. Head-Gordon, *Phys. Chem. Chem. Phys.*, 2018, **20**, 19800.
- 92 S. Øien, D. Wragg, H. Reinsch, S. Svelle, S. Bordiga, C. Lamberti and K. P. Lillerud, *Cryst. Growth Des.*, 2014, **14**, 5370.
- 93 F. Vermoortele, M. Vandichel, B. van de Voorde, R. Ameloot, M. Waroquier, V. van Speybroeck and D. E. de Vos, *Angew. Chem., Int. Ed.*, 2012, **51**, 4887.
- 94 S. Biswas, J. Zhang, Z. Li, Y.-Y. Liu, M. Grzywa, L. Sun, D. Volkmer and P. van der Voort, *Dalton Trans.*, 2013, **42**, 4730.
- 95 Z. Hu, Y. Peng, Z. Kang, Y. Qian and D. Zhao, *Inorg. Chem.*, 2015, **54**, 4862.
- 96 M. Kandiah, M. H. Nilsen, S. Usseglio, S. Jakobsen, U. Olsbye, M. Tilset, C. Larabi, E. A. Quadrelli, F. Bonino and K. P. Lillerud, *Chem. Mater.*, 2010, **22**, 6632.
- 97 W. Liang, R. Babarao and D. M. D'Alessandro, *Inorg. Chem.*, 2013, **52**, 12878.





## 4 Conclusion and outlook

The present work deals with the examination of metal-organic frameworks for optical applications. Therefore, two DFT-based simulation approaches were developed allowing the quantitative calculation of the RI of MOFs. The developed methods were used to analyze how the modular components of MOFs influence their optical properties. Furthermore, it was emphasized that the modular design of MOFs can be utilized to adjust the RI over a broad range resulting in highly adaptable materials for optical applications.

In the first part of this thesis, a simulation approach based on periodic boundary conditions was developed aiming at the precise calculation of the RI. For the development and validation of this method, the prominent Zr-based MOF UiO-66 was chosen. The calculation of the RI of UiO-66 was already addressed previously by two studies. Both studies used small plane wave basis sets and GGA XC functionals in combination with a scissors operator to correct the calculated band gap. As a result the obtained RI values were only qualitative and allowed the discussion of trends instead of a detailed comparison of different materials. To overcome this limitations, a simulation approach was developed that ensures a proper convergence of the plane wave basis set and an adequate choice of XC functionals to enable the reliable calculation of the RI of MOFs.

The first step of the developed simulation approach is concerned with the evaluation of the plane wave basis set size. Therefore, the convergence of the kinetic energy cutoff value is monitored with respect to the lattice parameters. Subsequently, different XC functionals and dispersion corrections are assessed with respect to the experimental lattice parameters of a MOF obtained from single crystal X-ray diffraction experiments. As a result, fully relaxed periodic models are obtained giving precise representations of the MOF structures. In addition, influences of the basis set size and variations of the cell volume are eliminated in the following step. Finally, the HSE06 XC functional is used to assure the adequate calculation of the electronic structure and the corresponding optical properties. This procedure was validated by comparing the calculated band gap values with experimental values obtained from UV-Vis DRS measurements.

Following these steps, this approach was applied to UiO-66 and its well-known nitro- and amino-functionalized derivatives UiO-66-NO<sub>2</sub> and UiO-66-NH<sub>2</sub>, respectively. In accordance with powder X-ray diffraction measurements, the three prepared periodic models were isostruc-

#### 4 Conclusion and outlook

tural and had closely matching lattice parameters underlining the robustness of the UiO-66 framework topology towards the introduction of functionalized linkers. Additionally, the lattice parameters of the models had a relative error below 0.2% compared to the experimental ones emphasizing the importance of the convergence of the basis set and the careful selection of XC functionals. Moreover, the calculated and experimental band gap values were in good agreement substantiating a trustworthy calculation of the electronic structure and the corresponding optical properties. The influence of the electron withdrawing (“pull”) nitro and electron donating (“push”) amino groups on the RI was studied by analyzing the band structures and DOS in detail. It was shown, that the altering of the electronic structure due to the functional groups of the linker resulted in higher RI values compared to the pristine UiO-66 ( $n_D = 1.37$ ). As a consequence, a novel UiO-66 derivative was presented built up by a “push-pull” linker. The compound constructed by this amino–nitro benzene dicarboxylate was denoted as UiO-66-(NH<sub>2</sub>,NO<sub>2</sub>). Again, the calculated structural properties as well as the band gap were on par with the experiment. Finally, the incorporation of the “push-pull” linker resulted in a remarkable increase of the RI ( $n_D = 1.50$ ). Consequently, this concept was further extended and three more UiO-66 derivatives with “push-pull” motifs were examined. The designed *bdc* linkers were equipped with a stronger “push” or “pull” moiety, or both. This resulted in MOFs with largely increased RI values up to 1.78 at 589 nm. Overall, a series of isostructural materials with closely matching lattice parameters was presented with RI values varying over a broad range. This highlighted MOFs as highly adaptable materials for optical applications due to their modular design.

The first study summarized above, was concerned with the establishment of the developed simulation approach and its validation as well as the presentation of MOFs as adaptable modular materials for optical applications. The investigated materials showed large RI values due to their “push-pull” motifs but this resulted also in materials with a limited transparency in the visible spectral region reducing the field of possible optical applications. To circumvent these shortcomings, the use of halogenated *bdc* linkers was studied. Starting with the established monohalogenated UiO-66-*X* ( $X = \text{F, Cl, Br, I}$ ) derivatives, the calculated lattice parameters and band gaps were compared with experimental values. Here, the capabilities of the developed simulation approach were illustrated by a relative error less than 0.1% for the calculated lattice parameters and a good agreement of the band gaps. Subsequently, the band structures and DOS were studied to analyze the effect of the different halogen atoms on the RI of these materials. While the introduction of fluorine atoms had no considerable effect on the RI in the

Vis region, the use of heavier halogens led to increasing RI values up to 1.49 at 589 nm (UiO-66-I). In addition to the established monohalogenated UiO-66 derivatives, a novel dihalogenated derivative built up by the diiodo benzene dicarboxylate linker was presented. This diiodo analogue (UiO-66-I<sub>2</sub>) is isostructural to UiO-66 but a slightly expanded cell was observed due to the steric demand of the iodine atoms. UiO-66-I<sub>2</sub> showed a further increased RI with 1.59 at 589 nm. Finally, the halogenation of linkers was presented as an effective method to exploit the modular design of MOFs and obtain a series of materials with a broad adaptability of the RI. Furthermore, the use of halogenated linkers allows to preserve the transparency in the Vis region widening the field of possible optical applications. Besides the preservation of the transparency, the use of halogenated linkers allows the tuning of the optical properties while maintaining the porosity of the frameworks. This enables the incorporation of guest molecules to further tune the optical properties or perform sensing.

In the second part of this thesis, a fragment-based simulation approach was developed aiming at the efficient calculation of the RI of MOFs. While the simulation approach presented in the first part of this thesis allows detailed studies of the crystal structure and the corresponding electronic and optical properties, it is computationally demanding. Consequently, it is not suitable for the direct and fast examination of the RI of MOFs for example to preselect compounds for a certain experiment or optical application. Therefore, the central concept of the fragment-based approach is to perform DFT calculations with (multi-atom) fragments instead of periodic models. To obtain these fragments, a fragmentation scheme was developed to decompose MOFs. In a first step, the metal-linker bonds are broken heterolytically resulting in anionic linker fragments and cationic IBU residues. In the case of simple IBUs built up only by individual metal ions, this first fragmentation step is sufficient. More complex IBUs require a second fragmentation step, in which all metal-ligand bonds of the IBU residues are broken heterolytically resulting in anionic ligands and metal cations. Afterwards, molecular DFT calculations are performed to obtain the static polarizabilities of the fragments. These polarizabilities are used to calculate the total polarizability of the MOF. By applying the Lorenz-Lorentz equation, the static RI of a MOF is calculated using its polarizability and the volume of its unit cell.

To determine a suitable XC functional, the fragment-based approach was applied to three Zr-based MOFs using five hGGA and one hmGGA functional as well as two hGGA functionals with dispersion correction. This series of eight calculations using the def2-QZVP basis set was benchmarked by taking the RI values obtained with the periodic simulation approach

#### 4 Conclusion and outlook

as reference. The comparison of the RI values revealed, that the fragment-based approach is suitable to reproduce the trend of the reference values in general and independently from the choice of the XC functional. Finally, the hGGA MPW1K functional was selected allowing a quantitative assessment of the RI.

Subsequently, the fragment-based approach was applied to 21 further MOFs. The calculated RI values were compared to the reference values obtained with the periodic simulation approach to validate the fragment-based approach. Starting with MOFs of the isorecticular UiO-66 series and functionalized UiO-66 derivatives, Zr-based MOFs were examined. A comparison of the CPU time for the pristine UiO-66 revealed a speed up factor larger than 170 indicating the capabilities of the fragment-based approach for an efficient calculation of the RI. Furthermore, MIL-140A and some of its functionalized derivatives were studied. Despite the neglect of the  $\pi$ -stacking of linkers occurring in MIL-140A MOFs, the RI values calculated with the fragment-based approach were in good agreement with the reference calculations. Additionally, the fragment-based approach was assessed by applying it to nine different ZIFs. Five of these ZIFs showed the **sod** topology including ZIF-8. The CPU times of the ZIF-8 calculations were compared and resulted in speed up by more than 600 times. Moreover, the RI value of ZIF-8 calculated with the fragment-based approach was found to be in good agreement with the experimental value with a relative error less than 1%. In total, the mean relative errors of the set of Zr-based MOFs and the set of ZIFs were both below 2% with maximal error values below 4%. To test fragment-based approach for p-element metals in addition to the transition metal-based MOFs, the Al-MIL-53 MOF was examined resulting in a relative error below 3%.

These results emphasize the capability of the fragment-based approach to perform quantitative calculations of the RI with small computational effort regardless of the type of MOF. The calculated RI values of the different series of MOFs also point out how the modular design of MOFs can be used to tune the RI over a broad range while maintaining the topology and with negligible differences of the cell parameters. This is especially interesting for optical elements based on systems of thin layers. Another important aspect is the successful speed up of the RI calculations. The developed fragment-based approach allows the screening of MOF databases to identify MOFs with exceptionally high or low RI values as well as MOFs with a certain RI value.

All in all, two simulation approaches were developed to examine the RI of MOFs. The first approach relies on periodic models and allows detailed studies of MOFs, while the second approach is focused on the efficient calculation of the RI of MOFs. The combination of these

approaches can be used to identify MOFs with a specific RI. Therefore, screenings of MOF databases or derivatives of a given MOF can be performed followed by a detailed study of the selected compounds. Additionally, both approaches can be used to design novel MOFs for optical applications requiring a certain RI. In this context, the fragment-based approach allows a first evaluation of novel materials with small computational effort accelerating the research process. Subsequently, the periodic simulation approach can be applied to characterize novel materials in detail. In addition, this periodic simulation approach can be used to validate experimental RI values and enable a deeper understanding of the studied materials.

Finally, both simulation approaches could be extended with a focus on host-guest systems. The incorporation of guest molecules into the porosity of MOFs can be utilized to tune the RI. The resulting changes of the RI were already studied experimentally using ZIF-8 for example. To study these systems with computational methods, additional simulation approaches have to be developed allowing the precise description of the intermolecular interactions of MOFs and guest molecules. Subsequently, models of these host-guest systems can be prepared. These models could be evaluated using the periodic simulation approach. In a following step, the fragmentation scheme of the fragment-based approach could be revised to be suitable for MOFs loaded with guest molecules. This revised fragmentation scheme should comprise the preparation of fragments representing the intermolecular interactions of the host-guest systems. Therefore, the fragments should include the interaction of the MOFs and the guest molecules as well as the interaction of the guest molecules with themselves.

Furthermore, the fragment-based approach could be extended to allow calculations beyond the static RI. Therefore, frequency-dependent calculations of the polarizability have to be performed. Additionally, a revision of the XC functional benchmark might be required to obtain the RI dispersion in accordance with experimental values and values calculated using the periodic simulation approach.



## 5 Curriculum vitae

Marvin Treger

Date of birth 15.07.1994  
Place of birth Hildesheim

since 04/2019 **Doctorate**  
Gottfried Wilhelm Leibniz Universität Hannover  
Institute of Inorganic Chemistry  
In the group of Prof. Dr. Peter Behrens

10/2016 – 09/2018 **Master of Science** Material- und Nanochemie  
Gottfried Wilhelm Leibniz Universität Hannover

Master thesis in the group of Prof. Dr. Peter Behrens  
Institute of Inorganic Chemistry  
Title: *Simulation of the structure and adsorption properties  
of metal-organic frameworks*

10/2013 – 09/2016 **Bachelor of Science** Chemie  
Gottfried Wilhelm Leibniz Universität Hannover

Bachelor thesis in the group of Prof. Dr. Peter Behrens  
Institute of Inorganic Chemistry  
Title: *Interlayer expansion of MWW-type zeolites  
with selected silanes*

06/2013 **Abitur**  
Otto-Hahn-Gymnasium Springe





## 6 Publications

### Articles presented in this work

*Tuning the optical properties of the metal-organic framework UiO-66 via ligand functionalization*

M. Treger, A. Hannebauer, A. Schaate, J. L. Budde, P. Behrens, A. M. Schneider, *Phys. Chem. Chem. Phys.* **2023**, 25, 6333–6341.

*Development of high refractive index UiO-66 framework derivatives via ligand halogenation*

M. Treger, A. Hannebauer, P. Behrens, A. M. Schneider, *Phys. Chem. Chem. Phys.* **2023**, 25, 15391–15399.

*Fragment-based approach for the efficient calculation of the refractive index of metal-organic frameworks*

M. Treger, C. König, P. Behrens, A. M. Schneider, *Phys. Chem. Chem. Phys.* **2023**, 25, 19013–19023.

### Further articles

*Metal-Organic Framework Co-MOF-74-Based Host-Guest Composites for Resistive Gas Sensing*

I. Strauss, A. Mundstock, M. Treger, K. Lange, S. Hwang, C. Chmelik, P. Rusch, N. C. Bigall, T. Pichler, H. Shiozawa, J. Caro, *ACS Appl. Mater. Interfaces* **2019**, 11, 14175–14181.

### Oral presentations

*Optical properties of nanoporous materials from first principles*

M. Treger, Nils C. Keppler, P. Behrens, A. M. Schneider  
Exzellenzcluster PhoenixD – Kolloquium, Hannover, **2021**

*Quantum-mechanical calculation of the optical properties of metal-organic frameworks*

M. Treger, P. Behrens, A. M. Schneider  
33. Deutsche Zeolith-Tagung, Frankfurt am Main, **2022**

## 6 Publications

### Poster presentations

#### *Modelling of graphene-like metal-organic frameworks*

M. Treger, A. M. Schneider, P. Behrens

31. Deutsche Zeolith Tagung, Dresden, **2019**

#### *Tetrathiafulvalene Doped Cobalt containing Metal-Organic Framework for Gas Detection Applications*

I. Strauss, A. Mundstock, H. Shiozawa, M. Treger, K. Lange, S. Hwang, C. Chmelik, P. Rusch, N. Bigall, T. Pichler, J. Caro

31. Deutsche Zeolith Tagung, Dresden, **2019**

#### *Modeling of graphene-like metal-organic frameworks*

M. Treger, P. Behrens, A. M. Schneider

MOFSIM2019, Ghent (Belgium), **2019**

#### *Modelling of metal-organic frameworks for optical applications*

M. Treger, P. Behrens, A. M. Schneider

39. CCP5 Annual General Meeting (AGM), London (United Kingdom), **2019**

#### *Modelling of metal-organic frameworks for optical applications*

M. Treger, P. Behrens, A. M. Schneider

NanoDay of the Laboratory of Nano and Quantum Engineering, Hannover, **2019**

#### *Examination of metal-organic frameworks for optical applications*

M. Treger, P. Behrens, A. M. Schneider

3rd European Conference on Metal Organic Frameworks and Porous Polymers, EuroMOF2019, Paris (France), **2019**

#### *Examination of metal-organic frameworks for optical applications*

M. Treger, P. Behrens, A. M. Schneider

Exzellenzcluster PhoenixD – Area-S Day, Hannover, **2020**

#### *Examination of metal-organic frameworks for optical applications*

M. Treger, N. C. Keppler, P. Behrens, A. M. Schneider

GDCh Wissenschaftsforum, Online, **2021**

*Investigations of the cyclopalladation of metal-organic frameworks containing azobenzene linkers*

N. Marquardt, M. Treger, A. Schaate

4th European Conference on Metal Organic Frameworks and Porous Polymers,

EuroMOF2021, Online, **2021**

*Examination of metal-organic frameworks for optical applications*

M. Treger, N. C. Keppler, P. Behrens, A. M. Schneider

4th European Conference on Metal Organic Frameworks and Porous Polymers,

EuroMOF2021, Online, **2021**

*First principles calculation of the optical properties of metal-organic frameworks*

M. Treger, A. Hannebauer, P. Behrens, A. M. Schneider

20. International Zeolite Conference (IZC-2022), Valencia (Spain), **2022**

*Optical properties of metal-organic frameworks from first principles*

M. Treger, A. Hannebauer, P. Behrens, A. M. Schneider

8th International Conference on Metal-Organic Frameworks and Open Framework Compounds,

MOF2022, Dresden, **2022**

*First principles calculation of the optical properties of metal-organic frameworks*

M. Treger, A. Hannebauer, P. Behrens, A. M. Schneider

NanoDay of the Laboratory of Nano and Quantum Engineering, Hannover, **2022**

*First principles calculation of the optical properties of metal-organic frameworks*

M. Treger, P. Behrens, A. M. Schneider

34. Deutsche Zeolith Tagung, Vienna (Austria), **2023**

